# REPORT DOCUMENTATION PAGE

| 1. REPORT DATE (DD-MM-YYYY) | 2. REPORT TYPE | 3. DATES COVERED (From - To) |
|---|---|---|
| 08-12-2016 | Final Technical Report | 07/09/2014 to 07/08/2016 |

**4. TITLE AND SUBTITLE**
Autonomous Control Modes and Optimized Path Guidance for Shipboard Landing in High Sea States

**5a. CONTRACT NUMBER**
N00014-14-C-0004

**5b. GRANT NUMBER**

**5c. PROGRAM ELEMENT NUMBER**

**6. AUTHOR(S)**
Horn, Joseph
He, Chengjian
Roark, Sean
Yang, Junfeng
Tritschler, John
Gonzalez, Geraldo

**5d. PROJECT NUMBER**

**5e. TASK NUMBER**

**5f. WORK UNIT NUMBER**

**7. PERFORMING ORGANIZATION NAME(S) AND ADDRESS(ES)**
The Pennsylvania State University
Office of Sponsored Programs
110 Technology Center
University Park, PA 16802-7000

**8. PERFORMING ORGANIZATION REPORT NUMBER**

**9. SPONSORING/MONITORING AGENCY NAME(S) AND ADDRESS(ES)**
Office of Naval Research
875 North Randolph Street
Arlington, VA 22203-1995

**10. SPONSOR/MONITOR'S ACRONYM(S)**

**11. SPONSOR/MONITOR'S REPORT NUMBER(S)**

**12. DISTRIBUTION/AVAILABILITY STATEMENT**
DISTRIBUTION STATEMENT A: Distribution Approved for public release; distribution is unlimited.

**13. SUPPLEMENTARY NOTES**
None

**14. ABSTRACT**

The research address the technical challenge of landing a helicopter on a ship in high sea states. An autonomous control law architecture for ship landing is proposed and developed. The controllers are tested using high fidelity simulation models of three classes of generic helicopters: light, medium, and heavy. The control design deals with inner and outer loop control, path generation and optimization, and landing using deck tracking and forecasting of deck motion. The control laws were successfully demonstrated in simulation for all three classes of helicopters. Dynamic inversion design proved to be an effective and portable control law, which can be tuned to achieve desired balance in stability margins and disturbance rejection. A deck forecasting algorithm using Minor Components Analysis was developed and integrated with landing path generation algorithms. Path optimization studies developed feasible methods for tailoring approach paths to minimize a weighted objective functions based on airwake disturbances, tracking performance, and power consumption. Future work will conduct comprehensive testing and evaluation of the integrated control laws with optimized approach paths.

**15. SUBJECT TERMS**
HELICOPTER, ROTORCRAFT, FLIGHT CONTROL, DYNAMIC INTERFACE, SHIP LANDING

| 16. SECURITY CLASSIFICATION OF: | | | 17. LIMITATION OF ABSTRACT | 18. NUMBER OF PAGES | 19a. NAME OF RESPONSIBLE PERSON |
|---|---|---|---|---|---|
| a. REPORT | b. ABSTRACT | c. THIS PAGE | | | Joseph F. Horn |
| U | U | U | UU | | 19b. TELEPHONE NUMBER (Include area code) (814) 865-6434 |

# Autonomous Control Modes and Optimized Path Guidance for Shipboard Landing in High Sea States

## Base Effort Final Report (CDRL A002)
## August 12, 2016

| PI: Joseph F. Horn | Co-PI: Chengjian He | Co-PI: Sean Roark |
|---|---|---|
| 814-865-6434 | (408) 523-5100 | (301)995-7093 |
| joehorn@psu.edu | he@flightlab.com | sean.roark@navy.mil |
| Junfeng Yang | Dooyong Lee | Geraldo Gonzalez |
| Grad. Research Assistant | | |
| | Advanced Rotorcraft | NAVAIR 4.3.2.4 |
| Penn State University | Technologies | |
| | | John Tritschler |
| | | U.S. Navy Test Pilot School |

**Performing Organization:**
**The Pennsylvania State University**
**Department of Aerospace Engineering**
**231C Hammond Building**
**University Park, PA 16802**
**Attn: Joseph F. Horn**
**Phone: 814-865-6434, Fax: 814-865-7092**
**Email: joehorn@psu.edu**

# Table of Contents

# Notation

| Variable | Description |
|---|---|
| $A, B, C$ | system matrix, control matrix and output matrix of a linear system |
| $e$ | error |
| $g$ | gravitational acceleration |
| $J$ | objective function |
| $K_D, K_p, K_I, K_{II}$ | differential, proportional, integral and double integral gains of PID compensator |
| $L_p, M_q, N_r$ etc. | stability derivatives e.g. $L_p = \dfrac{\partial L}{\partial p}$ |
| $M_{\delta lon}, Z_{\delta col}$ etc. | control derivatives e.g. $M_{\delta lon} = \dfrac{\partial M}{\partial \delta_{lon}}$ |
| $p, q, r$ | body roll, pitch and yaw angular rates |
| $R_{pd}$ | range of peak deceleration |
| $R, r$ | range of helicopter to landing spot |
| $s$ | Laplace operator |
| $u, v, w$ | body forward, right and downward velocities |
| $V_0$ | approach asymptotic speed |
| $V_N, V_E, V_Z$ | velocity vector in North-East-Up Frame (NEU) |
| $V_x^{HHF}, V_y^{HHF}, V_z^{HHF}$ | velocity vector in Helicopter Heading Frame (HHF) |
| $V_x^{SHF}, V_y^{SHF}, V_z^{SHF}$ | velocity vector in Ship Heading Frame (SHF) |
| $x, y, u$ | state vector, output vector and input vector of a linear system |
| $X_N, Y_E, H$ | position vector in NEU |

| | |
|---|---|
| $X^{HHF}, Y^{HHF}, H^{HHF}$ | position vector in HHF |
| $X^{SHF}, Y^{SHF}, H^{SHF}$ | position vector in SHF |
| $y_r$ | reference signal for tracking |
| $\delta_{lat}, \delta_{lon}, \delta_{col}, \delta_{ped}$ | Lateral, longitudinal, collective and directional control input |
| $\phi, \theta, \psi$ | bank, pitch, yaw attitude angles |
| $\gamma_{app}, \psi_{app}$ | approach glide slope angle and azimuth angle |
| $v$ | pseudo-command |
| $\tau, p$ | time constant and pole of 1st order systems |
| $\psi_s$ | ship heading angle |
| $\zeta, \omega_n$ | damping ratio, natural frequency of 2nd order systems |

## Subscripts

| | |
|---|---|
| $cmd$ | command |
| $col$ | collective |
| $deck$ | flight deck |
| $hov$ | hover |
| $lat$ | lateral cyclic |
| $lon$ | longitudinal cyclic |
| $ped$ | pedals |
| $ship$ | ship |

# 1. Overview of Project

This project is performed under the Office of Naval Research program on Basic and Applied Research in Sea-Based Aviation (ONR BAA12-SN-0028). This project addresses the Sea Based Aviation (SBA) initiative in Advanced Handling Qualities for Rotorcraft.

Landing a rotorcraft on a moving ship deck under the influence of the unsteady ship airwake is extremely challenging. In high sea states, gusty conditions, and a degraded visual environment, the pilot workload required during the landing task begins to approach the limits of a human pilot's capability. It is a similarly demanding task for autonomous control systems used for shipboard launch and recovery of a VTOL UAV. There is a clear need for additional levels of stability and control augmentation and novel control design methods for fully autonomous landing systems. One enabler would be the use of ship state information in the helicopter flight control laws (state information could be gathered by sensors on the helicopter or through telemetry of state information to the helicopter from the ship). Under the SBA program we are tasked with developing new control design methods assuming ship state information is available to the controller. Advanced flight control systems could then expand the operational conditions in which safe landings for both manned and unmanned rotorcrafts can be performed. Some of the specific challenges in design of autonomous landing systems for ship-based rotorcraft include the following:

1. In very high sea states, in order to match the motion of the flight deck, the helicopter needs to perform relatively aggressive maneuvers to avoid premature deck contact and to match deck velocity upon touchdown. Even with deck state information available, the control system needs to provide sufficient lead compensation to effectively match deck motions.

2. In some cases, deck motion might be so severe that the helicopter control system would approach control or power margin limits when holding a relative positon to the landing spot. In such cases an autonomous control system needs to use intelligent control strategies to perform feasible trajectories that match deck state on landing. This requires some kind of predictive compensation (similar to what a human pilot does).

3. Human pilots will commonly hold a stable hover in the inertial frame, identify a quiescent period in ship motion, and land when the deck motion is small. It is desirable to avoid this technique if possible as it extends the time of the landing task, and in very high sea states quiescent periods may occur very rarely.

4. The unsteady airwake of the ship acts as a significant external disturbance to the aircraft. The control systems need suitable disturbance rejection (which results in high gain), while maintaining robust stability (which is aggravated by high gain). In addition, airwake disturbances can aggravate issues related to control and power margins.

5. Airwake disturbances can be very sensitive to the helicopter position relative to the ship deck, and thus are sensitive to the approach path used. For this reason, landing operations are restricted to a single approach path that has been thoroughly tested for a variety of wind-over-deck (WOD) conditions. The current operational paths may not be an optimal, and operations artificially restricted by the acceptable WOD conditions for the established approach path.

Increasing flexibility of approach procedures to use optimal paths and even curved approach for maneuvering ships adds additional complexity but could expand operational envelopes.

This project seeks to develop advanced control law frameworks and design methodologies to provide autonomous landing (or, alternatively, a high level of control augmentation for pilot-in-the-loop landings). The design framework will focus on some of the most critical components of autonomous landing control laws with the objective of improving safety and expanding the operational capability of manned and unmanned rotorcraft. The key components include high performance station-keeping and gust rejection over a landing deck in high winds/sea states, optimized approach path planning that accounts airwake effects and a maneuvering ship, and deck motion feedback algorithms to allow for improved tracking of the desired landing position and timing of final descent.

Figure 1.1 shows a high level diagram describing the key control law technologies developed under this project. The core control law is based on Dynamic Inversion (DI), as documented in the text of Stevens and Lewis 2003. This control law architecture has seen wide use in aircraft flight control design, although is less common in rotorcraft applications. In recent years there have been several application of both non-linear and linear DI control towards a variety of rotorcraft applications (see many examples by Horn et al in the references). The architecture provides good separation of the command following and disturbance rejection functions of the controller and thus is well suited for control application studies such as this one. However, this research is intended to be "control law agnostic" in that many of the design methodologies can be readily applied to other control law architectures such as Explicit Model Following (EMF), which is commonly used in rotorcraft control design. Some of the key focal areas of this research are highlighted in the blue boxes of the diagram in Figure 1.1. These include: 1) Intelligent blending of ship-relative and inertial navigation during approach and station-keeping (section 2.4); 2) Use of deck motion prediction (sections 2.5 and 2.8) for landing and touchdown in high sea state; 3) Path optimization techniques (sections 2.6 and 2.12) for minimizing tracking error and airwake disturbances, and maximizing power / control margins; 4) Constrained optimization of the descent path to account for control and power limitations (sections 2.8 and 2.9); 5) Novel gain optimization methods to achieve optimal disturbance rejection (sections 2.10 and 2.11).
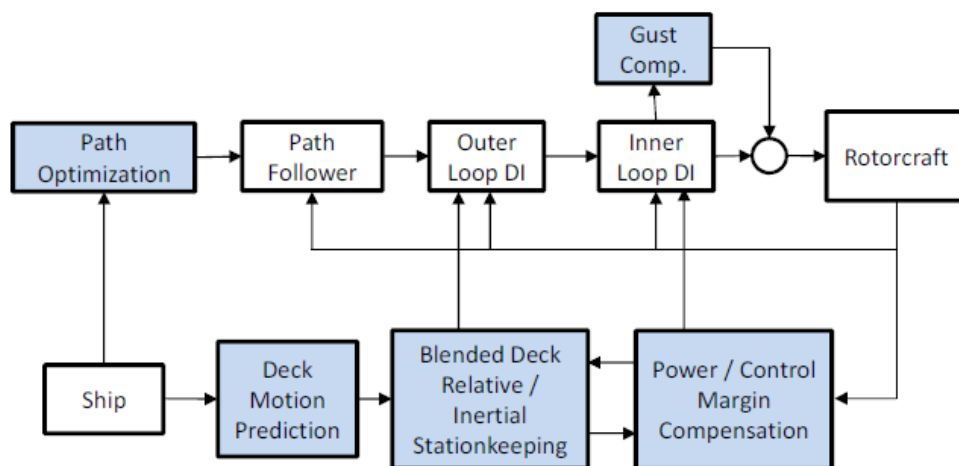


Figure 1.1 High Level Diagram of Control Law Architecture

## 2    Tasks Performed

### 2.1    Task 1 Aircraft plant and ship disturbance models

High fidelity flight dynamic models of the rotorcraft and accurate models of the shipboard environment are critical aspects of this project.  The project has used the FLIGHTLAB modeling and simulation software, which includes accurate models of the coupled non-linear fuselage and rotor blade dynamics, unsteady rotor aerodynamics and inflow models, non-linear landing gear models, engine/rotor RPM dynamics, and the capability to simulate ship airwake and ship motion effects.  Three different classes of rotorcraft have been developed:  1) a small UAV rotorcraft (FireScout class), 2) a utility helicopter (H-60 class), and 3) a large transport rotorcraft (H-53 class).  Table 2.1.1 summarizes the three different models used for the project.  Note that the light and medium class operate from a small deck ship, while the heavy class is assumed to operate from a large deck, thus two different ship environments are used.  During the course of the study, there were a number of modifications to the simulation environment.  The table below represents a snapshot of the final models used at the end of the base effort.

| | Generic Light Class | Generic Medium Class | Generic Heavy Class |
|---|---|---|---|
| Rotorcraft Properties | G.W. = 4,000 lbs<br>Main Rotor:<br>17.5 ft Radius, 3 Blades | G.W. = 17,000 lbs<br>Main Rotor:<br>27 ft Radius, 4 Blades | G.W. = 50,000 lbs<br>Main Rotor:<br>39 ft Radius, 7 Blades |
| Similar Operational Rotorcraft | MQ-8C<br> | SH-60<br> | CH-53E<br> |
| Ship Environment | Generic Model Similar to DDG-51<br>Motion Based on SCONE Small Deck Motion Model<br>Airwake Based on CFD Solutions of SFS2  (Oruc et al, 2015)<br> | | Generic Model Similar to LHA-1. Motion based on Sinusoidal Model of LHA (based on ship motion characteristics published in S. Williams and K. Long, 1997). Airwake based on CFD Solutions from PSU (Nezer-Usol et al 2005)<br> |

Table 2.1.1 Summary of Final Plant Models Used in the Study

The H-60 class model was developed and distributed by ART to both NAVAIR and Penn State research teams. The model consists of an articulated 4-bladed blade element main rotor using unsteady airloads and a high order Peters-He finite state dynamic wake model. It simulates fully articulated rotor dynamics with geometrically exact multi-body dynamics modeling that includes flap and lead-lag degrees of freedom. Each blade is modeled using 10 aerodynamic segments and aerodynamic forces/moments are computed for each segment with respect to the segment local angle of attack, Mach number, and dynamic pressure. The unsteady airloads model allows for the effects of blade yawed-flow, pitch rate, and stall delay due to the blade rotation. The airframe model consists of a fuselage, empennage, sensors, and landing gear. The fuselage is modeled using nonlinear 6-DOF dynamics and the fuselage airloads are computed using empirical table look-up as a function of fuselage angle of attack and angle of sideslip. The empennage consists of both left and right horizontal stabilators as well as a vertical fin. The sensor model outputs aircraft body attitude and rate information for use by the flight control SAS and FPS. The landing gear system model consists of left and right main as well as a tail landing gear. Both main and tail landing gear are modeled using a full nonlinear spring/damper formulation. The landing gear model also considers ground friction and tire deformation effects to support shipboard landing simulation. The FLIGHTLAB flight dynamics models for the light weight (FireScout class) and heavy weight (H-53 class) aircraft have been developed similarly. The light weight class model consists of a 4-bladed blade element main rotor and the heavy weight class model consists of a 7-bladed blade element main rotor model. Both models use unsteady airloads and 6-state Peters-He's finite state dynamic wake model. They simulate fully articulated rotor dynamics with geometrically exact multi-body dynamics modeling that includes flap and lead-lag degrees of freedom.

The ship motion models were initially developed using prescribed sinusoidal functions. The frequencies, phases, and amplitude of the sinusoidal functions were extracted using FLIGHTLAB's 6 DOF ship modeling utility to provide reasonable ship motions based on publicly available information for DDG-class ships (for small deck cases) and LHA-class ships (for large deck cases). Basic ship data was taken from published work [Williams, Long, 1997], but the models do not use detailed hull information and are therefore strictly generic. Later, the Navy released the generic deck motion models for small deck ships through the Systematic Characterization of the Naval Environment (SCONE) program. Subsequently the SCONE motion data were used for all small deck simulations of the light and medium class helicopters. The sinusoidal representation of the generic large deck ship will continued to be used for all heavy class simulations until large deck motion cases become available through the SCONE program.

As mentioned above, the Office of Naval Research and the Naval Surface Warfare Center released a set of standard deck motion time histories under the SCONE program. The motion data was for a Generic Surface Combatant similar to a DDG class ship. The data include "low", "medium", and "high" deck motion cases for both roll-dominated and heave-dominated conditions. In order to align the analyses with these standard deck motion cases, ART integrated the SCONE ship motion data into the FLIGHTLAB simulations of the medium utility helicopter. Two SCONE deck motion cases (for low and medium heave dominated motion) were incorporated into the simulations. FLIGHTLAB drives ship

motion referenced at the CG while the SCONE data only defines the flight deck motion. Since FLIGHTLAB uses the same reference coordinate system for both the ship airwake and the ship motion, the original SCONE data needed to be processed in order to integrate it within the FLIGHTLAB reference frame. Efforts were also needed to integrate and test the SCONE data with the ship deck motion forecasting scheme in order to create a full simulation model for control design and testing support.

Note that the SCONE "low" and "medium" heave-dominated motion cases exhibit relatively large dynamic motion. Table 2.1.2 summarizes the motion for the medium case used in our studies. The +/- 13 ft and 12 ft/sec maximum heave displacement and velocity are of specific interest. This case presents a significant challenge to the automatic landing problem.

| | Displacement | | Rate (deg/sec or ft/sec) | |
|---|---|---|---|---|
| *DOF* | *RMS* | *Max/Min* | *RMS* | *Max/Min* |
| Roll | 0.94° | 3.5°/-4.1° | 0.66 | 3.3 /-2.8 |
| Pitch | 0.91° | 3.7°/-3.4° | 0.89 | 3.9 / -3.3 |
| Yaw | 0.21° | 1.2°/-0.7° | 0.15 | 0.49 / -0.58 |
| Sway | 2.1 ft | 4.3 /-13 ft | 0.88 | 3.3 / -3.7 |
| Heave | 2.5 ft | 25 /-3.5 ft | 2.4 | 11.7 / -10.8 |

Table 2.1.2 Ship Motion Properties for SCONE Medium Heave-Dominated Case #2

For airwake models, CFD solutions of the SFS2 generic frigate shape were used for the small deck ship. These were generated at Penn State [Oruc et al, 2015] for 20 knots, 0° WOD. Later in the project a model for 20 knots, 30° WOD was also generated. The large deck airwake was based on CFD solutions of an LHA-class ship previously developed at Penn State [Sezer-Uzol et al, 2005].

## 2.2 Task 2 Overall control architecture

The autonomous flight control law consists of three functional blocks organized in a modular architecture: Path Generation, Outer loop, and Inner Loop. These are linked in an input-output order with clear interface as shown schematically in figure 2.2.1. The modularity allows many of the concepts used in the approach, deck following and landing to be readily extended to other control law architectures (such as EMF).
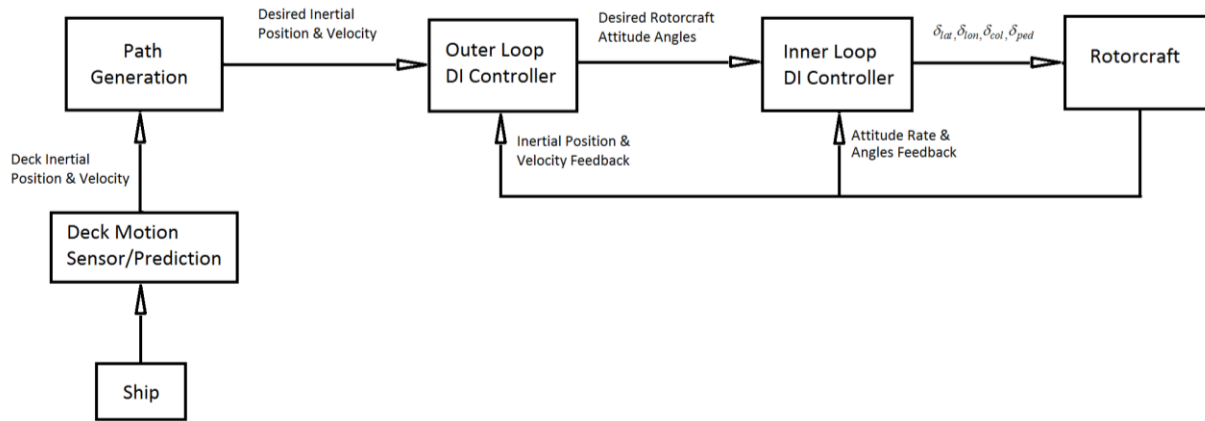
Figure 2.2.1 Overall view of the autonomous flight control law

The Path Generation block generates a reference trajectory in the Inertial Frame. There are different path generation algorithms for different phases of the approach and landing. In the approach phase, the desired path is formulated relatively to the Ship Heading Frame (SHF). The inertial trajectory is the summation of aircraft path in the ship-relative frame with the trajectory of some mean point of deck position. The mean deck position is derived through filtering, where the filter parameters vary with distance to the deck. In the landing phase, the inertial trajectory can be directly defined based on the forecasted and/or measured deck motion.

The Outer Loop DI controller is essentially a path following control law. It accepts reference inertial trajectory, solves for the Euler attitude angles required to track the reference trajectory. The desired Euler attitude angles are then fed into the inner loop DI controller. The Inner loop DI controller is an attitude control system providing basic stability and control augmentation. The inner loop DI control law uses a linear parameter varying model of the helicopter dynamics (reduced order linear models scheduled with airspeed). In theory this is the only part of the model that needs to be modified for different rotorcraft configurations. A set of linear models needs to be generated for each rotorcraft model. In practice we have found that the inner loop DI controller is robust to minor variations in aircraft properties such as gross weight and mass property variations (but rigorous robustness analysis is not part of this study). With inversion of the linear models, the DI controllers (inner loop and outer loop) use simple SISO PID compensators to regulate tracking error. By carefully tuning the control gain of the DI controllers, satisfactory closed-loop response and disturbance rejection can be achieved, while balancing these features with stability margins in order to ensure adequate stability robustness. Details of the control algorithms will be presented in the following sections.

## 2.3   Task 3 Shipboard control design criteria research and implementation

The shipboard control design qualitatively should address satisfactory motion stability, decoupled response in each axis, disturbance rejection, and command tracking performance. In the meantime, necessary stability margins must be maintained. ADS-33 provides a guideline of the quantitative aspect of the performance metrics, while SAE-AS94900 provides guidance on stability margins. In the context

of ship recovery task, additional design criteria closely related with the mission.  Specifically, we are interested in position and velocity tolerances upon landing on the deck.  Table 2.3.1 summarizes some of the desired properties.

|  | Level 1 | Level2 | Level3 |
|---|---|---|---|
| Touchdown Longitudinal Position Error (ft) | ±4 | ±6 | ±8 |
| Touchdown Lateral Position  Error (ft) | ±4 | ±6 | ±8 |
| Touchdown Lateral Velocity Error (ft/sec) | ≤2 | ≤4 | ≤6 |
| Touchdown Vertical  Velocity Error (ft/sec) | ≤2 | ≤4 | ≤6 |

Table 2.3.1 Landing quality metrics

## 2.4   Task 4 Dynamic inversion control laws development and testing

Based on extensive research activity and experience at PSU [see Horn et al in References], the Dynamic Inversion (DI) control law was selected for this research, as it shows great potential in satisfying the above mentioned technical requirements. Therefore, the core stability and control augmentation was constructed using the DI approach.

The DI approach has the advantage that the design process can essentially be automated if a comprehensive set of linear models of the aircraft are readily available.  This is the case for this study, as the FLIGHTLAB simulation tool allows for fast and accurate linearization of the model at any operating point. The linear models can be automatically generated for any configuration, and the models can be reduced and implemented in the inner loop inversion.  The control design then reduces to the selection of a few frequency parameters that govern command models (response to commands) and disturbance rejection.

In the course of this research design scripts were developed for FLIGHTLAB that automated the DI control law design.  These scripts were first developed for the medium class helicopter simulation, then re-used for light and heavy class models.  Following major updates to the various simulation models of each class, the design scripts could be run again to reflect any changed properties in the rotorcraft.  This rapid design process greatly expedited the control design study.

### 2.4.1   Basic Principles of Linear DI Control Laws

A "square" linear system is represented by state space model:

$$\frac{dx}{dt} = Ax + Bu, \; A \in \mathbb{R}^{nxn} \text{ and } B \in \mathbb{R}^{nxm} \tag{2.4.1}$$

$$y = Cx \quad C \in \mathbb{R}^{mxn} \tag{2.4.2}$$

Note that we need to define one output variable per control input.  These are the known as "controlled variables", where each control axis primarily controls one controlled variable.  In this context, the output vector does not represent the only measurement used in the controller, as the design will require full state feedback.

Differentiating Eq. (2.4.2) once with respect to time results in:

$$\dot{y} = C\dot{x} = C\left(Ax + Bu\right) \tag{2.4.3}$$

Eq. (2.4.3) Implies that if we select $u = \left(CB\right)^{-1}\left(\dot{y}_r - CAx\right)$ as the input, then the derivatives of the controlled variables are identical to those of the commanded reference signal:

$$\dot{y} = \dot{y}_r$$

This effectively converts the output response to a system of decoupled integrators. The control law in 2.4.3 is referred to as the feedback linearization loop of DI. Note that it requires full state feedback through the *x* vector in the equation. The control law is normally derived using a reduced order linear model of the system in which all states are measurable (e.g. a 6-DOF rigid body model of the aircraft). The tracking is only accurate in the special case where the initial conditions of the output $y(0)$ match the initial command $y_r(0)$ and when there is neither external disturbance nor modeling error. To correct the tracking for non-zero IC and disturbance, additional compensation denoted by G is added. The summation of the reference signal and the compensation is known as the pseudo-command,

$$u = \left(CB\right)^{-1}\left( \underbrace{\dot{y}_r + G}_{pseudo-command} - CAx \right) \tag{2.4.4}$$

Substituting 2.4.4 into 2.4.3 we can derive the tracking error dynamics

$$e_y \triangleq y_r - y$$
$$\dot{e}_y = \dot{y}_r - \dot{y} = -G \tag{2.4.5}$$

This is the error dynamics of the output governed by the compensator *G*. Care must be taken to construct a proper compensator to shape the error dynamics, so that any error arising from external disturbances or modelling error can decay rapidly. However, it must be kept in mind that the linear model used in DI is approximate, and thus overly aggressive (high gain) compensation must also be avoided. Note that the linearization loop has decoupled the output, thus the compensator can be designed independently for each output variable with SISO techniques. The most widely used compensators are of PID class, which can easily specify the error dynamics as 2$^{nd}$ order or 3$^{rd}$ order linear systems.

Equivalent formulations of the compensator can be derived as either proportional-integral-derivative (PID) or proportional-integrator-double integrator (PII) depending on how the controlled variable is defined. In the case of roll and pitch attitude, we want to control the attitude, but the controlled variable can be defined as the *attitude rate* ( $\dot{y}_r = \dot{\phi}_r$ or $\dot{\theta}_r$ ). The compensator is then readily derived via PII control. The command model is still set up to command and hold attitude, but PII compensation is applied to the attitude rate (which is identical to PID compensation on attitude). Alternatively, we

can define controlled variables as the attitude angle itself. This requires a second differentiation of the plant model in the feedback linearization of (Eq. 2.4.3 is differentiated a 2$^{nd}$ time). In fact, the two formulations are exactly equivalent.

The 3$^{rd}$ order error dynamics can be obtained by applying the following proportional plus integral plus double integrator compensator:

$$G = K_p e_y + K_i \int e_y dt + K_{ii} \iint e_y dt^2$$

Thereby the error dynamics is governed by:

$$\dot{e}_y + K_p e_y + K_i \int e_y dt + K_{ii} \iint e_y dt^2 = 0$$

Differentiate the above equation twice:

$$\dddot{e}_y + K_p \ddot{e}_y + K_i \dot{e}_y + K_{ii} e_y = 0$$

Using a Laplace transform,

$$s^3 e_y + K_p s^2 e_y + K_i s e_y + K_{ii} e_y = \Delta_{IC}(s) \tag{2.4.6}$$

where the right hand side represents perturbation due to initial conditions. The poles of the desired error dynamics can be solved using the following factorized form of the characteristic equation:

$$\left(s^2 + 2\zeta\omega_n s + \omega_n^2\right)(s + p) = 0$$

The natural frequency parameter, damping ratio, and pole can be selected to provide stable error dynamics with reasonable time and frequency domain properties. In practice, these can be set to be in a similar frequency range as the ideal response models (described below).

The corresponding PID gains can be selected as:

$$K_p = 2\zeta\omega_n + p$$

$$K_i = 2\zeta\omega_n p + \omega_n^2 \tag{2.4.7}$$

$$K_{ii} = \omega_n^2 p$$

Similarly, for 2$^{nd}$ error dynamics, the PID compensator

$$G = K_p e_y + K_i \int e_y dt$$

For desired error dynamics of the form:

$$(s + p_1)(s + p_2) = 0$$

The PID gains must be:

$$K_p = p_1 + p_2$$

$$K_i = p_1 p_2$$

Or the error dynamics can be designed with complex poles for given natural frequency and damping ratio:

$$K_p = 2\zeta\omega_n$$

$$K_i = \omega_n^2$$

Higher PID gains obviously lead to faster error decay rate (higher frequency), thus better tracking performance and disturbance rejection. However, necessary stability margins must also be retained. The technique of analyzing the stability margin will be described in section 2.10.

## 2.4.2    DI Inner Loop Design Method

The application of DI theory in designing the inner loop attitude command system is described in this section.

### 2.4.2.1    4th Order DI Control Law

The linear model used for the inner loop is a 4$^{th}$ order linear system, consisting only of angular rates and vertical velocity.

$$\frac{d}{dt}\begin{bmatrix} p \\ q \\ w \\ r \end{bmatrix} = [A]\begin{bmatrix} p \\ q \\ w \\ r \end{bmatrix} + [B]\begin{bmatrix} \delta_{lat} \\ \delta_{lon} \\ \delta_{col} \\ \delta_{ped} \end{bmatrix} \qquad (2.4.8)$$

Controlled variable output vector: $y = \begin{bmatrix} \dot{\phi} \\ \dot{\theta} \\ V_z \\ r \end{bmatrix} \approx \begin{bmatrix} 1 & 0 & 0 & 0 \\ 0 & 1 & 0 & 0 \\ 0 & 0 & -1 & 0 \\ 0 & 0 & 0 & 1 \end{bmatrix}\begin{bmatrix} p \\ q \\ w \\ r \end{bmatrix} = C\begin{bmatrix} p \\ q \\ w \\ r \end{bmatrix}$

This model is a reasonable representation of the short term linear rate dynamics of the helicopter for use in inner loop control. The A and B matrices are based on reduced order linear models extracted directly from the nonlinear FLIGHTLAB model. Models were generated at various airspeeds from hover to 160 knots in 20 knots increments.  Note that the third controller variable is vertical velocity of the aircraft in the inertial frame (positive up), which is assumed to be the negative of the body-axis vertical

velocity. This assumption is not necessarily very good at higher forward speeds. A correction was made later in the project as discussed in section 2.9.

The DI control law is then given by

$$
\begin{bmatrix} \delta_{lat} \\ \delta_{lon} \\ \delta_{col} \\ \delta_{ped} \end{bmatrix} = \left[ B(V) \right]^{-1} \left( \begin{bmatrix} v_p \\ v_q \\ v_w \\ v_r \end{bmatrix} - \left[ A(V) \right] \begin{bmatrix} p \\ q \\ w \\ r \end{bmatrix} \right)
\tag{2.4.9}
$$

Where A(V) and B(V) denote that these matrices are a function of airspeed. They are scheduled at the airspeeds defined above and linearly interpolated at intermediate airspeed. The $v$ parameters are the pseudo-controls which represent the desired accelerations along with PID compensations on the tracking error. The following pseudo-controls were used, where the subscript "m" denotes the desired state value based on our ideal response model:

$$
v_{\phi} = \ddot{\phi}_m + K_{D_{\phi}}(\dot{\phi}_m - \dot{\phi}) + K_{P_{\phi}}(\phi_m - \phi) + K_{I_{\phi}} \int (\phi_m - \phi) dt
$$

$$
v_{\theta} = \ddot{\theta}_m + K_{D_{\theta}}(\dot{\theta}_m - \dot{\theta}) + K_{P_{\theta}}(\theta_m - \theta) + K_{I_{\theta}} \int (\theta_m - \theta) dt
$$

$$
v_r = \dot{r}_m + K_{P_r}(r_m - r) + K_{I_r} \int (r_m - r) dt
$$

$$
v_w = -\left( \dot{V}_{Z_m} + K_{P_{VZ}}(V_{Z_m} - V_Z) + K_{I_{VZ}} \int (V_{Z_m} - V_Z) dt \right)
$$

The block diagram of $v_{\theta}$ and $v_r$ are presented in Fig 2.4.1 and 2.4.2 respectively. Note that inner-loop control law regulates Euler angle rates $\dot{\phi}$ and $\dot{\theta}$, whereas the inversion directly controls body-axis angular rates p and q. The following transformations are applied to convert Euler angle rate pseudo-commands to appropriate body-axis pseudo-commands:

$$
v_p = v_{\phi} - v_{\theta} \tan \phi \tan \theta - v_r \frac{\tan \theta}{\cos \phi}
$$

$$
v_q = v_r \tan \phi + \frac{v_{\theta}}{\cos \phi}
$$

For command following, we also want to define a command filter or ideal response model. This governs the time and frequency response to attitude commands effectively smoothing command inputs and deriving kinematically consistent commands for the controlled variables.

The model responses are governed by simple linear transfer functions. The pitch and roll attitude are second order, for example in roll

$$\begin{bmatrix} \ddot{\phi}_m \\ \dot{\phi}_m \\ \phi_m \end{bmatrix} = \begin{bmatrix} s^2 \\ s \\ 1 \end{bmatrix} \frac{\omega_m^2}{s^2 + 2\zeta_m \omega_m + \omega_m^2} \phi_{cmd}$$

Vertical speed and yaw rate model responses follow 1$^{st}$ order system

$$\begin{bmatrix} \dot{r}_m \\ r_m \end{bmatrix} = \begin{bmatrix} s \\ 1 \end{bmatrix} \frac{1}{\tau_m s + 1} r_{cmd}$$

The *cmd* subscript denotes the commanded state, which comes from the path following control law. Natural frequency parameters of $\omega_n$ =3 rad/sec and 2rad/sec were used in the roll and pitch axes respectively, with damping ratio $\zeta$ =0.9 in roll and 0.7 in pitch. The time constant parameter in the vertical axis was $\tau$ =2 sec, while the yaw axis used $\tau$ =0.4 sec.

The PID gains in equation can be selected to achieve desired error dynamics. They can also be tuned to achieve desired disturbance rejection and/or stability margins. In this study, the gains were initially set so that the error dynamics have similar frequency properties as the command model discussed above. The final assembly of inner loop DI controller is demonstrated in Fig 2.4.3
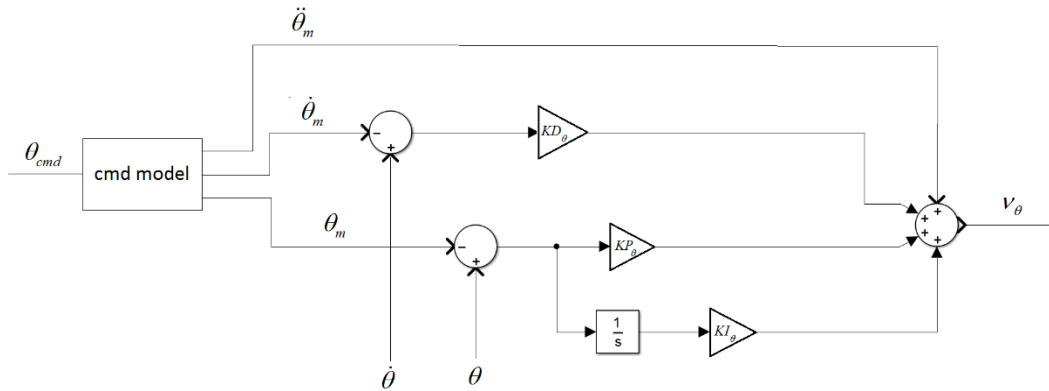


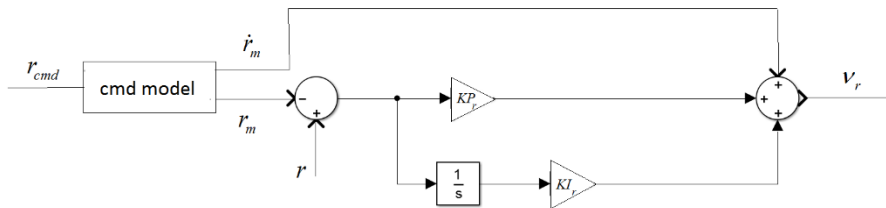Figure 2.4.1 The Diagram of Pseudo-control of Pitch Attitude



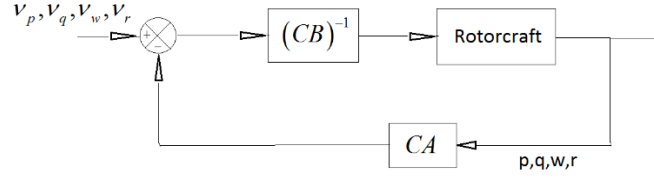Figure 2.4.2 The Diagram of Pseudo-control of Yaw Rate

$$v_p, v_q, v_w, v_r$$

$$(CB)^{-1}$$

Rotorcraft

CA

p,q,w,r

Figure 2.4.3 The Feedback Linearization Loop of The DI Controller

### 2.4.2.2    Simulation Tests of Inner Loop DI Control Laws

Figures 2.4.4 to 2.4.7 demonstrate non-linear simulation results of the inner-loop SCAS system.  These simulations are based on the heavy class helicopter model, trim condition was set with forward speed of 20 kts and an altitude of 300ft, in 2 seconds a doublet command was injected into $\phi_{cmd}$ , $\theta_{cmd}$ , $R_{cmd}$ , $V_{Zcmd}$ in each test case. Non-linear simulation shows that the DI controller successfully addressed the stability and command augmentation objectives, the inter-axial coupling effects have been reduced to HQ requirements.  Note the response tracking is very similar among all three classes of helicopters: light, medium, and heavy.
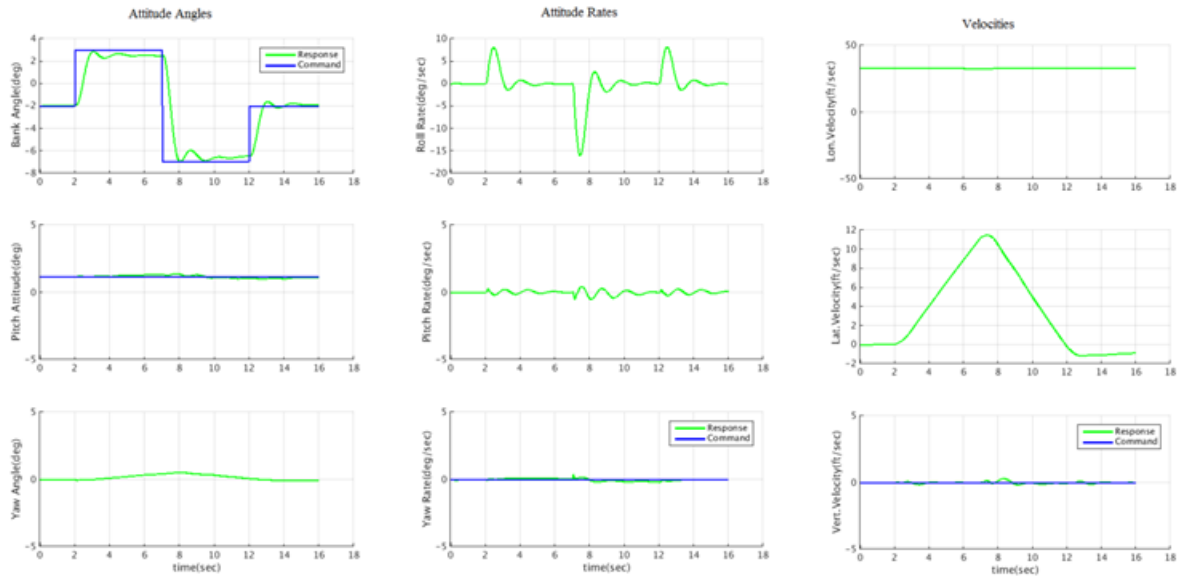


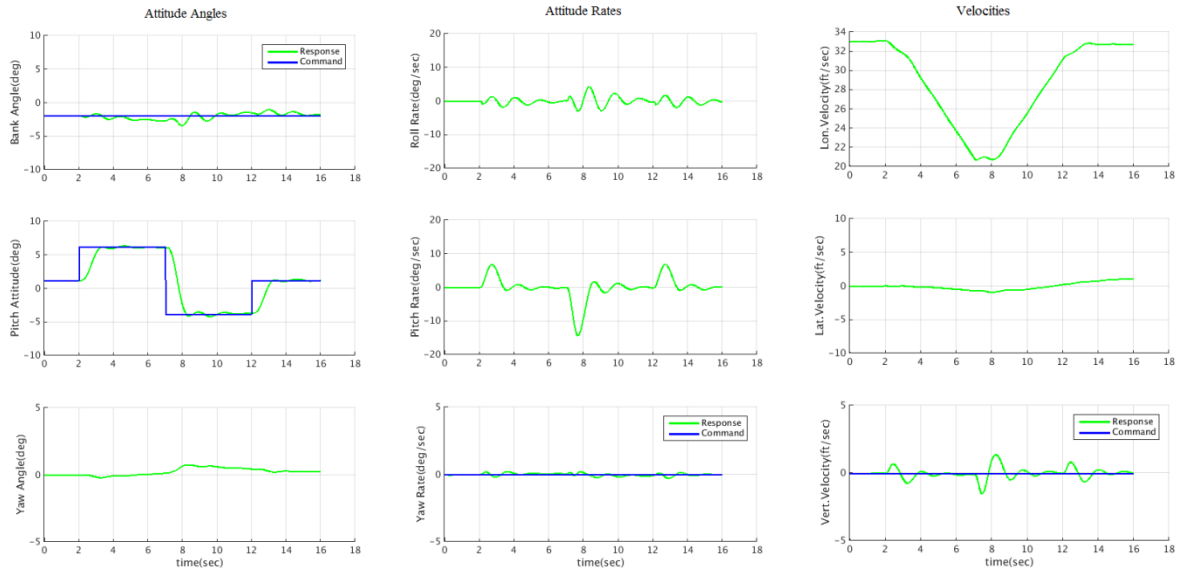Figure 2.4.4. Non-linear Simulation Test of Inner Loop: $\phi_{cmd}$ Doublet

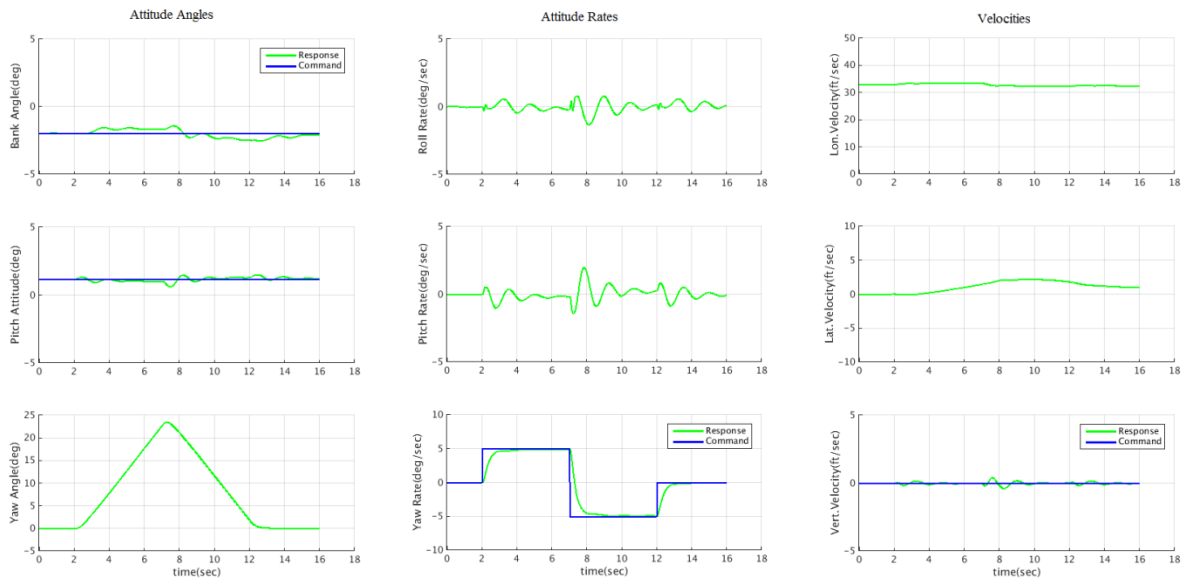Figure 2.4.5. Non-linear Simulation Test of Inner Loop: $\theta_{cmd}$ doublet



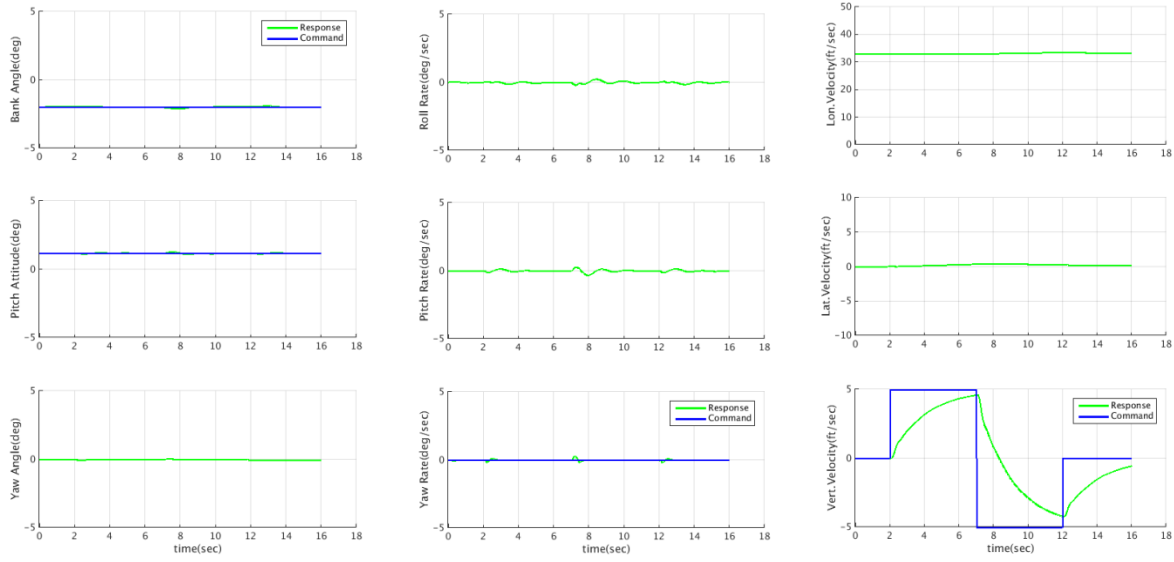Figure 2.4.6. Non-linear Simulation Test of Inner Loop: $r_{cmd}$ Doublet

Figure 2.4.7. Non-linear Simulation Test of Inner Loop: $V_{Zcmd}$ Doublet

## 2.4.3 Path Following Control Law

This work develops fully autonomous control of helicopter starting from a level flight approach, through descent, hover over the flight deck, and final descent to landing. To achieve this goal, a path following control law was developed, it enforces the helicopter to pass through a planned spatial trajectory with desired inertial acceleration, velocities and heading angles.

### 2.4.3.1 Coordinate systems

For the purpose of outer loop guidance and navigation, two sets of coordinate systems are used: flat earth inertial frame (with z axis up – a left handed NEU frame), and the helicopter heading frame (HHF frame is positive forward, right, and up and also a left-handed system). The helicopter heading frame is rotated from the NEU frame by a single rotation about the vertical axis by the helicopter heading as shown by equation below:

$$T_{HHF/NEU} = \begin{bmatrix} \cos\psi & \sin\psi & 0 \\ -\sin\psi & \cos\psi & 0 \\ 0 & 0 & 1 \end{bmatrix}$$

### 2.4.3.2 Outer Loop DI controller

The translational motion of helicopter in horizontal plane can be approximated by the following linear state space mode, this simple model assumes that lateral and longitudinal accelerations in the helicopter heading frame are proportional to perturbations in roll and pitch attitude:

$$\dot{V}_x^{HHF} \approx -g\theta$$

$$V_y^{HHF} \approx g\phi$$

Applying the DI method with commanded attitudes as the plant input yields the control law

$$\theta_{cmd} = -\frac{1}{g}\left( K_{P_{XPOS}} \left( X_{ref}^{HHF} - X^{HHF} \right) + K_{I_{XPOS}} \int \left( X_{ref}^{HHF} - X^{HHF} \right) dt + K_{P_{Vx}} \left( V_{Xref}^{HHF} - V_X^{HHF} \right) + \frac{dV_{Xref}^{HHF}}{dt} \right)$$

$$\phi_{cmd} = \frac{1}{g}\left( K_{P_{YPOS}} \left( Y_{ref}^{HHF} - Y^{HHF} \right) + K_{I_{YPOS}} \int \left( Y_{ref}^{HHF} - Y^{HHF} \right) dt + K_{P_{Vy}} \left( V_{Yref}^{HHF} - V_Y^{HHF} \right) + \frac{dV_{Yref}^{HHF}}{dt} \right)$$

Figure 2.4.8 shows the diagram of longitudinal position controller; the lateral position controller has the same structure.
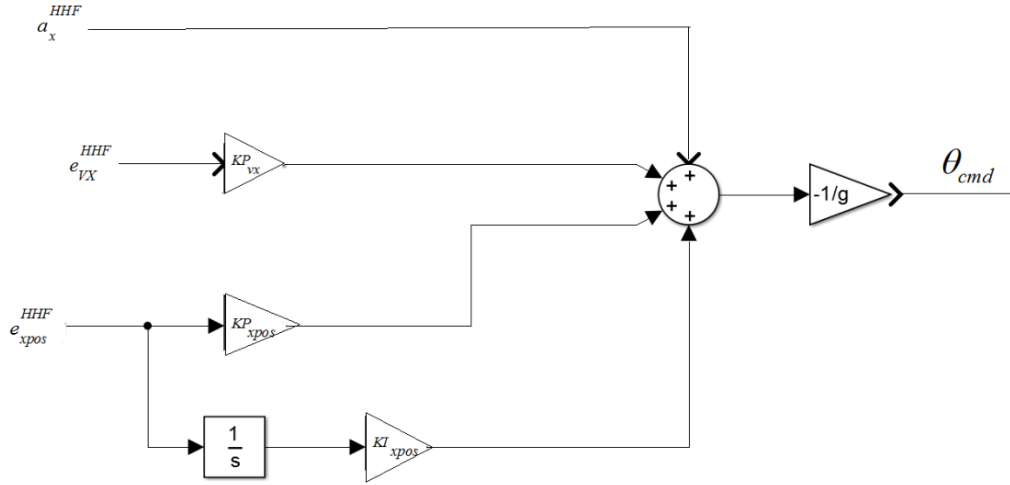


Figure 2.4.8. The Diagram of Longitudinal Position Controller

All measured and commanded position and velocities are defined in inertial frame, as required by the outer-loop control law, their error must be transformed into the HHF. Equation 2.4.9 demonstrates the transformation of position error. The same transformation applies for velocity error and acceleration.

$$\begin{bmatrix} e_X^{HHF} \\ e_Y^{HHF} \end{bmatrix} = \begin{bmatrix} \cos\psi & \sin\psi \\ -\sin\psi & \cos\psi \end{bmatrix} \begin{bmatrix} e_X^{NEU} \\ e_Y^{NEU} \end{bmatrix} \tag{2.4.9}$$

### 2.4.4 Reference Trajectory Generation

This functional block is to provide reference position, velocity and acceleration defined in inertial frame. It may start with a ship relative definition, and then corrected with deck motion (approach navigation uses this method); or an inertial trajectory can be directly generated (predictive landing uses this method).

### 2.4.4.1  Coordinate System

In the path generation, in addition to the NEU inertial frame another frequently used frame is the Ship Heading Frame(SHF). The SHF is obtained by rotating the ship-carried NEU about its vertical axis with the ship heading angle. Transform from NEU to SHF is performed by DCM displayed by equation 2.4.10

$$T_{SHF/NEU} = \begin{bmatrix} \cos\psi_{ship} & \sin\psi_{ship} & 0 \\ -\sin\psi_{ship} & \cos\psi_{ship} & 0 \\ 0 & 0 & 1 \end{bmatrix} \tag{2.4.10}$$

### 2.4.4.2  Approach trajectory

The approach phase starts in steady level flight and terminates with the helicopter hovering about a relative spot to the helicopter. The approach trajectories are initially defined in SHF, two classes of approach paths were developed, straight and curved paths.

#### 2.4.4.2.1  Straight in ship-relative path

This parameterization was initially developed for the path optimization work [Tritschler et al 2015] and has been found to be well suited for straight in approaches. The path is represented by a straight line emanating from the hover spot. Four parameters $\begin{bmatrix} \gamma_{app} & \psi_{app} & V_0 & R_{pd} \end{bmatrix}$ are used to specify to the geometric and kinematic properties of the straight path, $\gamma_{app}, \psi_{app}$ define the glide slope angle and azimuth angle respectively，a positive azimuth value indicates the helicopter is approaching from the starboard of the ship. The relative approach speed is determined by Heffley's formulation Eq. (2.4.11) observed for human pilots [Heffley, 1979].

$$V_{app} = \frac{\left(\dfrac{V_0}{2R_{pd}}\right)R}{1+\dfrac{R}{2R_{pd}}} \tag{2.4.11}$$

Where R is the Range to the landing spot. The tunable constants $V_0$ and $R_{pd}$ represent the asymptotic approach velocity and range at which the peak deceleration occurs.  The reference position and velocities in ship heading frame are governed by Eqs. (2.4.12):

$$X^{SHF} = -R\cos\gamma_{app}\cos\psi_{app}, \quad V_x^{SHF} = V_{app}\cos\gamma_{app}\cos\psi_{app}$$

$$X^{SHF} = R\cos\gamma_{app}\sin\psi_{app}, \quad V_y^{SHF} = V_{app}\cos\gamma_{app}\sin\psi_{app} \tag{2.4.12}$$

$$H^{SHF} = R\sin\gamma_{app}, \quad V_z^{SHF} = -V_{app}\sin\gamma_{app}$$

These coordinates describe the position and velocities of helicopter relative to the final hover point over the flight deck, which are transformed into the inertial NEU reference frame by adding the deck

motion. However, on approach it is not desirable to track the dynamic motion of the flight deck due to sea state, so the deck motions are filtered to yield an estimate of the steady trajectory due to ship course and heading. Details of the filters are described in section 2.4.4.2.

The airspeed in the end of the approach is relatively low and the aircraft must fly with non-zero bank angle to trim in rectilinear flight. At low speeds there is insufficient aerodynamic force to balance lateral forces with sideslip and the helicopter must bank left. Transitions between coordinated flight (zero bank angle) at higher speeds to zero sideslip flight at low speeds can result in unwanted transients. Thus the entire approach is performed in an uncoordinated flight mode. Bank angle is used to regulate lateral velocity, and the heading is set to align with the velocity vector as in Eq. (2.4.13)

$$\psi_{cmd} = \tan^{-1}\left(\frac{V_{Ecmd}}{V_{Ncmd}}\right) \tag{2.4.13}$$

The helicopter starts the approach in straight and level flight, so an entry maneuver is required to enter the decelerating descent. The entry is achieved by ramping in the desired approach glide slope as the aircraft passes through a threshold range. This scheme effectively acheives a constant speed push-over maneuver to smoothly enter the descent. The vertical speed and altitude commands (in the ship frame) are governed by:

$$W_R = \frac{R - R_{des}}{R_{init} - R_{des}}$$

$$\gamma_1 = (1 - W_R)\gamma_{app} \qquad \gamma_2 = W_R \sin^{-1}\left(\frac{h_{init}}{R_{init}}\right)$$

$$V_Z^{SHF}{}_{cmd} = -V_{app} \sin\gamma_1 \qquad h_{cmd} = R\sin(\gamma_1 + \gamma_2)$$

where $R_{init}$ is the range to a point where the pushover is initiated, and $R_{des}$ is the range to the point where the pushover is completed and the helicopter is in steady descent. These range parameters were set to 2000 ft and 1000 ft respectively, which resulted in a reasonable load factor during the push-over. Once the pushover is completed, the helicopter holds constant glide slope relative to the ship while decelerating according the profile

The approach profile is illustrated Fig. 2.4.9. Note that the commanded heading of the helicopter is not the same as the relative approach azimuth, $\psi_{app}$, but results from the vector sum of the relative approach velocity vector and the ship's velocity. Similarly, the actual glide slope of the approach in the inertial frame will be less than the approach glide slope, $\gamma_{app}$. The shallower angles on the inertial approach allow the helicopter to meet the ship at the end of the trajectory.
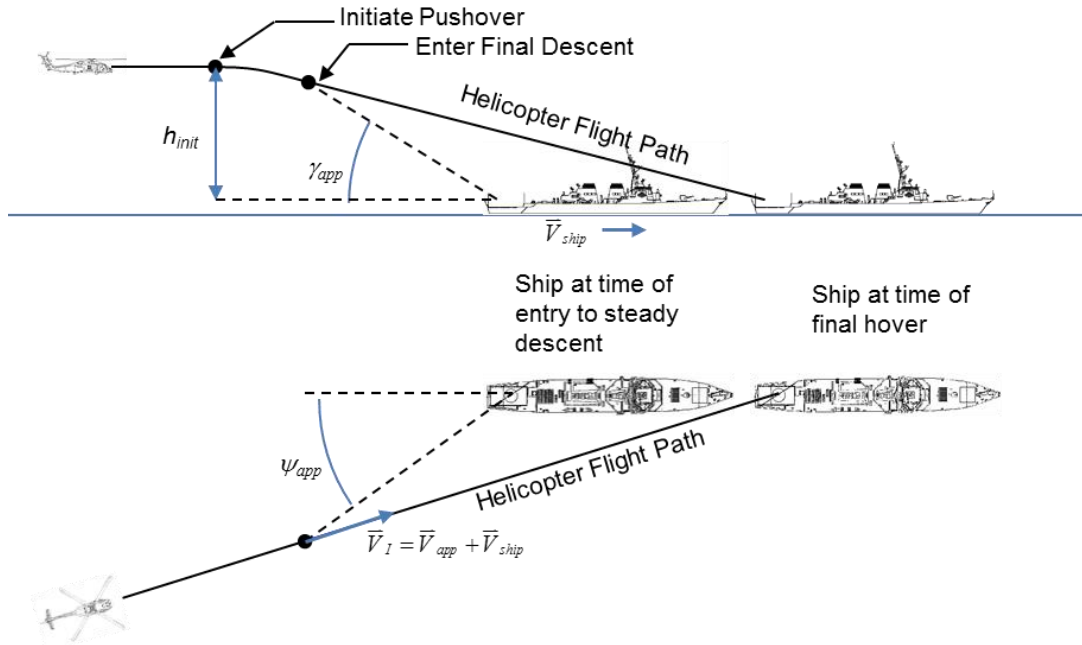
Fig 2.4.9. Ship Relative and Inertial Approach Trajectory

### 2.4.4.2.2  Curved approach path

To accommodate more complex trajectories and to provide additional path optimization criteria, a curved path generation was developed. Among the various curve definition methods, the B-spline was dound to provide excelent properties in the task of flight navigation.

A spline function is a piecewise polynomial function of degree K, where K is the order of spline. K=2, 3 defines parabolic and cubic spline respectively. In science and engineering, cubic splines are most widely used for its simplicity, robustness, and smoothness (up to 2$^{nd}$ derivative continuity). The definition of a cubic polynomial $y = ax^3 + bx^2 + cx + d$ requires four equations to determine four coefficients. Given 4 points, p1, p2, p3, p4, using the condition that the cubic curve passes through those four points we can collect enough equations to solve for polynomial coefficients. However, a polynomial can also be defined as Bezier curve. Bezier curve is given by de'Casteljau algorithm [Farin, 1988].

Given : $b_0$ , $b_1$ ,....., $b_n$ $\in$ $E^3$ , and t$\in$ $R$

Set: $b_i^r(t) = (1-t)b_i^{r-1}(t) + tb_{i+1}^{r-1}(t)$ $\begin{cases} r = 1,.....,n \\ i = 0,......,n-r \end{cases}$

If $b_i^r(t) = b_i$ then $b_0^n(t)$ is the point with parameter value $t$ on the Bezier curve $b^n$ . The polygon formed by $b_0$ , $b_1$ , ..... , $b_n$ is called the Bezier polygon or control polygon of the curve, similarly the polygon vertices $b_i$ are called control points or Bezier points.

The Bezier curve has the following properties

- It is a polynomial curve
- N+1 control points define $N^{th}$ order Bezier curves
- Unlike conventional polynomial interpolation, the Bezier curve interpolates only the end points, but not the intermediate points.
- According to the Casteljau algorithm, high order Bezier curves are obtained by interpolation of low order ones in the same recursive pattern.
- The parameter $t$ is defined on the range, $t \in [0,1]$

The cubic case n=3 is shown for t=1/4 in figure 2.4.10.
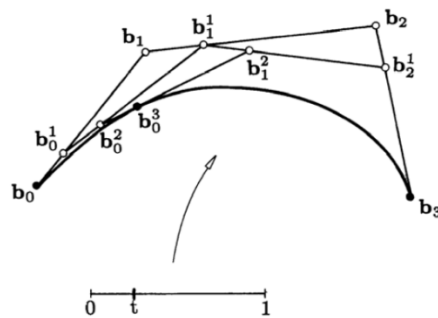


Figure 2.4.10. The de'Casteljau Algorithm: The Point $b_0^3(t)$ is Obtained From Repeated Linear Interpolation

With focus on the cubic case, the above algorithm enables the creation of a single piece of a cubic polynomial. However, the goal of the piecewise cubic spline is to connect L cubic polynomials with $C^1$ and $C^2$ continuity in the joints, where 3L+1 Bezier control points are redundant, since they define N pieces of individual but connected cubic curves which are not necessarily continuous. The piecewise cubic B-spline provides a solution. Given L-3 control points (called de'Boor points), we can find 3L+1 Bezier control points from de'Boor points, meanwhile the Bezier curves satisfy $C^1$ and $C^2$ continuity [Farin, 1988]. In figure 2.4.11, it is clear to see how de'Boor points give rise to Bezier points, and Bezier points span the B-spline.
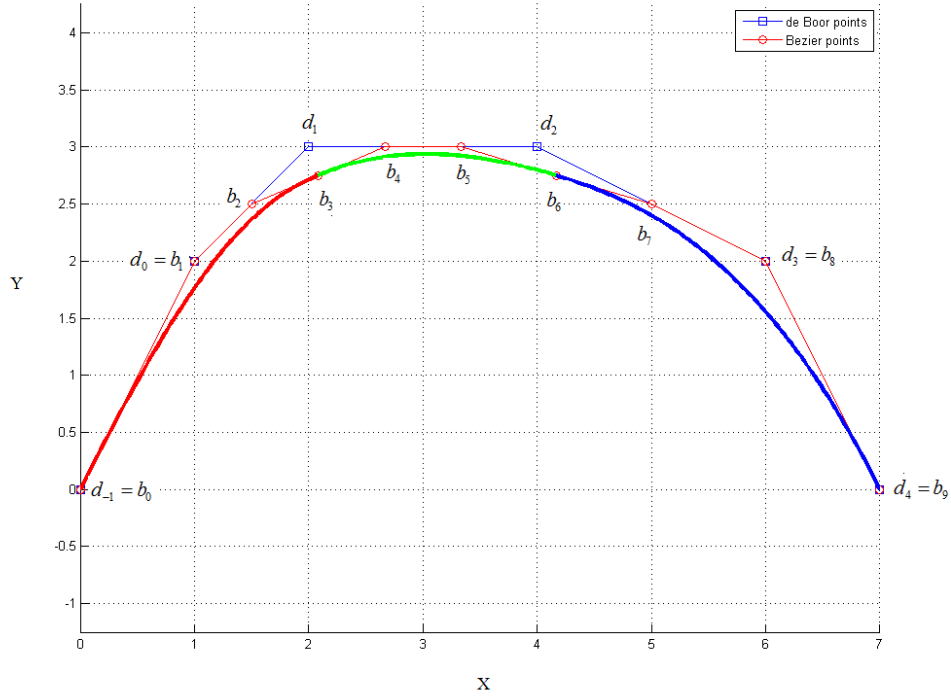
Figure 2.4.11. 3-Pieced Cubic B-spline Curve with its Control Polygon

The approach trajectory is defined in the ship heading frame with its starting point at the helicopter's current position and end point at the hover location over the ship deck. To obtain a trackable trajectory, the following properties are desired:

- The trajectory slope agrees with the helicopter flight direction at the start and prescribed approach angles at the end of the trajectory.
- Trajectories satisfy curvature constraints subject to helicopter maneuverability
- Trajectories are as short as possible to minimize approach time
- Trajectories are friendly in saving power consumption and actuator duty cycles
- Trajectories avoid obstacles or hazards
- Other optimum or constraint criteria

The spatial trajectory reduces into two planar trajectories in the horizontal and vertical plane as shown in Figure 2.4.13. In the meantime, path properties can be expressed in planar parameters, table 2.4.1 summarizes the most important metrics.
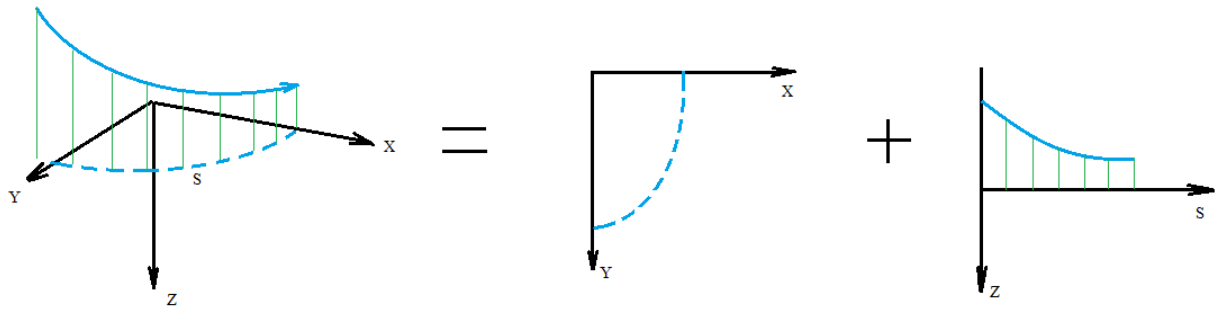
Figure 2.4.12. Decomposition of 3D Trajectory

| Spatial path properties | Horizontal navigation | Vertical navigation |
|---|---|---|
| Initial angle | Current Flight Path Angle | Current Flight Heading Angle |
| Final angle | $\psi_{app}$ | $\gamma_{app}$ |
| Path curvature constraint | Maximum turn rate | Maximum and minimum load factor |
| Path length | Horizontal path length | Vertical path length |
| Power and Actuator Duty Cycle | Lateral cyclic control, TR collective control | Longitudinal cyclic control, MR collective control |

Table 2.4.1 Spatial Path Properties

From the above discussion, a universal 2D algorithm can be designed for both horizontal and vertical path generation. Six de'Boor control points (d1,d2,d3,d4,d5,d6) are used to define a planar B-spline. The points $d_1$ and $d_6$ are naturally fixed at helicopter position and hover point over ship deck which is defined as the ship heading frame origin (0,0). The other four internal points $d_2$ - $d_5$ are initialized as points equally spaced in a straight line between $d_1$ and $d_6$. The optimization algorithm drives internal de'Boor points $d_2$ - $d_5$ to achieve a minimal value of the following objective function:

$$J = w_1 \left| \theta_{ini} - \theta_{inides} \right| + w_2 \left| \theta_{end} - \theta_{enddes} \right| + w_3 \bullet L_{tot} + w_4 \bullet N_{curv} + w_5 \bullet TVC + other$$

Where:

$\theta_{ini}$ : initial tangent angle of B-spline path

$\theta_{inides}$ : desired initial tangent angle

$\theta_{end}$ : end tangent angle of B-spline path

$\theta_{enddes}$ : desired end tangent angle

$L_{tot}$ : total length of path

$N_{curv}$ : number of path data points violating curvature constraint

$TVC$ : total variation of curvature characterizing the smoothness of path, $\sum\limits_{i=1}^{i=Np} \left| \rho_i - \rho_{i-1} \right|$ , for straight line or circle, it's zero

$w_1$ - $w_5$ : weighting factors

A quickly converging gradient descent method is used to search for the optimal trajectory subject to given constraints, initial de'Boor control points are equally distributed between start and end points. A typical scheme of de'Boor control points migration and final trajectory shape is shown in figure 2.4.13.
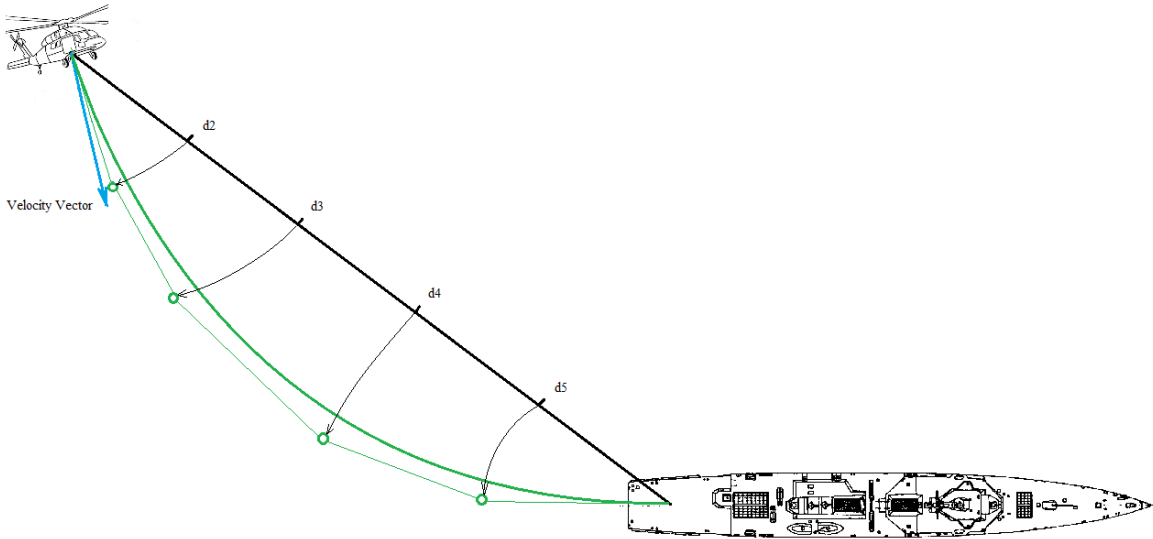


Figure 2.4.13. Scheme of Migration of de'Boor Control Points During Path Optimization

Applying the 2D planar path optimization algorithm to both the horizontal and vertical plane results in a 3D spatial trajectory. This trajectory serves as the reference position for tracking control. The control law also requires a velocity reference, which can also be generated by optimization, however here Heffley's mathematical formulation of the velocity profile is used (as it was for the straight in approach profile). Figure 2.4.14 and Figure 2.4.15 demonstrate the shape of a planned path and the associated velocity profile.
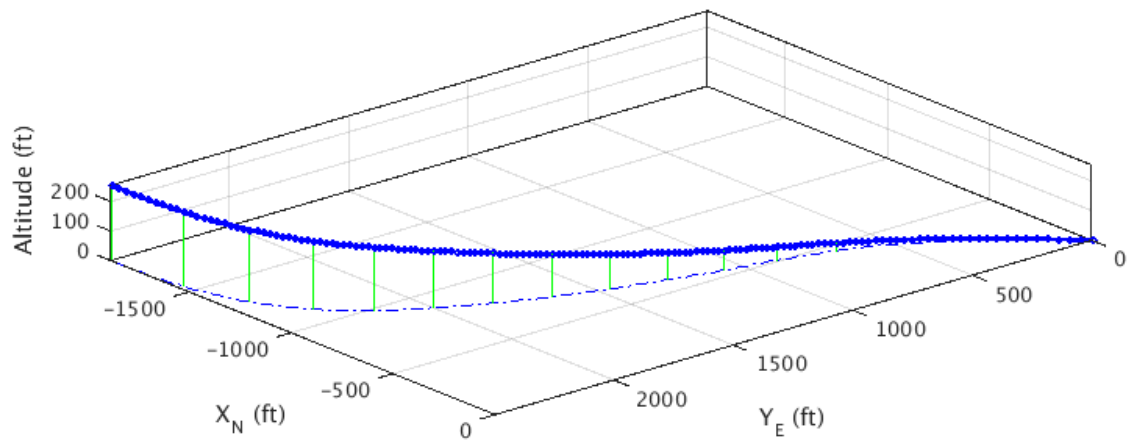
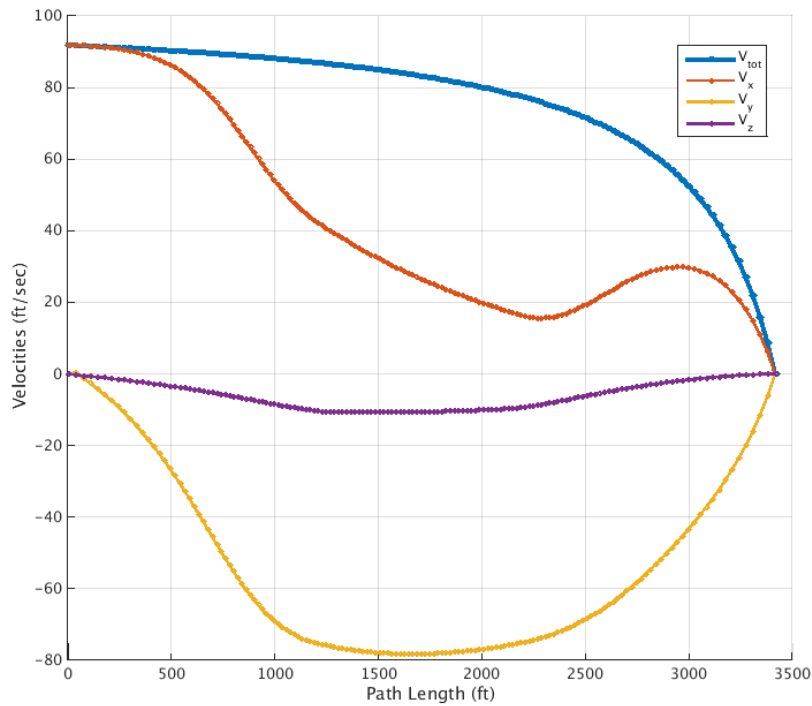Figure 2.4.14. Position Reference in Ship Heading Frame



Figure 2.4.15. Velocity Reference in Ship Heading Frame vs. Path Length

An interpolation algorithm is needed to find a unique position and velocity corresponding to the current helicopter location. For the navigation task, a nearest interpolation method is used. Path sampling points L and R are the two closest points to the helicopter; reference point P is defined as the

projection of the helicopter to a straight line connecting L and R as demonstrated in Fig 2.4.16. Thus reference position and velocity could be determined by a simple linear interpolation law:

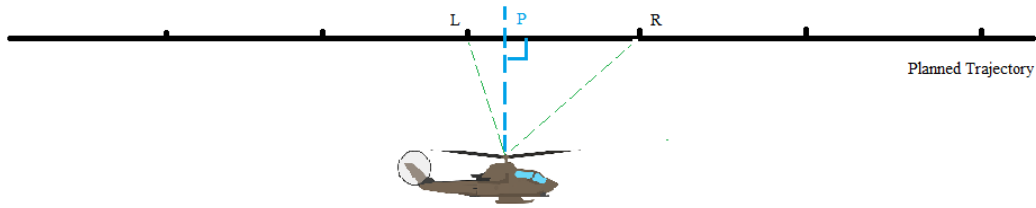$$f_p = f_L \frac{PR}{LR} + f_R \frac{LP}{LR}$$



Figure 2.4.16. Reference Position Search Scheme

### 2.4.4.3  Deck Motion Filter

The final reference of position and velocity for tracking is in fact defined in Earth Frame, which is obtained by converting reference parameters from SHF to NEU and then adding ship motion [2]. However, on approach it is not desirable to track the dynamic motion of the flight deck due to sea state, so the deck motions are filtered to yield an estimation of the steady trajectory due to ship course and heading. Ship motion has different properties in each channel, in the longitudinal direction, $X_{ship}^{NEU}$ can be continuously increasing with an almost steady speed like a ramp signal, a $2^{nd}$ order low pass filter in Figure 2.4.17 is capable to track it with small steady state error.   The tunable frequency parameter w1 varies from 0.1 to 100 as helicopters get closer to hover point, so that the full ship motion can be followed during station keeping.
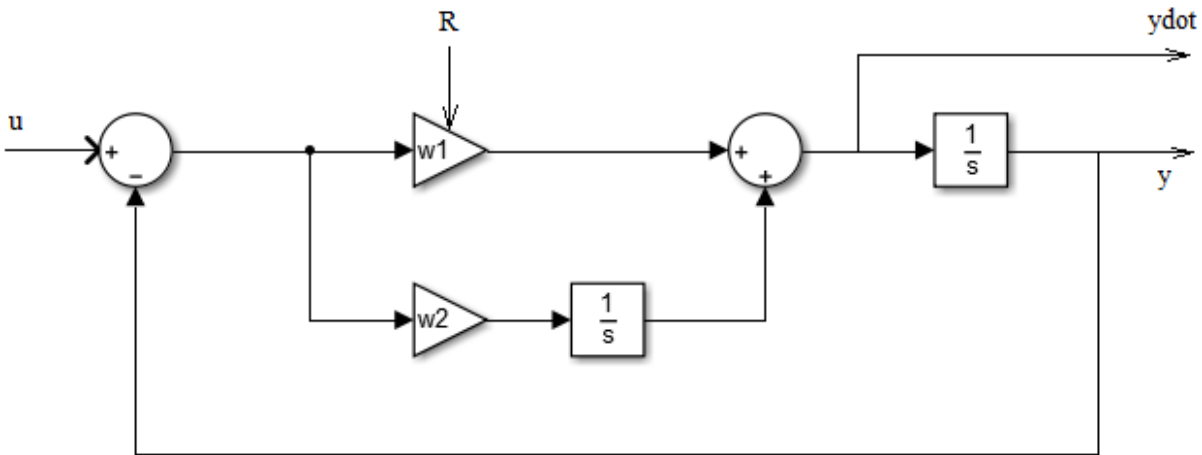


Figure 2.4.17.  $2^{nd}$ Order Low Pass Filter with Tunable Parameter

The lateral, vertical displacement and heading angle demonstrate oscillatory properties about a mean value due to the sea state. Therefore, a $1^{st}$ order low pass filter with tunable parameter $w$ in Figure 2.4.18 is applied.
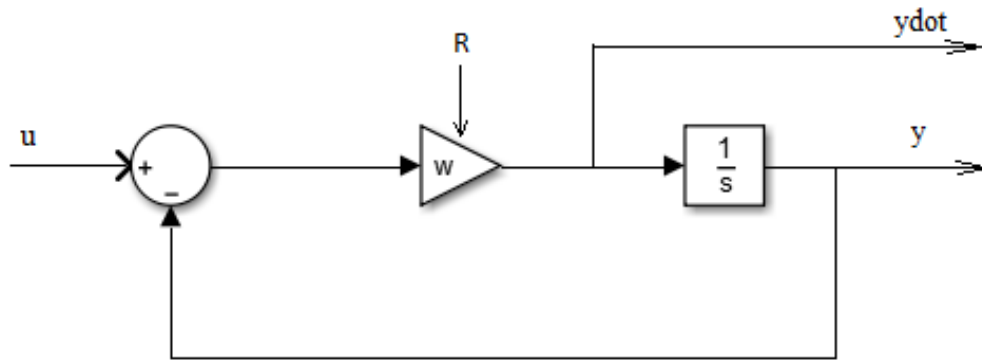
Figure 2.4.18. 1$^{st}$ Order Low Pass Filter with Tunable Parameter

### 2.4.5 Sample Simulation Results

The full autonomous controller has been extensively tested on all three rotorcraft models. Sample simulation results are shown here for three different approaches for each of three rotorcraft classes: light, medium, and heavy.

The simulation results demonstrated in Fig 2.4.19-Fig 2.4.23 are based on the light class helicopter. The helicopter starts the approach at 2500 ft from behind the deck with airspeed 125 ft/sec, the initial altitude is 300 ft.
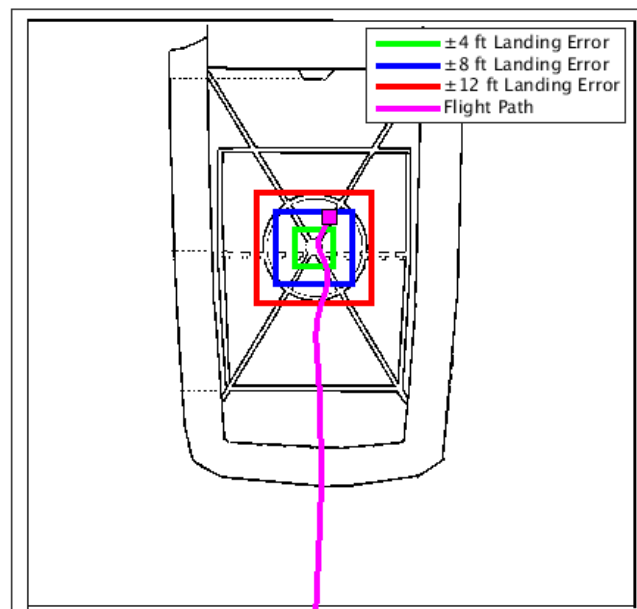


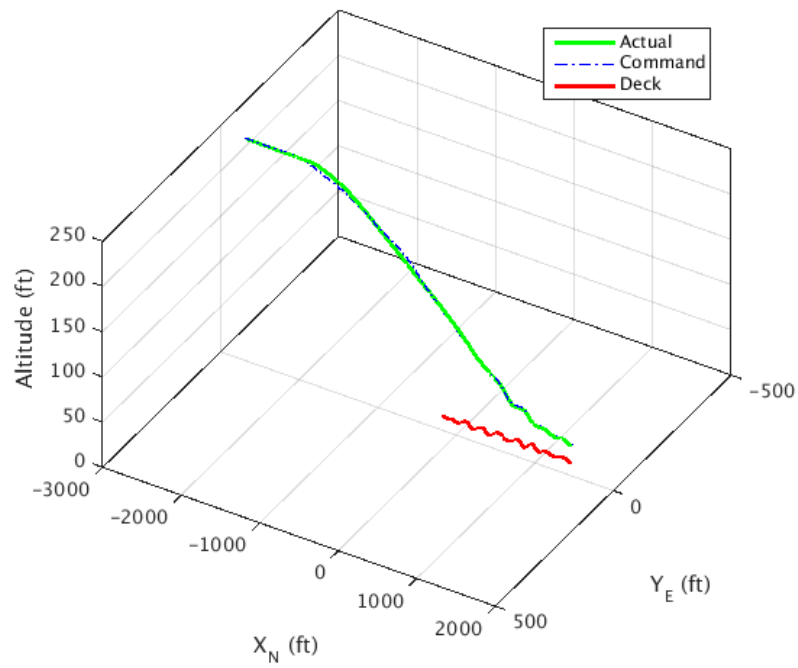Figure 2.4.19. Top-View of Approach Path
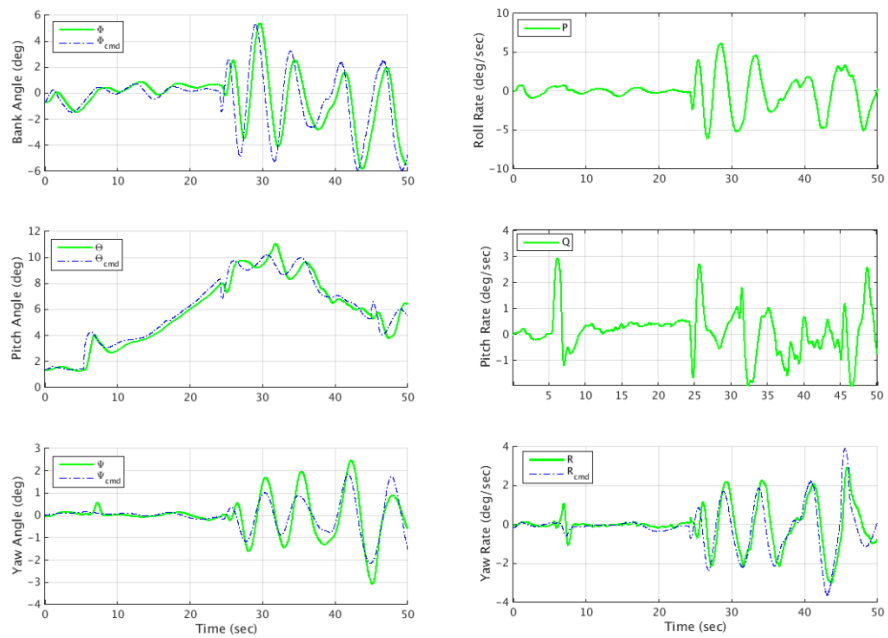
Figure 2.4.20. 3D plot of Approach Trajectory
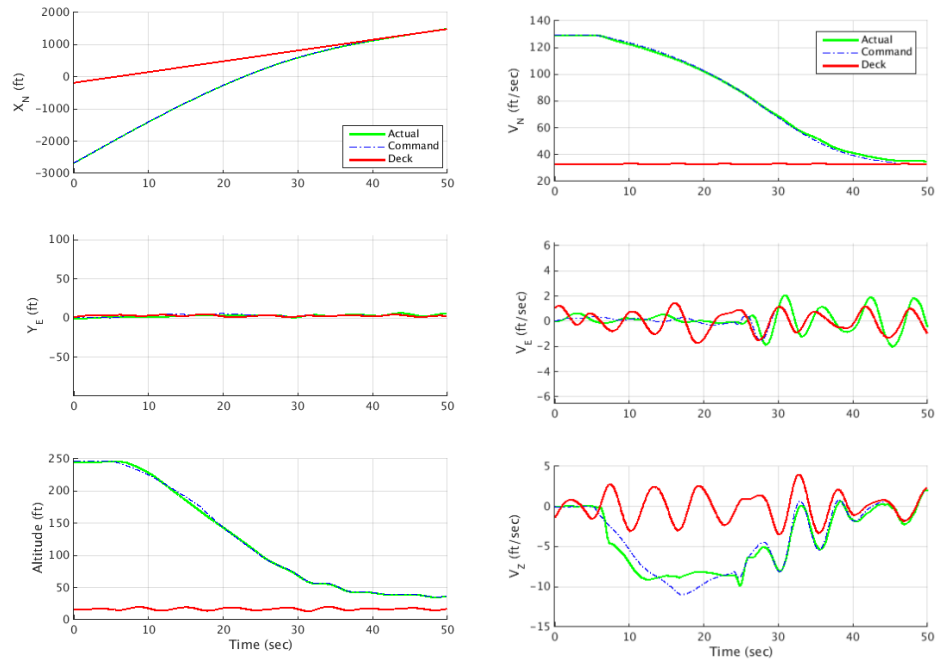


Figure 2.4.21. Attitude Angles and Attitude Rate

Figure 2.4.22. Position and Velocity Tracking History



Figure2.4.23. Control Effort

The next set of simulation test results are performed on the medium class helicopter model. The curved path generation was enabled in this test. The approach azimuth angle was set to be $45^{\circ}$, all the other conditions are the same as those used for the light class in the previous set of results. The non-linear simulation results are demonstrated in Fig 2.4.24-Fig.2.4.28.
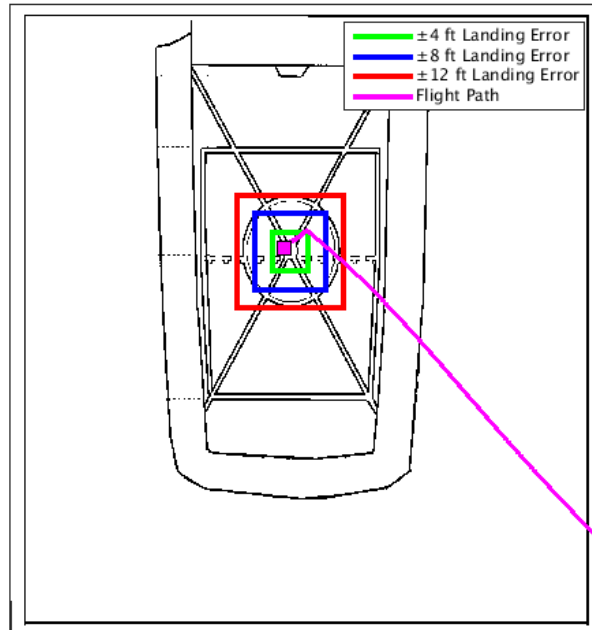


Figure 2.4.24. Top-View of Approach Path
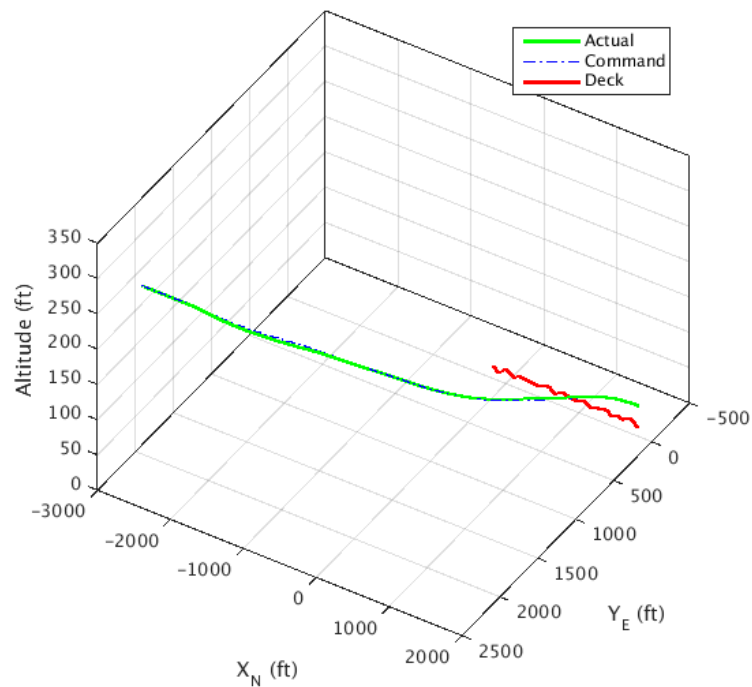


Figure 2.4.25. 3D Plot of Approach Path

Figure 2.4.26. Attitude Angles and Attitude Rate
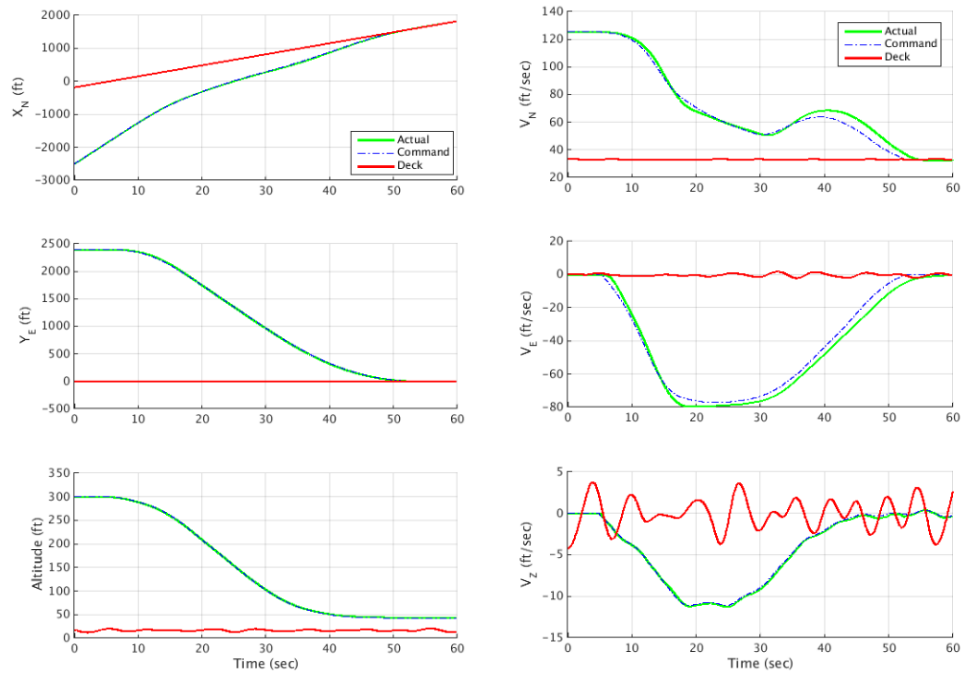
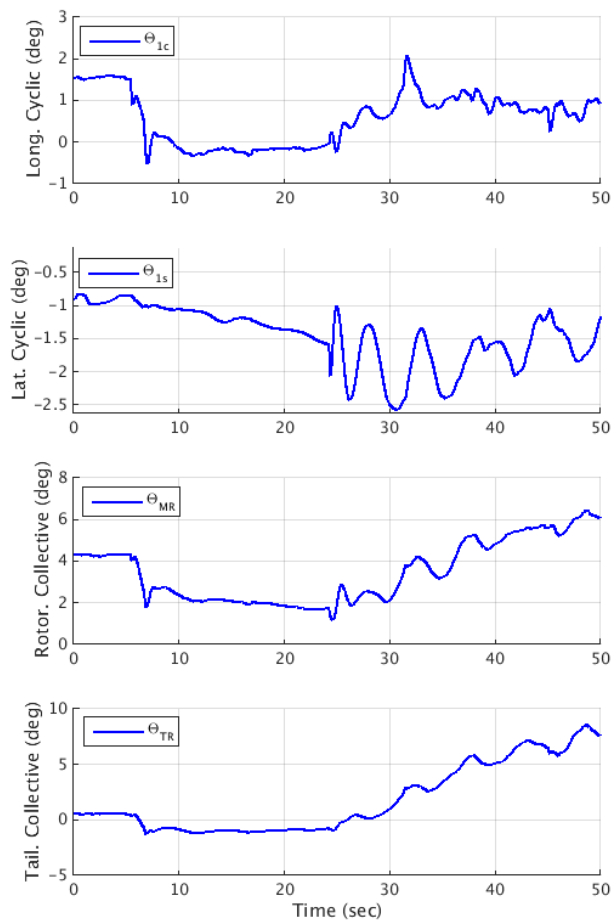

Figure 2.4.27. The Position and Velocity Tracking History
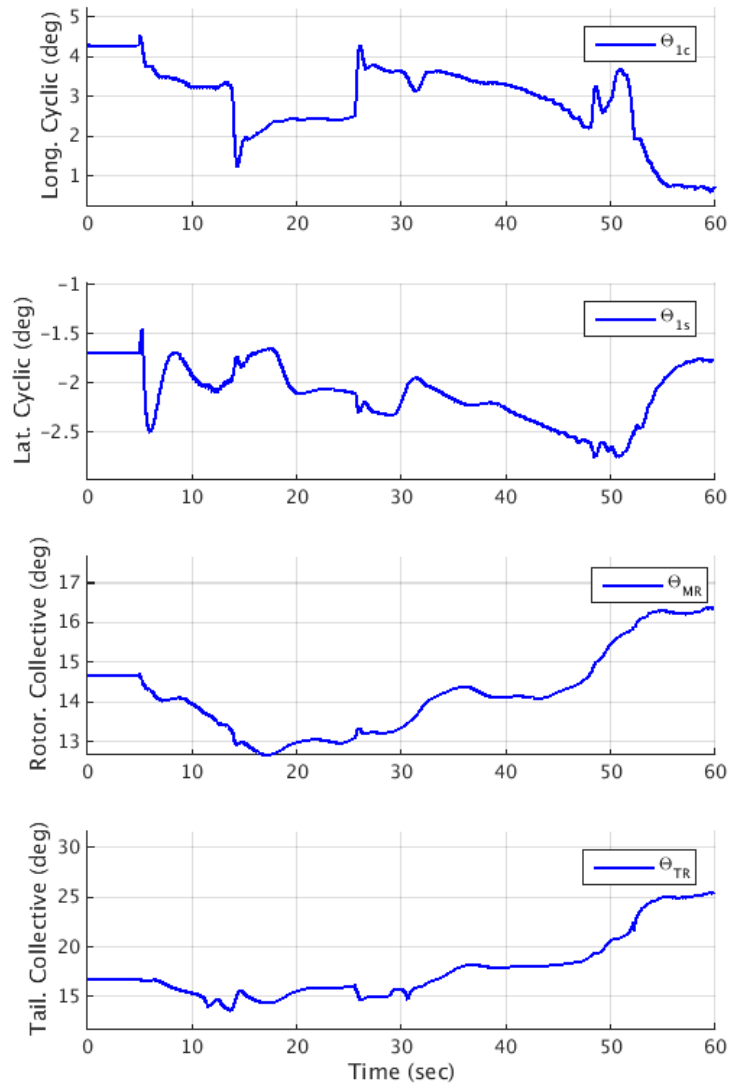
Figure 2.4.28. Control Effort

The third simulation test was carried out with heavy class model using curved path algorithmn to generate approach trajectory. All the test conditons are the same with $2^{nd}$ test, exept the approach came with azimuth angle of -45$^o$. Simulation results are represented in Fig 2.4.29 – Fig 2.4.32

Figure 2.4.29. Top View of Approach Path
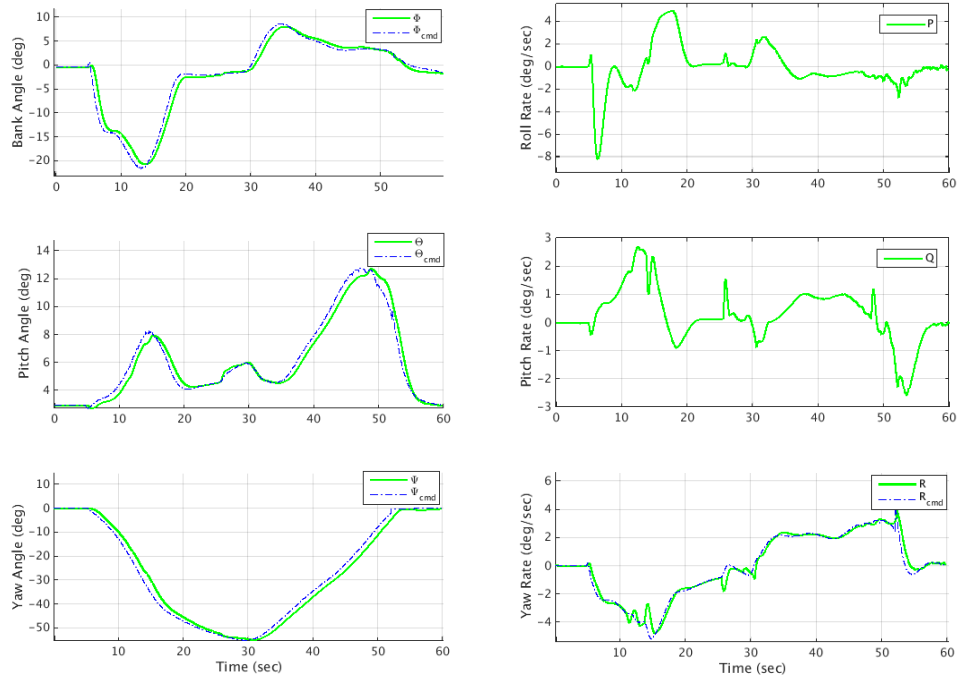


Figure 2.4.30. 3D Plot of the Approach Path

Figure 2.4.31. Position and Velocity Tracking Performance
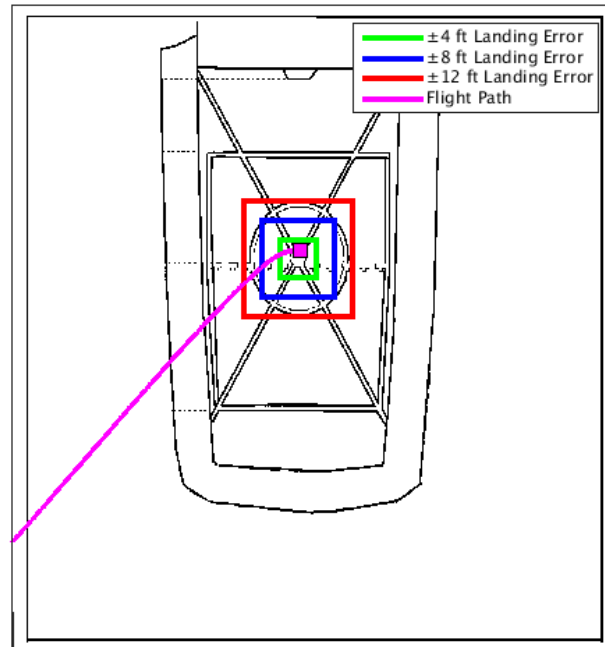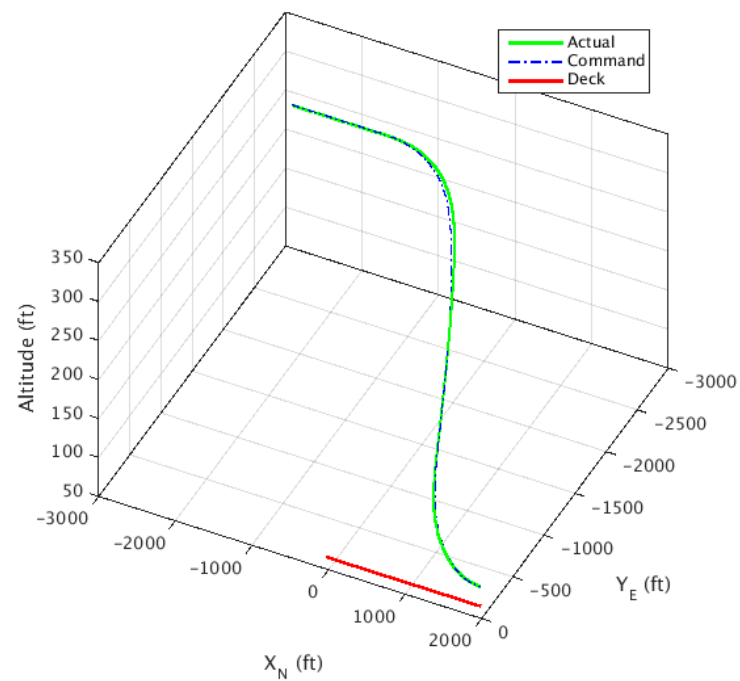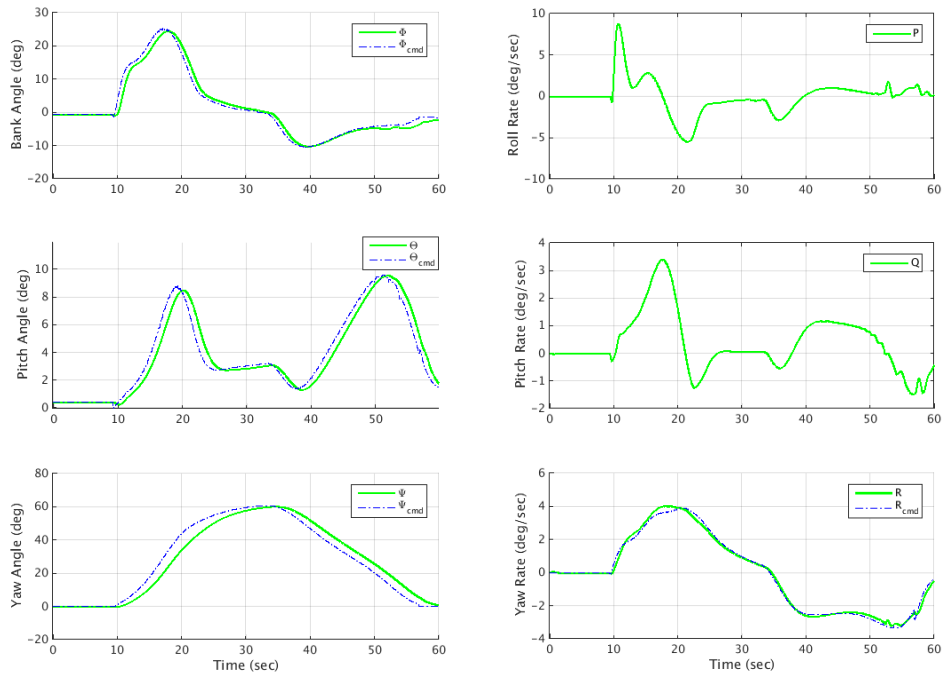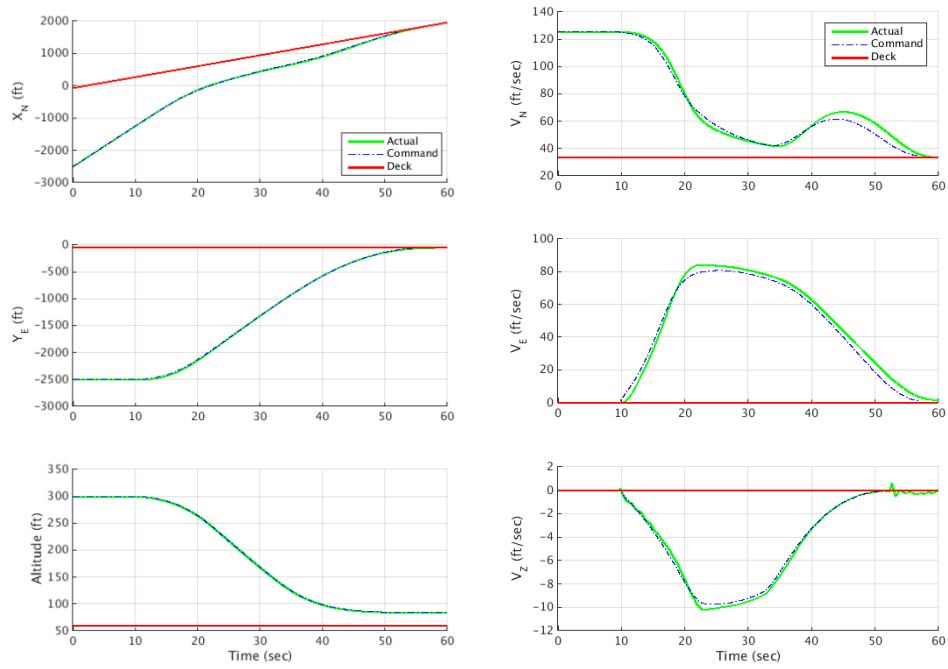


Figure 2.4.32. The Position and Velocity Tracking History

Simulations with various test conditions on different classes of helicopter demonstrate the capability of the developed guidance and control law in working with different Aircraft platforms. Good tracking performance of spatial position proved the potential of the control system to be implemented in the shipboard recovery task.

## 2.5   Task 5 Ship Deck Motion Prediction

Ship deck motion forecasting provides a good opportunity for a shipboard rotorcraft controller to take advantage of using advanced control laws (such as a robust feed-forward control) for a safe shipboard landing under high sea states. Efforts were made in this reporting period to investigate dynamic forecasting methods and to formulate a ship deck motion forecast framework to support the development. The ship deck motion forecasting framework under development includes 1) the forecasting algorithm formulation and implementation, 2) the test condition formulation for ship motion time history data generation; 3) evaluation criteria for the prediction accuracy measurement.

A group of auto-regression and moving average algorithms for dynamic forecasting based on past time history data was studied. A Holt-Winters (H-W) algorithm (Markridakis 1998) was selected for initial testing. The H-W algorithm predicts the future variation based on an online adaptive update of the mean, the trend, and the cyclic characteristic from past time history.  The algorithm adopts a smoothing technique with weight decaying exponentially with older observations and, therefore, places a much heavier weight on using the most recent information for the forecast. Efforts were made to implement a Holt-Winters (H-W) method. Although it provided a reasonable prediction for a short amount of future time, the algorithm had difficulty predicting a longer time period due to the requirement of "seasonal cycle" input which defines the deterministic trend term of a given signal. Since the ship motion is an inherently random process (even though a set of dominant periods can be extracted), the H-W algorithm may not be the best choice for the current task. Therefore, efforts were made to investigate an alternative method, a minor component analysis (MCA) method.

The minor component is the direction in which the data has the smallest covariance. The statistical method for extracting a minor component from the input data is called minor component analysis. The MCA determines the directions of smallest variance in a distribution. They correspond to the directions of those eigenvectors of the covariance matrix of the data which have the smallest eigenvalues. The main idea of MCA was applied for a curve fitting problem (Oja 1992). Usually, the least squares method is used to solve such problems.  For example, given a set of data points ($x_1$, $x_2$), the problem of having a line model to fit the data in the usual least square sense becomes the problem of finding a pair of estimates. If it is assumed that only the measurements $x_2$ contain errors while the measurements $x_1$ are accurate, the total least squares approach gives the optimal way to minimize the sum of the squared lengths of all the bars which are perpendicular to the estimated line. The total least squares fitting problem can be reduced to the problem of finding the minimum eigenvalue and its corresponding normalized eigenvector of matrix or, in other words, finding the first minor component of the data set.

To implement the MCA method, a set of ship motion data is aligned into a sequence of vectors, $X_i$. The eigenvalues and eigenvectors of the autocorrelation matrix, $R = \sum_{i=1}^{N} X_i X_i^T$, can then be calculated. The vector $X_i$ is formed as $[X_{1i}, X_{2i}]^T$. where $X_{1i}$ is the measured ship motion and $X_{2i}$ is the forecasted motion in the length of the forecasting window. Based on the MCA algorithm, the forecasted vector ($X_{2i}$) is calculated using an approximated equality formulation consisting of eigenvectors which are associated with the smallest eigenvalues of the autocorrelation matrix ($R$). In addition, a multi-block method was used where the data are organized in multiple sampling blocks with offsets from each. The MCA algorithm was then applied to each data block with adaptation to generate the forecasting for that block. The outputs from each block were then combined from the multi-block prediction to result in the forecasting. Figure 2.5.1 illustrates the MCA based multi-block method.
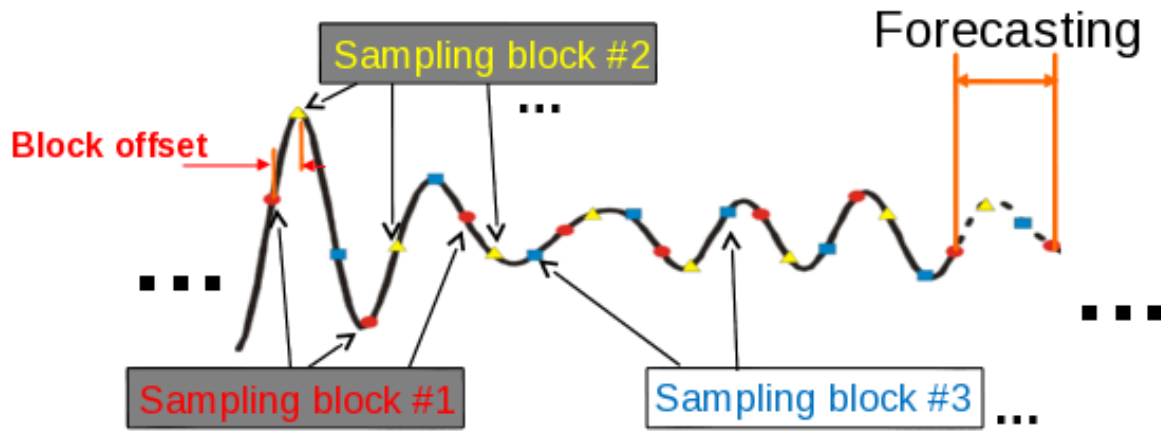


Figure 2.5.1 MCA based multi-block forecasting method

For simulation tests of the MCA based ship motion forecasting algorithm, a set of ship motion data is required. Although it is best to use measured ship deck motion data for the simulation tests, the ship motion outputs from USN SMP and STH are used for the current research because of a lack of measured data. The full 6-DOF motion (surge, sway, heave, roll, pitch, and yaw) is considered in response to the variation of the sea state wave conditions, the wave heading angle, and the ship speed. Given a sea state, ship speed, and wave heading angle, the ship motion is generated by sweeping the significant wave height and the wave modal period over the range as defined by a sea state table. For this research, two classes of ship model, DDG-81 class and LHA class, were used to generate the ship motion data. A total of 1,260 test cases was generated for each ship class. Each set of test conditions is a combination of (a) three sea states (3, 5, and 6), (b) two ship speeds (10 and 20 knots), (c) ten wave heading angles (0, ±30, ±60, ±90, ±135, ±180 degrees), (d) five significant wave heights for each given sea state, and (e) four wave modal periods for each given sea state. The significant wave heights and the wave modal periods were arbitrarily selected from the NATO Sea State Numeral Table for the Open Ocean North Atlantic in order to simulate a greater variety of ship motions.

The 6-DOF landing deck motions were sampled at a 10 Hz rate for each test case. It should be noted that Landing Spot 8 was used for the LHA class ship. The current MCA based ship motion forecasting algorithm was set to predict the deck motion up to 6 seconds ahead considering the accuracy and computational complexity. Further research will be required to enhance the overall performance. Approximately the first 1,500 points of deck motion data were used for the MCA algorithm training and the remaining 8,500 points were used to test the proposed forecasting algorithm. The minor components of the autocorrelation matrix were selected such that their energy added up to no more than 1% of the total energy. Figure 2.5.2 shows the sample time history comparison with 6 seconds of forecasted values of the DDG-81 class ship for the following cases: sea states 3 and 5, a ship speed of 20 knots, and a wave heading angle of 0 degrees. The black solid lines represent the actual ship motions and the red dashed lines are the forecasted values.

In order to provide a quantified performance criterion, several statistical terms were used. From the initial testing, it was observed that the forecasting error variations in terms of standard deviation are very close to a normal distribution. Thus, a range of forecasting error was calculated such that the forecasted deck motion was within 90% of its real value. For example, if a range of forecasted error is wide, then the forecasting performance is not acceptable. In addition, the significant amplitude, which is based on a concept similar to the significant wave height, was defined to represent the nominal level of ship motion. The significant wave height is a statistical term that represents the average of the highest 1/3 of the waves in a given wave train. Since it is known that about 16 percent of the waves will be higher than the significant wave height, it is suitable for illustrating the sea condition. Similarly, the ship motion can be quantified using the significant amplitude (e.g., significant heave, significant roll, etc.). Figure 2.5.3 shows the corresponding quantified performance of the forecasting algorithm for the same simulation condition. Figure 2.5.4 shows the simulation results using an LHA class ship for the same simulation condition. It can be seen that the forecasting error increases when the sea wave heading angles are close to the port and starboard sides of ship due to the highly coupled roll and pitch motion. This is because of the loosened correlation of the matrix $R$. In fact, one of the default procedures of helicopter shipboard landing is to align the ship with respect to the wave heading angle. From the figures, the MCA forecasting algorithm forecasted the ship motion reasonably well for wave heading angles between ±45 degrees, which satisfies the requirements of the current task. In addition, it can be observed that the forecast algorithm performs very well for relatively smaller ship motions, such as low sea state condition and heavier ship. It should be noted that the forecasting accuracy is significantly improved for shorter forecasting time and it is useful for a deck motion feedback controller (see Figure 2.5.5). The prediction horizon of the algorithm is nominally set to 5 seconds, but it can be adjusted in real time during flight. The expected strategy is to shorten the prediction horizon during the landing sequence to predict deck state at the expected touchdown time. Although the prediction horizon of the algorithm can be adjusted in real time during flight, the forecasting algorithm was developed to have an integer forecasting horizon. In order to resolve this issue, the MCA-based deck motion prediction algorithm with multiple prediction horizons (e.g., 1 sec, 2 sec, 3 sec, 4 sec, and 5 sec) has been developed to provide the continuous ship motion prediction using a linear interpolation method.
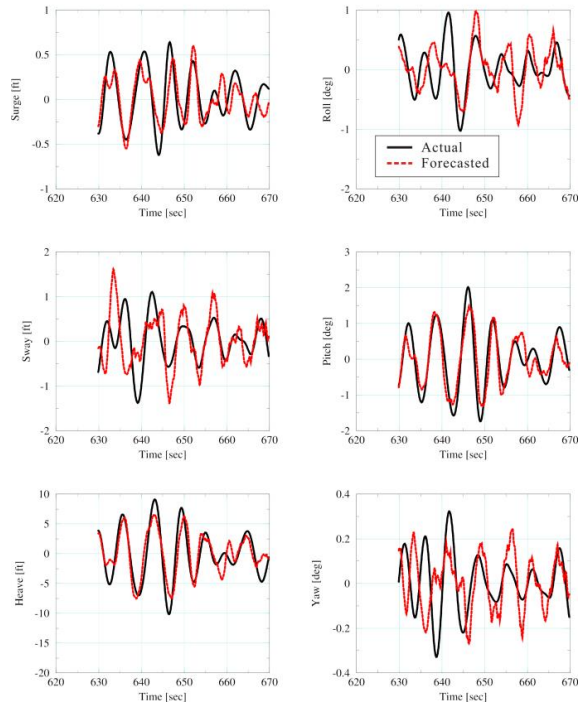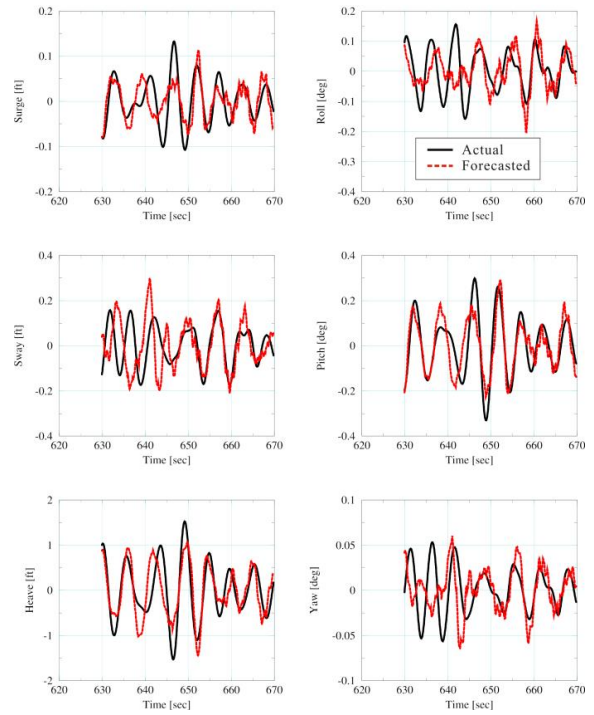
Figure 2.5.2 Comparisons of time responses of forecasted 6-DOF ship motion (DDG-81 class)

Ship Type: DDG-81 Class (Landing deck)    Sea state : 5
Ship speed (knots): 20                    Forecasted time (sec) : 6

Ship Type: DDG-81 Class (Landing deck)    Sea state : 3
Ship speed (knots): 20                    Forecasted time (sec) : 6



(a) sea state : 5                          (b) sea state : 3

Figure 2.5.3 Quantified performance criteria (vs wave heading angle) - DDG-81 class

Significant amplitude and MCA based forecasted error (90% tolerance)

Ship Type: LHA Class (Landing Spot 8)    Sea state : 5
Ship speed (knots): 20                    Forecasted time (sec) : 6

Significant amplitude and MCA based forecasted error (90% tolerance)

Ship Type: LHA Class (Landing Spot 8)    Sea state : 3
Ship speed (knots): 20                    Forecasted time (sec) : 6



(a) sea state : 5                                    (b) sea state : 3
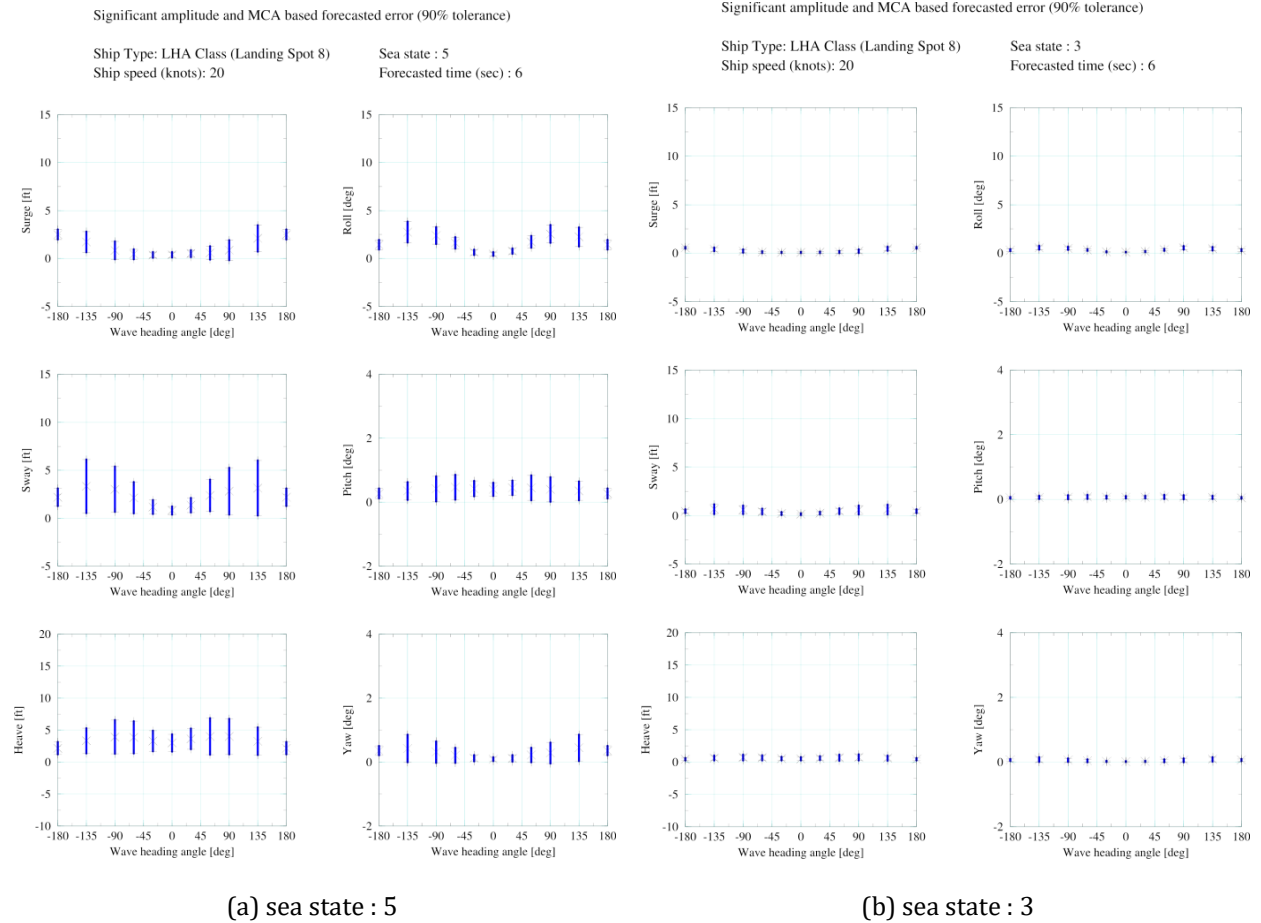
Figure 2.5.4 Quantified performance criteria (vs wave heading angle) - LHA class

Significant amplitude and MCA based forecasted error (90% tolerance)

Ship Type: DDG-81 Class (Landing deck)    Sea state : 5
Ship speed (knots): 20                     Forecasted time (sec) : 3
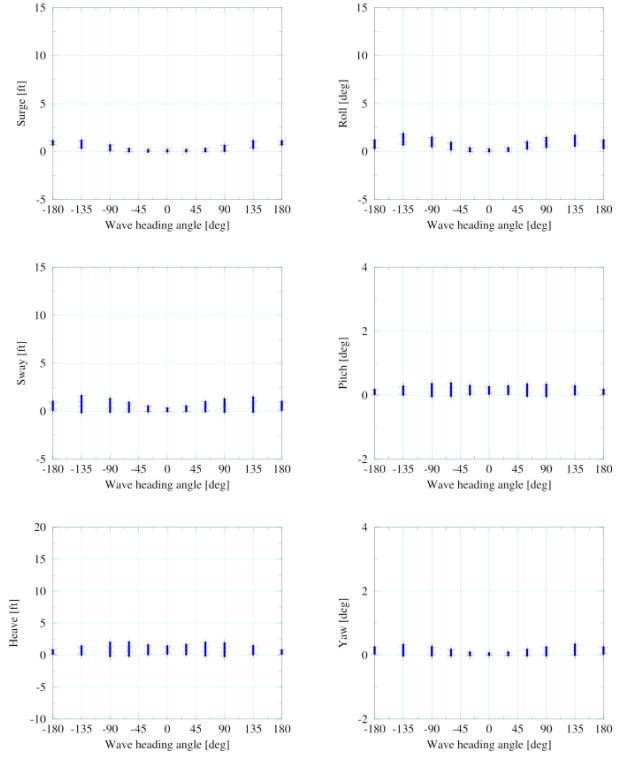
Significant amplitude and MCA based forecasted error (90% tolerance)

Ship Type: LHA Class (Landing Spot 8)     Sea state : 5
Ship speed (knots): 20                     Forecasted time (sec) : 3

(a) DDG-81 class                    (b) LHA class
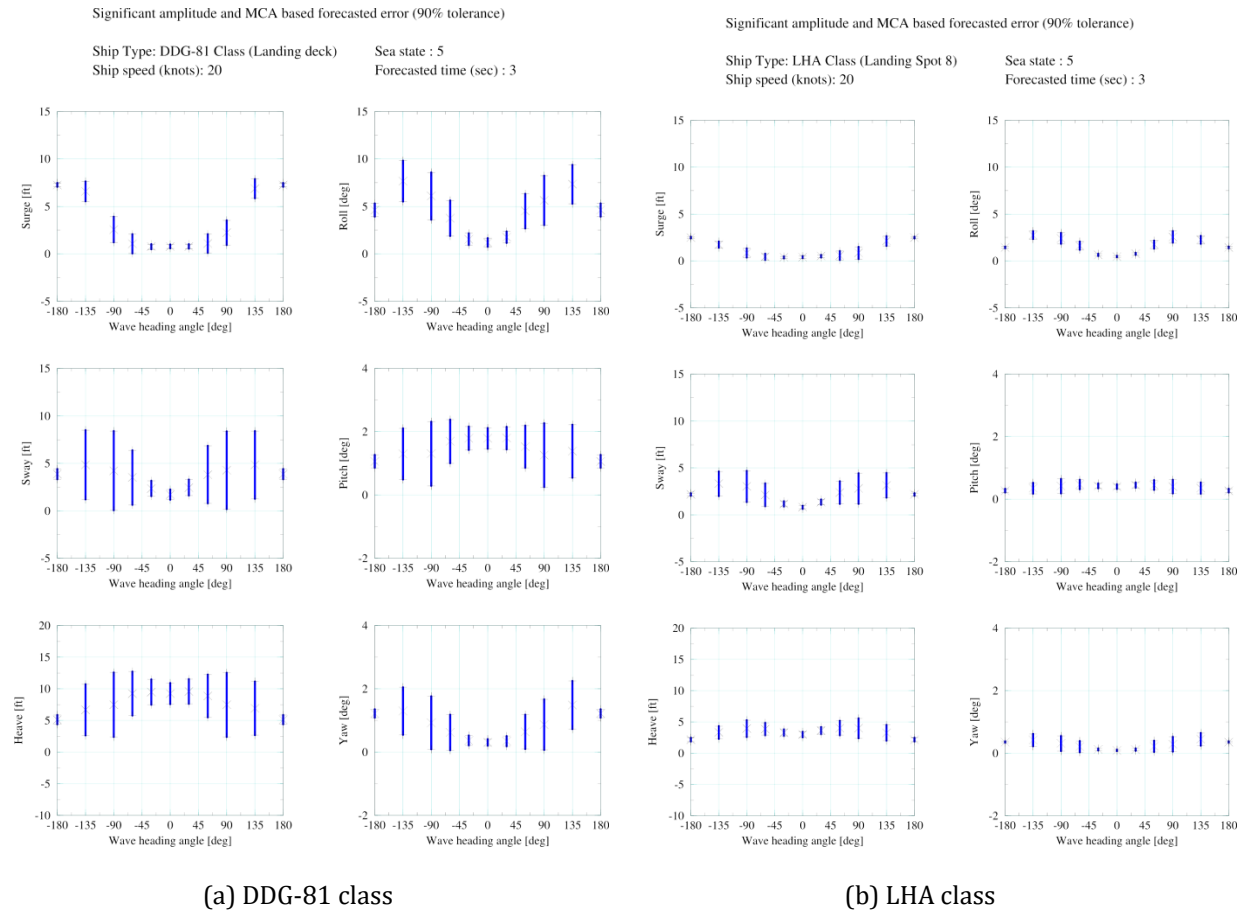
Figure 2.5.5 Quantified performance criteria for 3 second forecast

## 2.6    Task 6 Path optimization of shipboard helicopter

An essential element of an autonomous landing system is the ability to self-generate a suitable (perhaps optimal) path in space and time with acceptable computational expense.  A variety of path planning algorithms for rotorcraft unmanned aerial systems (UASs) have been proposed in recent research, and one class of path planning algorithms involves the use of numerical optimization methods.   The use of numerical optimization for addressing the path planning problem is well established for manned aircraft, and it has been applied to challenging rotorcraft aeromechanics problems in recent years, such as brownout and autorotation.

The general objective of Task 6 was to develop and demonstrate, through simulation, a methodology for determining path guidance for helicopter shipboard recovery within a numerical optimization framework.  In this section, results from two simultaneous optimization studies are presented that demonstrate the development of objective functions that incorporate multiple performance factors, such as 1) the maneuver duration, 2) the power requirements over the course of the maneuver, 3) path error along the maneuver, and 4) the effects of the turbulent ship airwake.

### 2.6.1 Simulation Overview

For the initial path optimization study, the medium class helicopter was used, with the Dynamic Inversion control law as described in Section 2.4. Within this control architecture, a path following control law was developed to autonomously track a three-dimensional trajectory. The controller is designed to track a smooth, continuous trajectory defined by a kinematically consistent set of position, velocity and acceleration commands. The control law uses a dynamic inversion scheme to produce command roll and pitch attitudes, yaw rate commands, and vertical speed commands that are then fed to the inner-loop control system.

These studies did not use dynamic ship models (so the ship moves at steady speed in calm waters with no roll or pitching of the deck). This allowed the study to focus on airwake effects. The ship airwake is modeled with a non-uniformly-distributed mean disturbance plus a stochastic turbulent airwake variation, as derived from CFD solutions of the flow over the SFS2 generic frigate shape. Simulations in the present study were performed for approaches to a ship moving at 20 kts in calm winds (i.e., 20 kts wind over deck, 0° relative wind).

### 2.6.2 Optimization Framework

In the present study, the shipboard approach is formulated mathematically as a numerical optimization problem and cast into nonlinear mathematical programming form. The general optimization procedure consists of finding the value of a vector of design variables $X$ such that a scalar objective function $F(X)$ is minimized; that is,

$$F(X) \rightarrow \min \tag{2.6.1}$$

$$\text{subject to: } g_j(X) \leq 0 \quad j = 1,...,m \tag{2.6.2}$$

$$X_{\min} \leq X \leq X_{\max} \tag{2.6.3}$$

In practice, the optimization problem is converted into a sequence of approximate optimization problems in which the objective function is replaced by function approximation $F_{\text{app}}(X)$.

#### 2.6.2.1 Approach Profile Design Vector

The approach profile utilized in the present study is an extended version of Heffley's mathematical formulation of longitudinal deceleration and velocity profiles for a visual helicopter approach; that is,

$$\ddot{r} = \frac{(v_0/2r_{\text{pd}})^2 r}{(1+r/2r_{\text{pd}})^3} \tag{2.6.4}$$

$$\dot{r} = \frac{(v_0/2r_{\text{pd}})r}{(1+r/2r_{\text{pd}})} \tag{2.6.5}$$

where $v_0$ is the asymptotic velocity and $r_{pd}$ is the range from the landing spot at which peak deceleration occurs. Representative profiles are shown in Fig. 2.6.1. Notice that $v_0$ and $r_{pd}$ drive the aggressiveness of the approach profile; as $v_0$ increases and $r_{pd}$ decreases, a more severe deceleration is required to yield zero forward speed at the approach termination. A benefit of this formulation is that it is based upon only two parameters; the simplicity of the formulation makes it ideal for preliminary investigations.
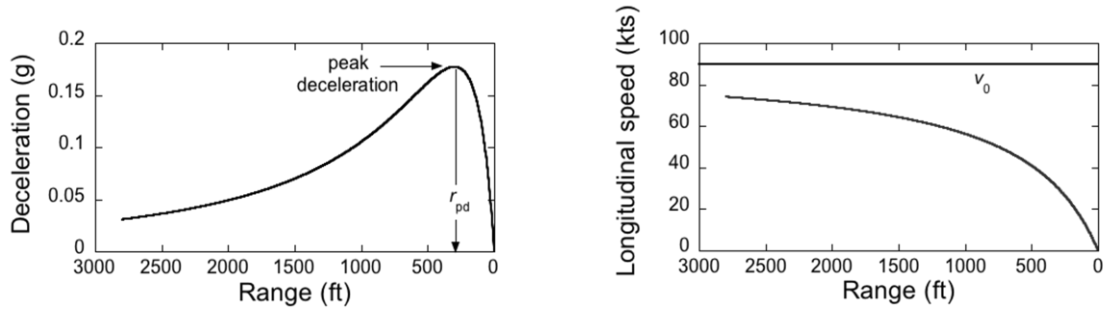
a) Deceleration vs. range from landing spot          b) Speed vs. range from landing spot

Figure 2.6.1. Representative examples of longitudinal deceleration and velocity profiles for a visual

This formulation was previously extended to allow for the prescription of the approach path through a constant approach angle, $\gamma$; that is,

$$\dot{h} = \dot{r} \tan(\gamma) \qquad (2.6.6)$$

where $\dot{h}$ is the vertical velocity. The approach profile was extended further in the present work to include a ship-relative azimuth angle, $\psi$. The resulting approach profile design vector consists of only four variables, i.e., $\mathbf{X} = [v_0 \ r_{pd} \ \gamma \ \psi]^T$. A schematic diagram is shown in Fig. 2.6.2. Notice that the first two variables describe the temporal approach profile, i.e., $\mathbf{X}_{\text{temp}} = [v_0 \ r_{pd}]^T$, and the second two variables describe the spatial approach profile, i.e., $\mathbf{X}_{\text{spatial}} = [\gamma \ \psi]^T$. In other words, $\mathbf{X}_{\text{temp}}$ describes the way in which the aircraft traverses the path defined by $\mathbf{X}_{\text{spatial}}$.
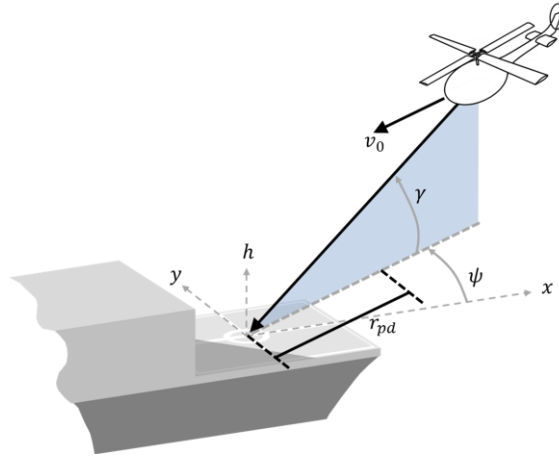


Figure 2.6.2.    Schematic diagram showing
the four approach profile design variables.

Each design variable is subjected to side constraints, Eq. (2.6.3), which, for the present study, were

$$100 \text{ ft/sec} \le v_0 \le 150 \text{ ft/sec} \tag{2.6.7}$$

$$190 \text{ ft} \le r_{pd} \le 500 \text{ ft} \tag{2.6.8}$$

$$1 \text{ deg} \le \gamma \le 15 \text{ deg} \tag{2.6.9}$$

$$-45 \text{ deg} \le \psi \le 45 \text{ deg} \tag{2.6.10}$$

It is important to notice that there are many other factors that could be included in the approach profile design vector, such as 1) yaw/sideslip angle (the present formulation assumes that the nose of the helicopter is pointed in the direction of flight), 2) aircraft gross weight, 3) wind over deck (i.e., the magnitude and azimuth), and 4) ship motion (where the proper mathematical description of ship motion remains an open research question). The inclusion of such factors may need to be addressed in future studies.

The optimization procedure began with an initial inventory of approach profile designs. The baseline approach profile was $X_1 = [v_0 \; r_{pd} \; \gamma \; \psi]^T = [125 \text{ ft/sec} \quad 300 \text{ ft} \quad 8 \text{ deg} \quad 0 \text{ deg}]^T$, and the remainder of the initial inventory of designs was based on a sensitivity study, i.e., the baseline plus a positive and negative perturbation for each of the four variables in the design vector

### 2.6.2.2 Objective Function

The objective function $F(X)$ is a quantitative description of the approach performance, where the overall performance can potentially involve a number of independent and interdependent performance factors. Multiple performance factors were considered in the present study: 1) the maneuver duration, 2) the power requirements over the course of the maneuver, 3) path error along the maneuver, and 4) the effects of the turbulent ship airwake.

First, the maneuver duration and power requirements were considered together through the work performed over the duration of the maneuver; that is,

$$W = \int_0^{t_{end}} P(t) \, dt \tag{2.6.11}$$

where $P(t)$ is the power required over the duration of the maneuver, and the work is computed by integrating the power requirements from the initiation of the maneuver to its end, $t_{end}$. A representative plot of $P(t)$ is shown in Fig. 2.6.3-a.
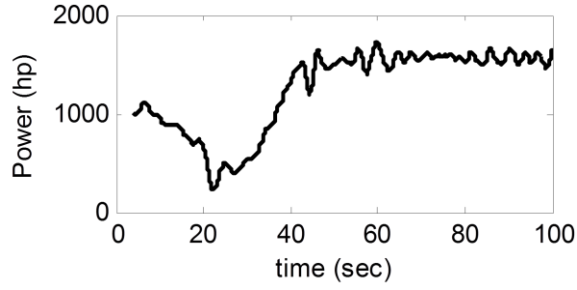
a) Power required vs. time
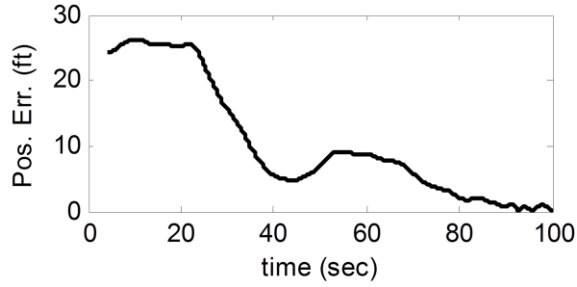


b) Position error vs. time
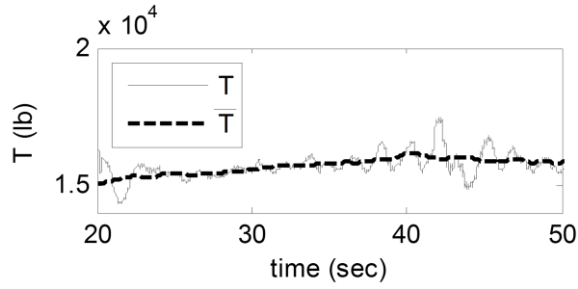


c) Thrust vs. time

Figure 2.6.3. Performance factors to be considered in the objective function.

Second, the aircraft error with respect to the commanded position was computed for the duration of the maneuver; that is,

$$\varepsilon(t) = \sqrt{(x(t) - x_{cmd}(t))^2 + (y(t) - y_{cmd}(t))^2 + (h(t) - h_{cmd}(t))^2}$$ (2.6.12)

where $x$, $y$, and $h$ are the coordinates of the aircraft position and the subscript 'cmd' denotes the coordinates of the prescribed approach profile. A representative plot of $\varepsilon(t)$ is shown in Fig. 2.6.3-b. The mean position error $\bar{\varepsilon}$ over the duration of the maneuver was selected as the performance metric to be included in the objective function for the present study, although this may need to be investigated in further studies because allowable error thresholds for a realistic mission will certainly change as a function of range from the ship.

Last, the effects of the turbulent ship airwake on the aircraft approach performance were considered. There are many different ways in which the ship airwake impacts the aircraft approach, such as uncommanded excursions in Euler angles or fluctuations in the main rotor thrust. In the present study, the ship airwake effects were quantified by the resulting thrust fluctuations. In the first instance, the time-varying thrust fluctuation was defined to be

$$\Delta T(t) = T(t) - \bar{T}(t) \qquad (2.6.13)$$

Where $T(t)$ is the instantaneous thrust and $\bar{T}(t)$ is the mean thrust computed from a five-second rolling average centered at time $t$. A representative plot of $T(t)$ and $\bar{T}(t)$ is shown in Fig. 2.6.3-c. The maximum thrust fluctuation over the duration of the maneuver was selected as the performance metric to be included in the present study.

Notice that the three performance factors included in the present study are by no means an exhaustive list, and many other factors could reasonably be included in future studies (e.g., actuator control margins). For a set of $n$ performance factors, the objective function may be formulated as

$$F(\textbf{X}) = w_1 k_1(\textbf{X}) + w_2 k_2(\textbf{X}) + \ldots + w_n k_n(\textbf{X}) \qquad (2.6.14)$$

where $w$ is the relative weight assigned to performance factor $k$, and each performance factor $k$ has been normalized such that it ranges from zero to approximately one.

Two objective functions of the form given by Eq. (2.6.14) were simultaneously evaluated in the present study. In each case, the performance factors were normalized by representative values determined from a preliminary sensitivity study. The first objective function was computed by averaging across all three performance parameters. That is, the objective function is defined by Eq. (2.6.15) with $w_1, w_2, \ldots, w_n = 1/n$:

$$F^1(\textbf{X}) = (k_1(\textbf{X}) + k_2(\textbf{X}) + k_3(\textbf{X}))/3 \qquad (2.6.15)$$

where $k_1$, $k_2$, and $k_3$ are normalized values for the work performed, mean position error, and maximum thrust fluctuation, respectively; that is,

$$k_1 = \frac{W}{2000 \text{ hp-min}} \qquad (2.6.16)$$

$$k_2 = \frac{\bar{\varepsilon}}{25 \text{ ft}} \qquad (2.6.17)$$

$$k_3 = \frac{\max(\Delta T(t))}{2000 \text{ lbs}} \qquad (2.6.18)$$

A second objective function was constructed by varying the relative weights between the different performance factors; that is,

$$F^2(\textbf{X}) = w_1 k_1(\textbf{X}) + w_2 k_2(\textbf{X}) + w_3 k_3(\textbf{X}) \qquad (2.6.19)$$

where $w_1 = w_2 = 0.1$, $w_3 = 0.8$, and the performance factors $k_1$, $k_2$, and $k_3$ are defined as they were in Eqs. (2.6.16)–(2.6.18).

### 2.6.2.3  Constraints

Behavior constraints were applied to the optimization procedure to ensure that the resulting approach profiles were both realistic and safe.  The first behavior constraint was imposed to limit the maximum pitch attitude experienced by the aircraft over the duration of the maneuver to be no more than 15 deg; that is,

$$g_1(\boldsymbol{X}) = \vartheta_{\max}(\boldsymbol{X}) - 15 \text{ deg} \leq 0 \qquad (2.6.20)$$

A second behavior constraint was imposed to prevent approach profiles in which the aircraft would be likely to descend to within 10 feet of the ship deck (the approach maneuver terminated at a height of 20 feet above the ship deck); that is,

$$g_2(\boldsymbol{X}) = 10 \text{ ft} - [\min(h_{\text{ac}}(\boldsymbol{X})) - h_{\text{deck}}] \leq 0 \qquad (2.6.21)$$

### 2.6.2.4  Approximate Problem Formulation

Because of the moderate computational cost of a shipboard approach simulation, the optimization problem was not solved by directly connecting the simulation and the optimizer.  Rather, the baseline optimization problem was converted into a sequence of computationally inexpensive approximate optimization problems in which the objective function and behavior constraints were replaced by approximations that were updated at each step of the sequence.

While a variety of approximating functions may be used in such a procedure, the method of the present study was to replace the objective and constraint functions with approximations based on a Radial Basis Function (RBF) that were generated from the exact function evaluations.  Additionally, move limits were imposed such that each design variable could not traverse more than 25% of the design space in a single optimization step; that is,

$$-0.25(\boldsymbol{X}_{\max} - \boldsymbol{X}_{\min}) \leq \boldsymbol{X}_k - \boldsymbol{X}_{k-1} \leq 0.25(\boldsymbol{X}_{\max} - \boldsymbol{X}_{\min}) \qquad (2.6.22)$$

where $\boldsymbol{X}_{k-1}$ is the best feasible design from the current inventory.

### 2.6.2.5  Additional Designs

To improve the global convergence characteristics of the methodology, additional designs were generated during the course of the optimization.  The designs computed in this way were not necessarily better designs; however, they can improve the mathematical properties of the overall optimization by improving the accuracy of the approximate objective function and improving the global convergence characteristics.

## 2.6.3  Results

### 2.6.3.1  Primary Objective Function

A summary of the progression of the optimization procedure for the primary objective function, i.e., Eq. (2.6.15), is shown in Fig. 2.6.4.  The best design at each step is shown by a filled diamond marker. The approach profiles described by $\boldsymbol{X}_1$–$\boldsymbol{X}_9$ comprise the initial sensitivity study that served to explore the design space before initiating any formal optimization steps (i.e., step zero).  Notice that, although these approach profiles spanned the design space, the objective function values for the initial

sensitivity study were remarkably similar (ranging from 0.3606–0.4516). The best design from the initial inventory was:

$$X_4 = [v_0 \ r_{pd} \ \gamma \ \psi]^T = [100 \text{ ft/sec} \quad 300 \text{ ft} \quad 8 \text{ deg} \quad 0 \text{ deg}]^T$$
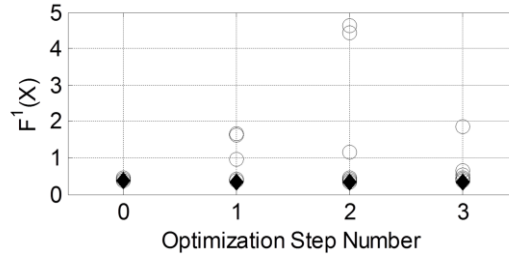


a) All function evaluations
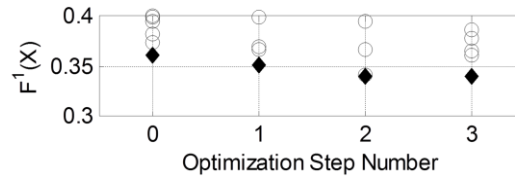


b) Best function evaluations

Figure 2.6.4. Optimization history; that is, objective, function values vs. step number, for $F_{app}^1(X_{temp})$.

The first optimization step included runs $X_{10}$–$X_{21}$, where $X_{10}$ was the optimum of the approximation to the primary objective function, $F_{app}^1(X_1$–$X_9)$, $X_{11}$ was the optimum of the approximation to the secondary objective function, $F_{app}^2(X_1$–$X_9)$ (which may be treated as an additional design for the primary optimization), and $X_{12}$–$X_{21}$ were computed using the additional design objective function, Eq. (26). The best design evaluated at this step was an additional design; that is,

$$X_{17} = [v_0 \ r_{pd} \ \gamma \ \psi]^T = [100.0052 \text{ ft/sec} \quad 190.0000 \text{ ft} \quad 1.0015 \text{ deg} \quad 44.9907 \text{ deg}]^T$$

The second optimization step included runs $X_{22}$–$X_{33}$, where $X_{22}$ was the optimum of the approximation to the primary objective function, $F_{app}^1(X_1$–$X_{21})$, $X_{23}$ was the optimum of the approximation to the secondary objective function, $F_{app}^2(X_1$–$X_{21})$, and $X_{24}$–$X_{33}$ were computed using the additional design objective function. The best design evaluated at this step was also an additional design; that is,

$$X_{24} = [v_0 \ r_{pd} \ \gamma \ \psi]^T = [100.8626 \text{ ft/sec} \quad 190.8920 \text{ ft} \quad 14.9616 \text{ deg} \quad 44.8624 \text{ deg}]^T$$

The third optimization step included runs $X_{34}$–$X_{45}$, where $X_{34}$ was the optimum of the approximation to the primary objective function, $F_{app}^1(X_1$–$X_{33})$, $X_{35}$ was the optimum of the approximation to the secondary objective function, $F_{app}^2(X_1$–$X_{33})$, and $X_{36}$–$X_{45}$ were computed using the additional design objective function. The best design evaluated at this step was also an additional design; that is,

$$\boldsymbol{X}_{42} = [v_0\ r_{pd}\ \gamma\ \psi]^T = [113.4527\ \text{ft/sec}\quad 191.1298\ \text{ft}\quad 13.3628\ \text{deg}\quad -6.8391\ \text{deg}]^T$$

Notice in Fig. 2.6.4-b that the objective function values for the best design at each step are very close; therefore, the optimization was terminated. In fact, the objective function values for the best designs from the second and third optimization steps are equal, i.e., $F^1(\boldsymbol{X}_{24}) = F^1(\boldsymbol{X}_{42}) = 0.3402$, despite the fact that these designs are not particularly similar. This observation does not imply that the objective function is uniform across the approach profile design space. The approximation to the primary objective function that was constructed from all 45 approach profile designs is shown in Fig. 2.6.5. Notice that, although the objective function appears to be quite sensitive to $\boldsymbol{X}_{\text{temp}}$ (i.e., it exhibits drastic variations in a given subfigure in Fig. 2.6.5), it is somewhat insensitive to $\boldsymbol{X}_{\text{spatial}}$ (i.e., it exhibits only subtle variations between subfigures in Fig. 2.6.5).



a) $\gamma=1°$, $\psi=-45°$      b) $\gamma=1°$, $\psi=0°$      c) $\gamma=1°$, $\psi=45°$

d) $\gamma=8°$, $\psi=-45°$      e) $\gamma=8°$, $\psi=0°$      f) $\gamma=8°$, $\psi=45°$

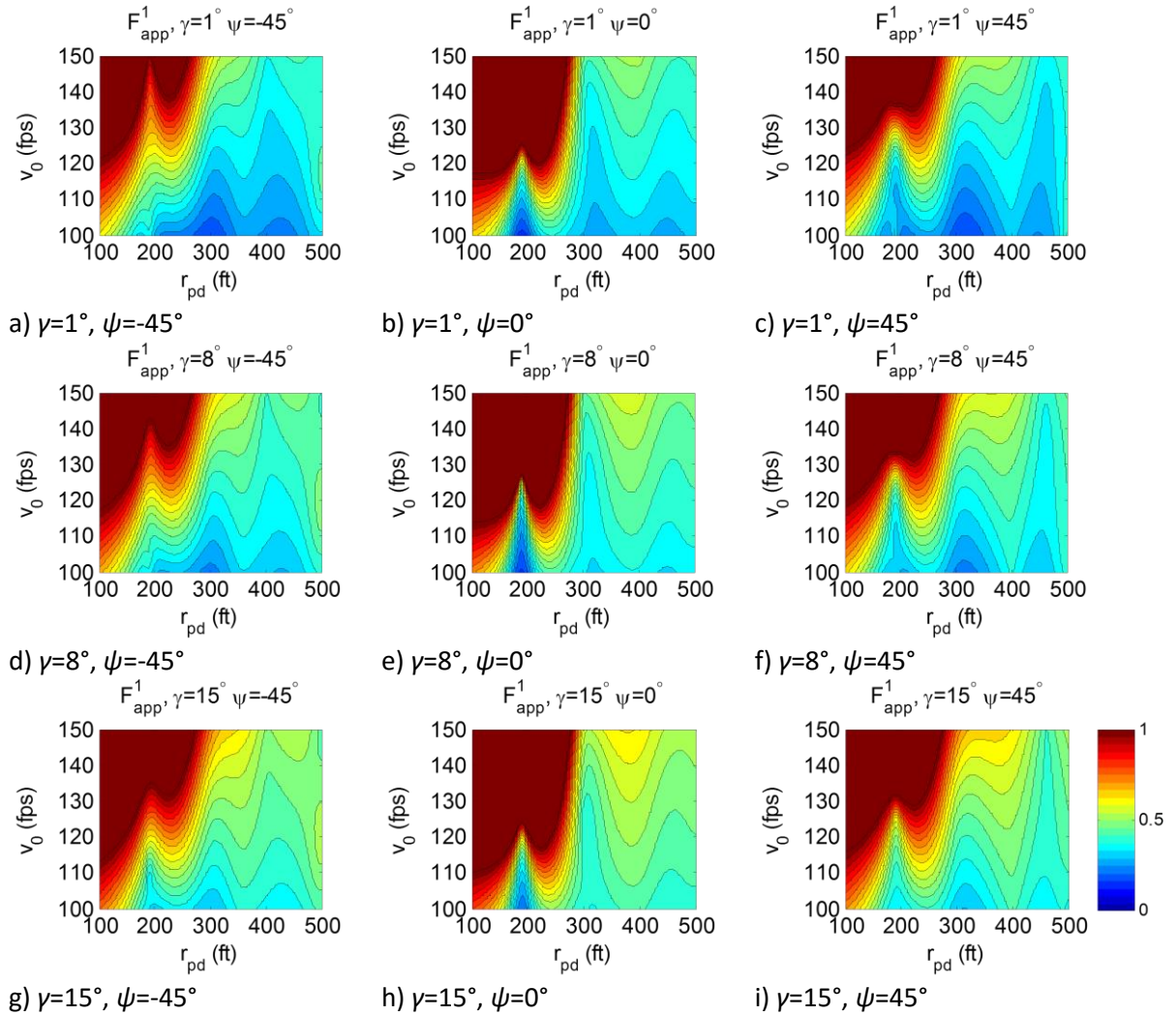g) $\gamma=15°$, $\psi=-45°$      h) $\gamma=15°$, $\psi=0°$      i) $\gamma=15°$, $\psi=45°$

Figure 2.6.5. Contour maps for $F^1_{\text{app}}(X_{\text{temp}})$ over a range of values for $X_{\text{spatial}}$.

### 2.6.3.2 Secondary Objective Function

A summary of the progression of the optimization procedure for the secondary objective function, i.e., Eq. (19), is shown in Fig. 2.6.6. Once again, the approach profiles described by $X_1$–$X_9$ comprise the initial sensitivity study that served to explore the design space before initiating any formal optimization steps. As seen with the primary objective function, the objective function values for the initial sensitivity study were similar (ranging from 0.3032–0.6868) despite the fact that the approach profiles spanned the design space. The best design from the initial inventory was:

$$X_4 = [v_0 \ r_{pd} \ \gamma \ \psi]^T = [100 \text{ ft/sec} \quad 300 \text{ ft} \quad 8 \text{ deg} \quad 0 \text{ deg}]^T$$



a) All function evaluations



b) Best function
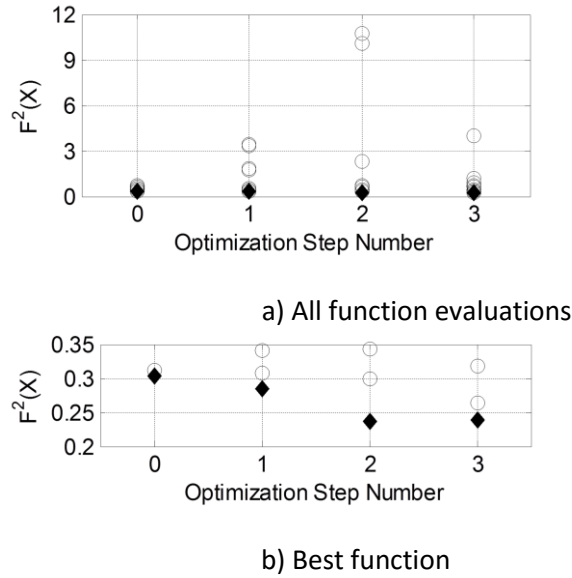
Figure 2.6.6. Optimization history; that is, objective, function values vs. step number, for

$$F^2_{\text{app}}(X_{\text{temp}}).$$

Each step of the optimization included the same runs described previously for the primary objective function, though, in this case, the optimal designs from the primary optimization were treated as additional designs for the secondary optimization. The best design evaluated in the first step was an additional design; that is,

$$X_{10} = [v_0 \ r_{pd} \ \gamma \ \psi]^T = [100.0003 \text{ ft/sec} \quad 328.2820 \text{ ft} \quad 11.4993 \text{ deg} \quad -8.1010 \text{ deg}]^T$$

The best design evaluated in the second step was also an additional design; that is,

$$X_{27} = [v_0 \ r_{pd} \ \gamma \ \psi]^T = [101.6728 \text{ ft/sec} \quad 499.3203 \text{ ft} \quad 14.9511 \text{ deg} \quad 44.8768 \text{ deg}]^T$$

The best design evaluated in the third step was found at the optimum of the approximation to the secondary objective function; that is,

$$\boldsymbol{X}_{35} = [v_0 \ r_{pd} \ \gamma \ \psi]^{\mathrm{T}} = [100.0001 \ \text{ft/sec} \quad 498.9066 \ \text{ft} \quad 14.8464 \ \text{deg} \quad 44.9997 \ \text{deg}]^{\mathrm{T}}$$

The approach profile designs for $\boldsymbol{X}_{27}$ and $\boldsymbol{X}_{35}$—and their objective function values (see Fig. 2.6.6-b)—were very close; therefore, the optimization was terminated.

The approximation to the secondary objective function that was constructed from all 45 approach profile designs is shown in Fig. 2.6.7. As with the primary objective function, the secondary objective function appears to be quite sensitive to $\boldsymbol{X}_{\text{temp}}$ (i.e., it exhibits drastic variations in a given subfigure in Fig. 2.6.7) although it is somewhat insensitive to $\boldsymbol{X}_{\text{spatial}}$ (i.e., it exhibits only subtle variations between subfigures in Fig. 2.6.7).
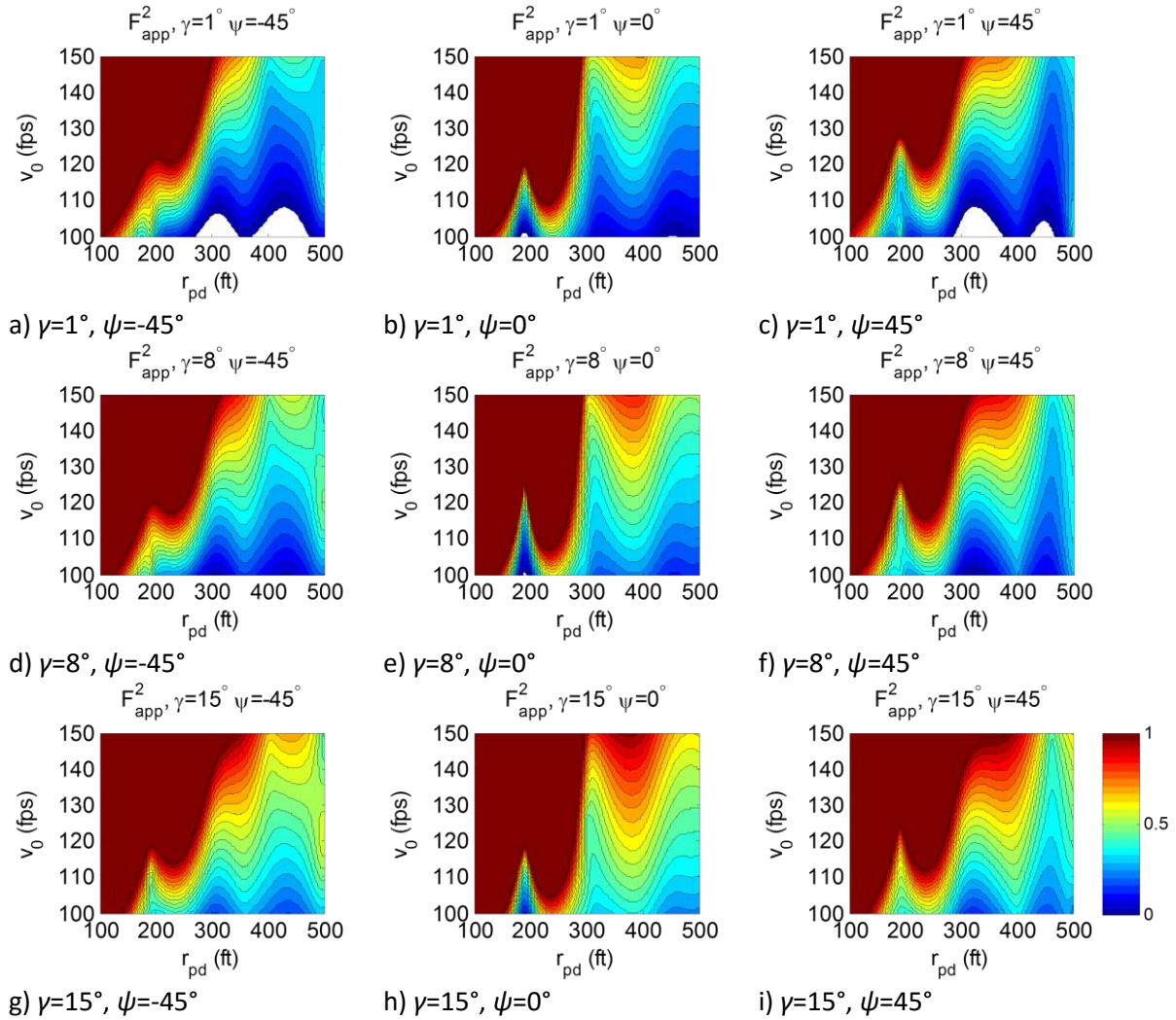


Figure 2.6.7. Contour maps for $F_{\text{app}}^2(X_{\text{temp}})$ over a range of values for $X_{\text{spatial}}$.

### 2.6.3.3  Discussion

To gain a better understanding of the optimization results, the individual performance metrics were also evaluated separately.  To make these assessments, RBF-based approximations to the various performance factors were computed.  Figure 2.6.8 shows RBF-based approximations for: 1) $k_1(\boldsymbol{X})$, i.e., normalized work, 2) $k_2(\boldsymbol{X})$, i.e., normalized mean path error, and 3) $k_3(\boldsymbol{X})$, i.e., the maximum thrust fluctuations caused by ship airwake for the baseline $\boldsymbol{X}_{\mathrm{spatial}} = [\gamma \ \psi]^{\mathrm{T}} = [8 \ \mathrm{deg} \quad 0 \ \mathrm{deg}]^{\mathrm{T}}$.



a) $k_{1,\mathrm{app}}(X_{\mathrm{temp}})$, i.e.,
normalized work

b) $k_{2,\mathrm{app}}(X_{\mathrm{temp}})$, i.e.,
normalized mean path error

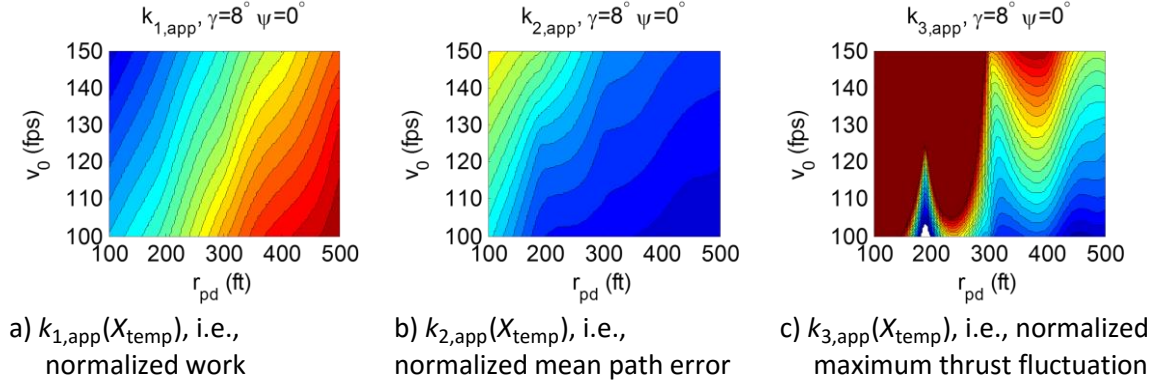c) $k_{3,\mathrm{app}}(X_{\mathrm{temp}})$, i.e., normalized
maximum thrust fluctuation

Figure 2.6.8. Contour Maps of the Various Performance Factors over a Range of Values

for $\boldsymbol{X}_{\mathrm{spatial}} = [\gamma \ \psi]^{\mathrm{T}} = [8 \ \mathrm{deg} \quad 0 \ \mathrm{deg}]^{\mathrm{T}}$

The results in Fig. 2.6.8-a clearly show that the work is minimized for more aggressive approach profiles, i.e., approach profiles with increased $v_0$ and reduced $r_{pd}$.  The results for mean path error (Fig. 2.6.8-b) show a similar sensitivity to the aggressiveness of the approach profile; however, performance is improved for less aggressive approach profiles for the case of mean path error.  Both the $k_1(\boldsymbol{X})$ and $k_2(\boldsymbol{X})$ performance factors were generally insensitive to $\boldsymbol{X}_{\mathrm{spatial}}$.  Notice that the maximum thrust fluctuation performance factor (Fig. 2.6.8-c) is highly nonlinear and nonconvex over $\boldsymbol{X}_{\mathrm{temp}}$.  While this performance factor exhibited some sensitivity to $\boldsymbol{X}_{\mathrm{spatial}}$, the results suggested that, for the present study, the airwake effects are similar for all oblique approaches (i.e., regardless of whether the approach profile is from the port or starboard side of the ship).  This result is likely attributable to the simplified SFS2 hull shape and 0° relative winds.

A qualitative comparison of the performance factors, i.e., Fig. 2.6.8, and the two objective functions, i.e., Figs. 2.6.5 and 2.6.7, reveals that the thrust fluctuations caused by the turbulent ship airwake were the primary driver of the nonlinearity and nonconvexity of both objective functions.  While this is to be expected for the secondary optimization, in which the weighting factors emphasized the $k_3(\boldsymbol{X})$ performance factor, it was not necessarily expected for the primary optimization.  For the case of the primary optimization, in which the weighting factors were equal between the three performance metrics, the normalization factors drove the increased impact of $k_3(\boldsymbol{X})$.  Although the normalization factors were selected as representative values determined from the preliminary sensitivity study, the high nonlinearity of $k_3(\boldsymbol{X})$ resulted in much greater values observed during the course of function evaluations for the optimization procedures.  This may potentially be adjusted in future studies by

changing the normalization factors between optimization steps or by setting a "ceiling" value to a given performance factor, above which the factor does not result in greater penalty; for example,

$$k_3 = \begin{cases} \dfrac{\max(\Delta T(t))}{2000 \text{ lbs}} & \text{for } \max(\Delta T(t)) \le 2000 \text{ lbs} \\ 1 & \text{for } \max(\Delta T(t)) > 2000 \text{ lbs} \end{cases} \qquad (2.6.23)$$

### 2.6.4  Conclusions

From this analysis, the following conclusions have been drawn:

First, results from the present study indicate that it is possible to generate objective functions that include multiple performance factors, and that the relative weighting of performance factors may be tailored in accordance with operational considerations.  The weighting factors and normalization factors must be carefully selected to maintain a suitable balance between multiple performance factors that may oppose each other.  In the present study, the thrust fluctuations caused by the turbulent ship airwake were the primary driver of the objective function characteristics.  This relationship was a result of the relative weighting between performance factors and the normalization factors that were applied to each performance factor.

Second, results indicate that the mathematical properties of the resulting optimization problem are likely to be dependent on the specific performance factors included in the objective function as well as their relative weights.  This dependency may have implications on the tractability of trajectory optimization studies with certain objective function formulations.  In the present study, both objective functions were highly nonlinear and nonconvex.  Although the optimization method produced improvements in the objective functions and was terminated because successive steps resulted in no appreciable improvement, the mathematical properties of the objective functions may have proven problematic if more stringent termination criteria were applied.

Last, the segmentation between the temporal and spatial variables within the proposed approach profile design vector appears to be particularly effective for comparing sensitivities of performance parameters to $X_{\text{spatial}}$, the path through space that the helicopter will follow, and $X_{\text{temp}}$, the way in which the aircraft will traverse that path.  In the present study, the objective functions were highly sensitive to $X_{\text{temp}}$ and less sensitive to $X_{\text{spatial}}$.  In particular, the results generally showed little sensitivity to the ship-relative azimuth angle, $\psi$.  This may be attributable to the use of a simplified ship structure (the SFS2) and 0° relative winds.  As such, a useful extension to the present work may be to perform additional optimization studies for alternate wind-over-deck conditions or to include relative wind magnitude and azimuth as design variables in the optimization, i.e., $X_{\text{ship}} = [v_{0,\text{ship}} \ \psi_{\text{winds}}]^{\text{T}}$.

## 2.7   Task 7 Documentation

Year 1 efforts focused on development of the plant models, implementation of the core control laws, and initial path optimization studies.  Efforts were reported in quarterly reports and published in an AIAA Conference paper:

Tritschler, J.K., Horn, J.F., and He, C., "Objective Function Development for Optimized Path Guidance for Rotorcraft Shipboard Recovery," AIAA Atmospheric Flight Mechanics Conference, Dallas, TX, June 2015.

## 2.8 Task 8 Station-keeping and landing control laws

Early in the effort it became clear that the landing phase was to be the most challenging portion of the control design. The station-keeping (Section 2.8 Task 8) and vertical descent (Section 2.9 Task 9) were deemed to be a coupled problem, and thus much of the development for landing control laws will be presented in this section (2.8), while section 2.9 is devoted to a few issues directly related to the vertical axis. Due to the challenge of landing on a moving ship deck in high sea states, a multi-pronged effort was used to study various novel methods for planning the final descent trajectory, including control algorithms that make use of forecasted deck motion.

### 2.8.1 Station keeping control law

Once the helicopter reaches a hover over the ship flight deck within tolerances, it enters a station keeping mode. In the mode, the helicopter tracks the x, y location representing the center of the flight deck and it holds a constant relative height over the deck. Since the position control law operates on commanded x, y position, the exact same control law is used in final station-keeping as on the approach, thus avoids transients associated with switching of control mode.

### 2.8.2 Landing Control Law

The objective of the landing phase is to bring the helicopter from a stable hover over the flight deck to touchdown on the flight deck, with all three landing gear contacting the deck at acceptable relative velocities. The purpose of this research is to develop methods that allow landing in high sea state conditions. Thus, for the purpose of simulation evaluation, the landing control does not attempt to wait for a quiescent period in the ship motion. Three approaches were investigated for the autonomous landing task as described below.

#### 2.8.2.1 Landing with Deck Tracking

The 1$^{st}$ method is tracking the measured horizontal deck motion while closing the gap of relative vertical position at a constant rate. This is considered the baseline case, and does not use the deck motion prediction algorithms. In this case, the commanded (x, y) positions and velocities are simply equivalent to the measured position and velocities of the flight deck. The vertical axis controller uses the measured altitude and vertical velocity of the flight deck with a constant descent bias of 1.5 ft/sec. The commanded altitude is obtained by the integration of commanded velocity (2.8.1).

$$V_{Zcmd} = V_{Zdeck} - V_{descent}$$

$$H_{cmd} = H_{hov} + H_{deck} + \int V_{Zcmd} dt \qquad (2.8.1)$$

The landing control law with deck tracking was tested in non-linear simulations, the simulation starts at a stationary hover 20 ft over the flight deck, and then initialized a descent after 10 seconds. The simulation is completed when all three landing gear are in contact with the deck. Fig shows a sample

trajectory, the red vertical lines indicate time of deck contact (first the tail gear, followed by the left and right gear shortly afterwards). Results proved the conception of landing strategy with tracking, despite the large amount of maneuvers.
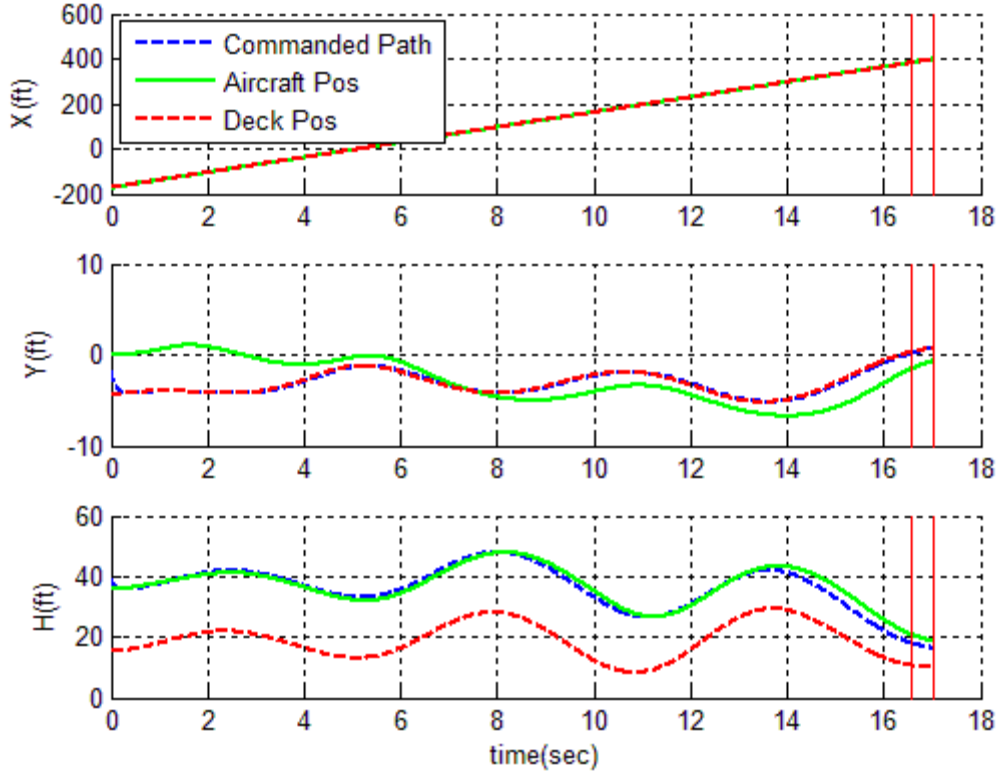


Figure2.8.1 Landing with deck tracking

### 2.8.2.2   Landing with Deck Motion Prediction and Optimal Guidance Law

This algorithm used optimal control theory to plan a descent path to the center of the landing deck such that the final vertical and lateral velocities match that of the deck at the expected touchdown time. The same outer-loop guidance control laws are used, but the commanded lateral and vertical positions and velocities are generated by the optimal control theory. The longitudinal position and velocity still track the current deck position as in the previous method.

The optimal control scheme is based on the simple dynamics of a 1 DOF inertial system:

$$\dot{y} = v$$
$$\dot{v} = a(t)$$

(2.8.2)

This is a second order system with states y and v (position and velocity), and the control input a (acceleration). Note that the DI method effectively decouples the four control axes, and the outer loop is well suited to follow acceleration commands. Thus Eq. (2.8.2) is a reasonable model for the lateral, longitudinal and vertical guidance. A control law for a(t) is sought to take the helicopter from current

state $y(t_0)$ and $v(t_0)$ to a terminal state at a fixed time horizon $y(t_f)$ and $v(t_f)$. The time $t_f$ is the prediction horizon of the deck motion forecasting algorithm and the time to land. The terminal states are set to match the predicted deck state at the landing time. During the landing maneuver, the perdition horizon is shortened and the predicted deck state updated. The control law is derived from the classical optimal control problem that minimizes the following objective function

$$ J = \frac{1}{2}c_1 \left[ v(t_f) - v_d \right]^2 + \frac{1}{2}c_2 \left[ y(t_f) - y_d \right]^2 + \frac{1}{2}\int_t^{t_f} a^2 dt $$

Where $v_d$ and $y_d$ are set to match the forecasted deck state at touch down. Thus the objective function minimizes a weighted function of terminal error and integrated control effort. In the case of vertical velocity, we add a negative bias to the terminal velocity of -1.5 ft/sec, to ensure that the helicopter descends down to wheel contact rather than hover just over the deck.

The resulting control law is of the form:

$$ a(t) = -\Lambda_v(t)\left[v(t)\text{-}v_d\right] - \Lambda_v(t)\left[y(t)\text{-}y_d\right] $$

Where $\Lambda_v$ and $\Lambda_y$ are time-varying gains defined in Ref [5]. The velocity and position weighting factors selected were, $c_1 = c_2 = 5$. This control law yields a commanded acceleration for both the lateral and vertical axes. The acceleration is integrated twice to yield commanded velocity and positions that are fed to the outer loop guidance law. In order to avoid infeasible landing trajectories, the landing profile (in terms of accelerations, velocities and positions) is calculated before initiating the landing sequence. The commanded accelerations and velocities must be within the following tolerances before initiating the landing:

$$ \left| a_y(t) \right| \leq 0.2g \; , \; \left| a_z(t) \right| \leq 0.3g $$

$$ \left| v_y(t) \right| \leq 4 \text{ ft/sec, } \left| v_z(t) \right| \leq 6 \text{ ft/sec} $$

In addition, the altitude profile is checked against forecasted deck altitude to verify that it will not make early deck contact. Once these tolerances are satisfied, the five second landing sequence is initiated. The target landing position and speed are updated every 0.096 seconds based on the latest deck forecast data from the MCA algorithm. Figure shows a sample landing trajectory that was successful. The landing sequence was initiated at 11.3 seconds into the simulation. As seen in the figure, the helicopter is commanded to hold a stable inertial hover over the landing deck until the landing maneuver begins. It then performs a more direct descent rather than follow the deck motion. The figure shows the predicted deck motion as generated by the MCA algorithm as the magenta line. The curve is shifted forward in time by the prediction horizon, which is 5 seconds for most of the simulation. At about 16.3 seconds these values "bunch up", as the forecast time is shortened throughout the descent maneuver. There is some significant error in the deck motion prediction, notably in the lateral

position. But as the forecast time decreases, the prediction becomes more accurate, as shown by the magenta prediction line moving closer to the actual deck position shown by the red line. For this case, the final x, y errors at touchdown were within the desired tolerances (0.9 ft and 1.2ft respectively). The vertical touchdown velocities of the front landing gear were slightly higher than desired (2.4ft/sec) while the lateral velocity relative to the deck was only 0.3 ft/sec.
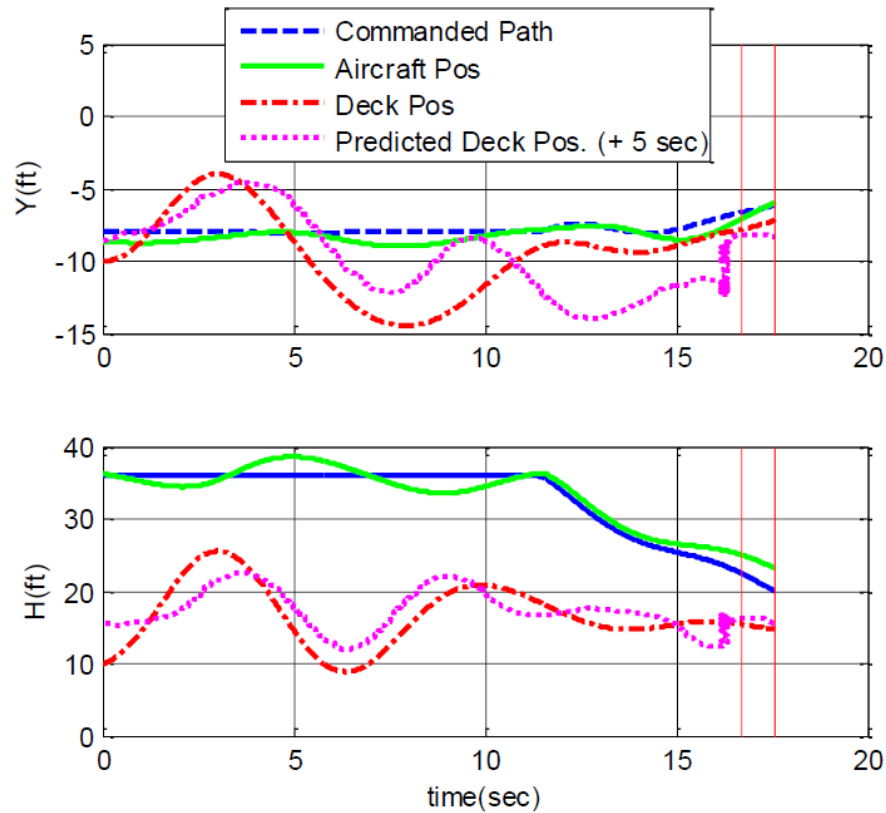


Fig.2.8.2 Landing Path Planation with multi-points deck prediction

### 2.8.2.3 *Landing with Deck Motion Prediction and Path Optimization*
The MCA algorithm was updated to accommodate forecasting of deck position at multiple points within the prediction horizon. This new feature enabled a method to plan a landing path w.r.t the predicted deck trajectory instead of using only the final point information. The method developed in this section decides the inertial landing trajectory based on full information of predicted deck motion with subject to certain constraints and optimum criteria.
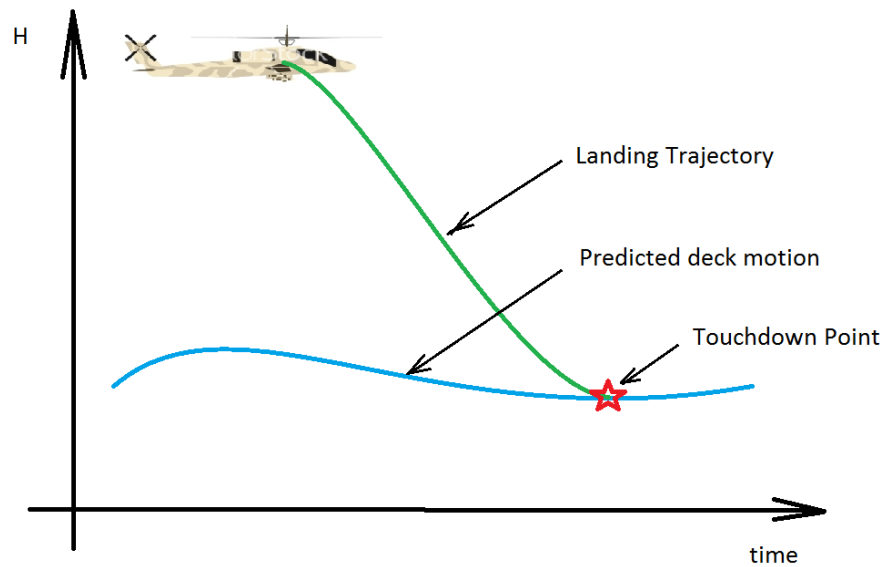
Figure 2.8.3 Scheme of Predictive Landing Path and Touchdown

Since the motions in three spatial axes are controlled individually, it's possible to generate a timed trajectory in three axes independently. Without losing generality, the vertical axis is investigated as an example.

FLIGHTLAB provides five forecasts of the deck position $X_{Ndeck}$, $Y_{Edeck}$, $H_{deck}$ spaced 1 sec apart within the horizon of 5 sec. The velocity predictions $V_{Xdeck}$, $V_{Ydeck}$, $V_{Zdeck}$ are obtained by numerical differentiation of the position prediction. The landing trajectory is parameterized by a 5$^{th}$ order polynomial $H(t) = at^5 + bt^4 + ct^3 + dt^2 + et + f$, its 1$^{st}$ and 2$^{nd}$ derivatives V(t) and A(t) define the velocity and acceleration profile respectively. Physically feasible landing paths must satisfy the following requirements

- The initial position H(0) must be the current helicopter position $H_h$
- The initial velocity V(0) must be zero, or current helicopter velocity $V_h$ whichever is smaller
- The final position is the forecasted deck position $H_{deck}$
- The final velocity is the forecasted deck velocity blended with proper relative sinking rate, e.g -1 ft/sec
- The velocity does not exceed a limit, $V_{lim}$ =6 ft/sec
- The acceleration does not exceed a limit, $A_{lim}$ =11.3 ft/sec$^2$

Quantitatively, the above condition can be reformulated as:

At t=0

$$H_h = f;$$

$$V_h = e;$$

At t=$t_f$ :

$$H_{deck}(t_f) = at_f{}^5 + bt_f{}^4 + ct_f{}^3 + dt_f{}^2 + et_f + f$$

$$V_{Zdeck}(t_f) = 5at_f^4 + 4bt_f^3 + 3ct_f^2 + 2dt_f + e$$

Having the above four equations, still need another two conditions to determine the six unknown coefficients. Note that those two additional degrees of freedom must be able to affect the internal shape of the position profile, and thus the velocity profile and acceleration profile. A feasible way is to specify H(t) at $t = \dfrac{1}{3}t_f$ and $t = \dfrac{2}{3}t_f$ . If so, the two additional equations are (2.8.3)

$$H_{13} = a(\tfrac{1}{3}t_f)^5 + b(\tfrac{1}{3}t_f)^4 + c(\tfrac{1}{3}t_f)^3 + d(\tfrac{1}{3}t_f)^2 + e(\tfrac{1}{3}t_f) + f \qquad \text{(2.8.3-a)}$$

$$H_{23} = a(\tfrac{2}{3}t_f)^5 + b(\tfrac{2}{3}t_f)^4 + c(\tfrac{2}{3}t_f)^3 + d(\tfrac{2}{3}t_f)^2 + e(\tfrac{2}{3}t_f) + f \qquad \text{(2.8.3-b)}$$

The equations for determining polynomial coefficients can be expressed in matrix form (2.8.4)

$$
\begin{bmatrix}
0 & 0 & 0 & 0 & 0 & 1 \\
0 & 0 & 0 & 0 & 1 & 0 \\
t_f^5 & t_f^4 & t_f^3 & t_f^2 & t_f & 1 \\
5t_f^4 & 4t_f^3 & 3t_f^2 & 2t_f & 1 & 0 \\
\left(\tfrac{1}{3}\right)^5 & \left(\tfrac{1}{3}\right)^4 & \left(\tfrac{1}{3}\right)^3 & \left(\tfrac{1}{3}\right)^2 & \tfrac{1}{3} & 1 \\
\left(\tfrac{2}{3}\right)^5 & \left(\tfrac{2}{3}\right)^4 & \left(\tfrac{2}{3}\right)^3 & \left(\tfrac{2}{3}\right)^2 & \tfrac{2}{3} & 1
\end{bmatrix}
\begin{bmatrix}
a \\ b \\ c \\ d \\ e \\ f
\end{bmatrix}
=
\begin{bmatrix}
H_h \\ V_h \\ H_{deck} \\ V_{deck} \\ H_{13} \\ H_{23}
\end{bmatrix}
\qquad \text{(2.8.4)}
$$

So far, $H_{13}$ and $H_{23}$ are unknown. An optimization problem is set to find out those two variables in pursuit of the minimum value of the objective function with the following constraints

- $H(t) > H_{deck}(t)$ over $t \in [0, t_f)$ to avoid early contacts
- $V_{max} < V_{lim}$
- $|A|_{max} < A_{lim}$

Those are constraints of inequality type, to apply them in the objective function, its necessary to construct a function which must be increasingly large when the constraints are not satisfied, while be ignorably small in the other case. A function with this property is exponential function.

$$obj = e^{-C(\text{Vlim}-\text{Vmax}-0.1)}$$

If $V_{\lim} - V_{\max} < 0$, the objective function increases rapidly, in the other case $V_{\lim} - V_{\max} > 0$, the objective asymptotically approaches zero. If the desired property is not strong enough, a larger value of tunable parameter C can be used.

Totally the objective function has the following form (2.8.5)

$$J = \text{w}_1 \cdot e^{-C_1 (\text{H}-\text{Hs}-0.1)_{\max}} + \text{w}_2 \cdot e^{-C_2 (\text{Vlim}-\text{Vmax}-0.1)} + \text{w}_3 \cdot e^{-C_3 (\text{Alim}-\text{Amax}-0.1)} \qquad (2.8.5)$$

Where $\text{w}_1$, $\text{w}_2$, $\text{w}_3$ are the weighting factors. An efficient gradient descent method is used to solve the optimization problem. The following example is used to demonstrate the capability of the landing path algorithm.

$t_f$ =5sec, $H_h$=45ft, $V_h$=0 ft/sec, $H_{deck}$=16 ft, $V_{deck}$=3 ft/sec

The forecasting time array is: $T_{fcast}$ = [0 1 2 3 4 5]

The forecasted deck position array is: $H_{fcast}$ = [15 20 22.12 21.95 19.46 16];

The optimized position, velocity and acceleration profiles vs. time are presented in Figure 2.8.4. it's obvious that the initial guess of landing path violates the velocity and acceleration constraint, while the optimization algorithm successfully addresses this problem and yields a feasible trajectory.
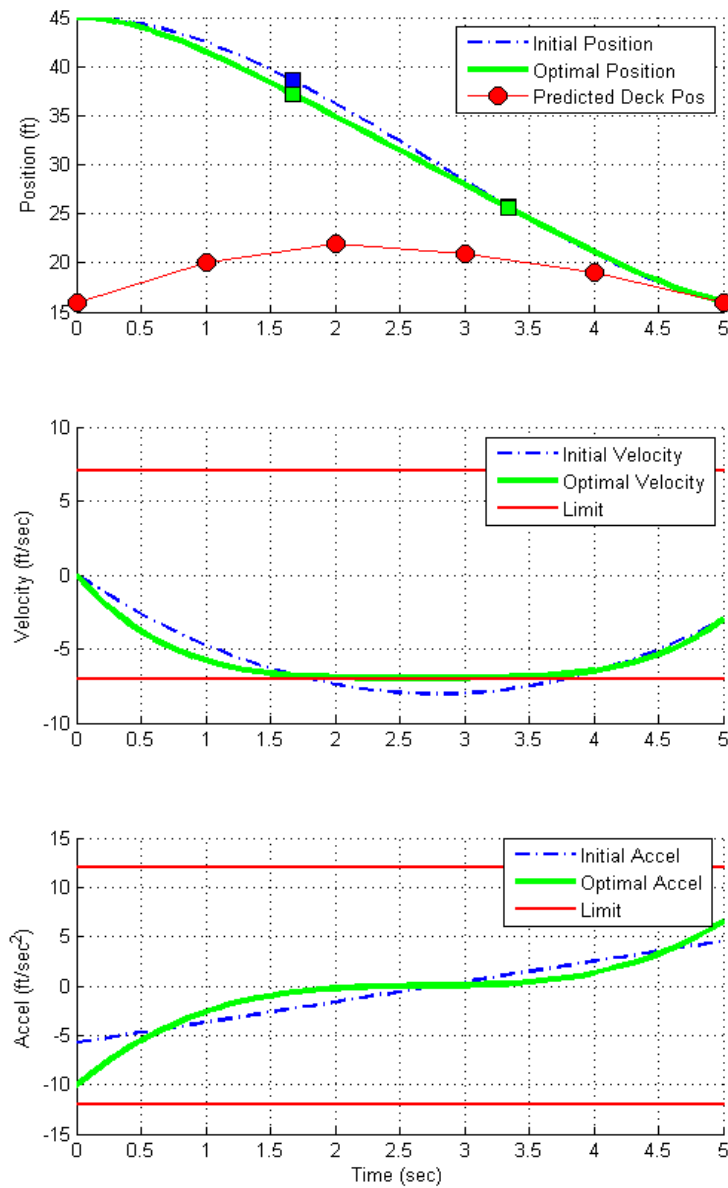
Figure 2.8.4. Planned Position, Velocity and Acceleration Profiles

Results of a landing test on medium class helicopter model with SCONE 2 data were shown in Fig 2.8.5 – 2.8.9, for this case, the final x, y errors at touchdown were 1.5 ft, 2.0 ft respectively. The vertical and lateral touchdown velocities were 3.6855 ft/sec and 0.6712 ft/sec respectively. Both position and velocity error were in acceptable tolerance.
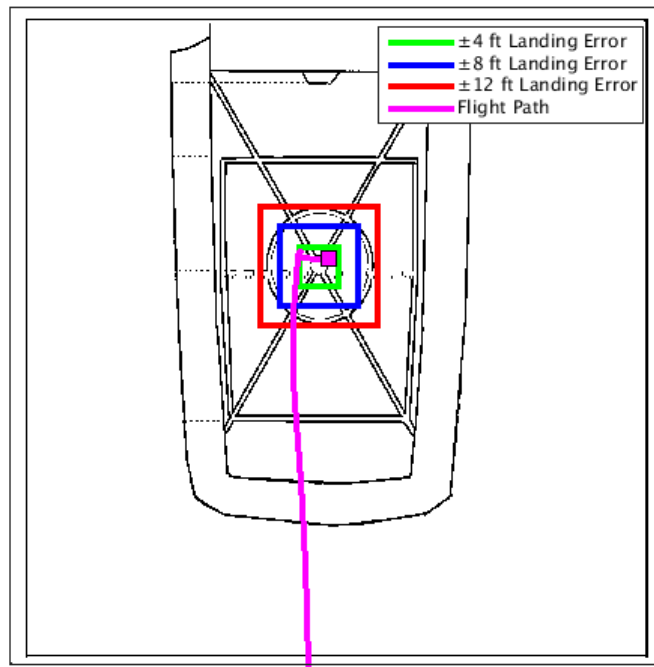
Figure 2.8.5.  Top View of Approach and Landing Path in Ship Relative Frame
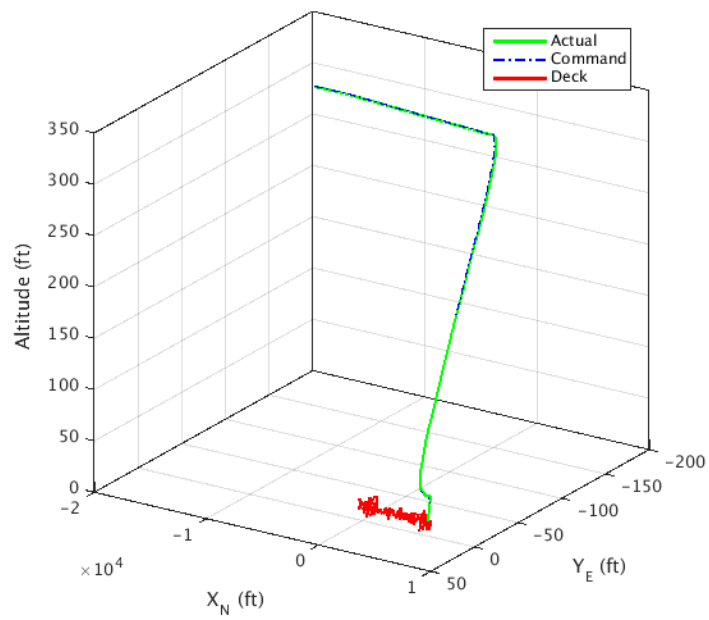


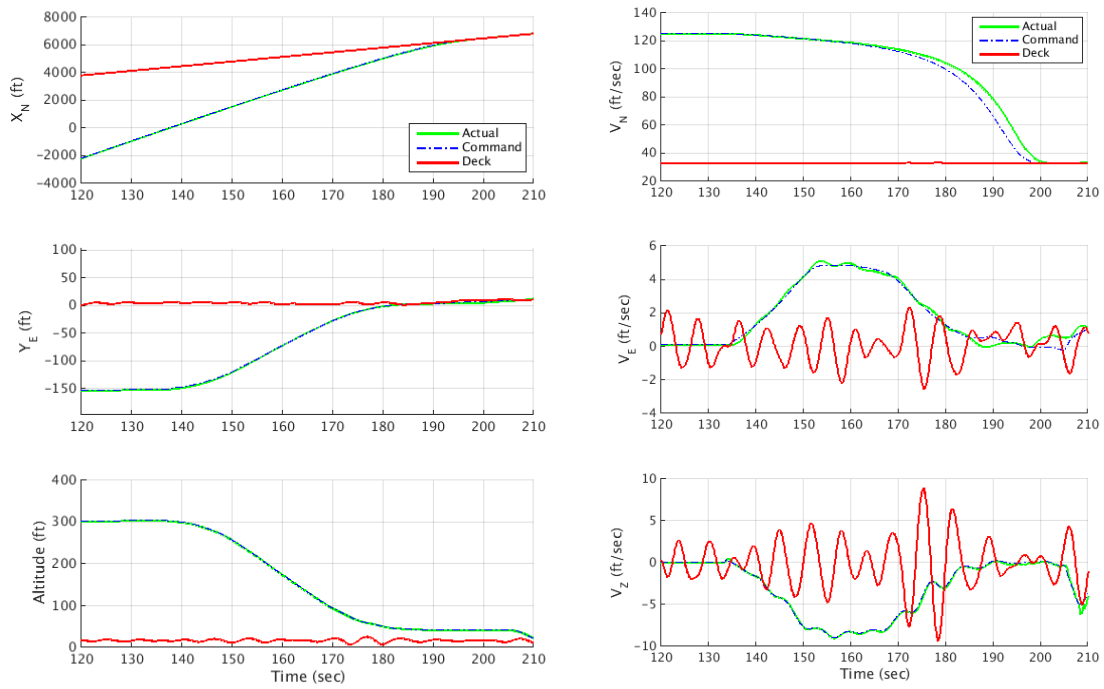Figure 2.8.6. 3D Plot of Approach and Landing Path

Figure 2.8.7. Position and Velocities Tracking History
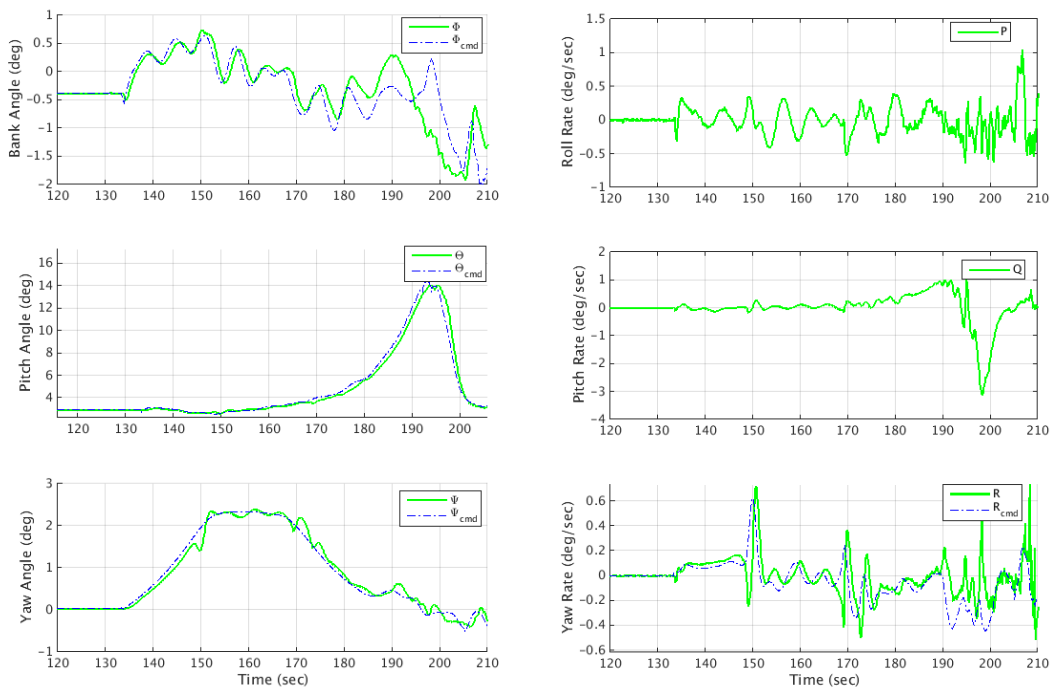


Figure. 2.8.8 Attitude Angles and Attitude Rate
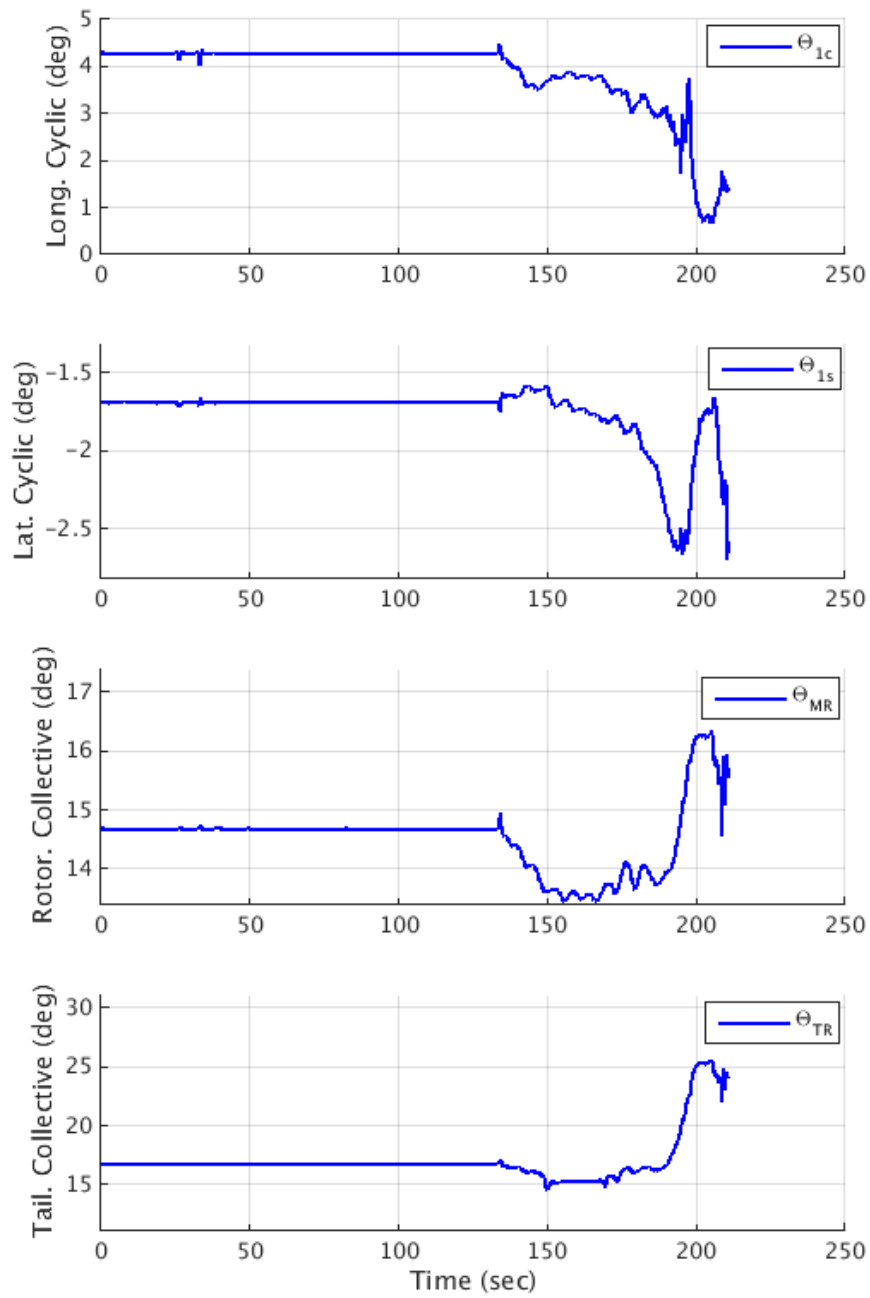
Figure 2.8.9. Control Effort

## 2.9  Task 9 Vertical axis control laws and control/power margin compensation

From section 2.4.2, the body-axis heaving velocity $w$ is in the state vector of the linear model used in the DI controller, and the inertial velocity is assumed to be equivalent but with opposite sign. In the context of vertical position control, the position can be more accurately regulated use a model that use vertical inertial velocity $V_D$ which is affected by aircraft pitch attitude.

From the Eq. (2.9.1):

$$V_D = w\cos\theta - u\sin\theta \qquad\qquad (2.9.1)$$

It's evident that $w$ is an acceptable approximation to $V_D$ at low speed, while at high forward speed the 2$^{nd}$ term starts to contribute significantly. To account for this effect, it's necessary to convert $w$ to $V_D$ in the inner loop design procedure. In the analysis below, the red terms are modifications to the original control law.

The linear model for state vector [w p q r]$^T$ :

$$\frac{d}{dt}\begin{bmatrix} w \\ p \\ q \\ r \end{bmatrix} = A\begin{bmatrix} w \\ p \\ q \\ r \end{bmatrix} + B\begin{bmatrix} \delta_{lon} \\ \delta_{lat} \\ \delta_{col} \\ \delta_{ped} \end{bmatrix}$$

Where

$$A = \begin{bmatrix} Z_w & Z_p & Z_q + U_{trim} & Z_r \\ L_w & L_p & L_q & L_r \\ M_w & M_p & M_q & M_r \\ N_w & N_p & N_q & N_r \end{bmatrix},$$

$$B = \begin{bmatrix} Z_{\delta lon} & Z_{\delta lat} & Z_{\delta col} & Z_{\delta ped} \\ L_{\delta lon} & L_{\delta lat} & L_{\delta col} & L_{\delta ped} \\ M_{\delta lon} & M_{\delta lat} & M_{\delta col} & M_{\delta ped} \\ N_{\delta lon} & N_{\delta lat} & N_{\delta col} & N_{\delta ped} \end{bmatrix}$$

In particular, the linearized equation for W is (2.9.2)

$$\dot{w} = Z_w w + Z_p p + (Z_q + u_{trim})q + Z_r r + Z_{\delta lon}\delta_{lon} + Z_{\delta lat}\delta_{lat} + Z_{\delta col}\delta_{col} + Z_{\delta ped}\delta_{ped} \quad (2.9.2)$$

To obtain the equation for VD i.e. (2.9.4), simply substitute (2.9.3) into Eq. (2.9.2)

$$V_D \approx w - u_{trim}\theta \qquad\qquad (2.9.3.a)$$

$$\dot{V}_D = \dot{w} - u_{trim}q \qquad\qquad (2.9.3.b)$$

$$\dot{V}_D = Z_w \cdot V_D + Z_p p + {\color{red}Z_q q} + Z_r r + {\color{red}Z_w u_{trim}} \cdot \theta + Z_{\delta lon} \delta_{lon} + Z_{\delta lat} \delta_{lat} + Z_{\delta col} \delta_{col} + Z_{\delta ped} \delta_{ped} \quad (2.9.4)$$

The state space model for $\begin{bmatrix} V_D & p & q & r \end{bmatrix}^T$ is in (2.9.5):

$$\frac{d}{dt}\begin{bmatrix} V_D \\ p \\ q \\ r \end{bmatrix} = A' \begin{bmatrix} V_D \\ p \\ q \\ r \end{bmatrix} + B \begin{bmatrix} \delta_{lon} \\ \delta_{lat} \\ \delta_{col} \\ \delta_{ped} \end{bmatrix} + \underbrace{\begin{bmatrix} {\color{red}Z_w u_{trim}} \\ 0 \\ 0 \\ 0 \end{bmatrix}}_{A_2} \theta \qquad (2.9.5)$$

$$\text{where } A' = \begin{bmatrix} Z_w & Z_p & {\color{red}Z_q} & Z_r \\ L_w & L_p & L_q & L_r \\ M_w & M_p & M_q & M_r \\ N_w & N_p & N_q & N_r \end{bmatrix}$$

The new stability derivative matrix $A'$ shares all the elements with $A$ matrix except 1$^{st}$ row 3$^{rd}$ column element which becomes $Z_q$. Now the inversion part of the inner loop DI controller is modified as (2.9.6):

$$\upsilon = CB^{-1}\left(\begin{bmatrix} \dot{V}_D \\ \dot{p} \\ \dot{q} \\ \dot{r} \end{bmatrix}_{cmd} - CA'\begin{bmatrix} V_D \\ p \\ q \\ r \end{bmatrix} - CA_2\theta\right) \qquad (2.9.6)$$

The derivation of this section shows that external states can be easily injected into the inversion procedure without essential change of the control structure or overall redesign. This version of the control law was ultimately implemented and shown to improve tracking on the approach.

Power margin compensation can then be implemented in this control law through simple constraints on the vertical velocity in the inertial frame. This is applied relating the vertical velocity to excess power:

$$\left(\Delta V_D\right)_{min} = \frac{\Delta P}{W}$$

Given current power required, the margin to maximum rate of climb can be related to the power margin and gross weight. The limiter can be continuously updated based on a filtered power measurement. Similarly, descent velocity limits can be established based on the autorotation limit or vortex ring state considerations. In the results presented in this report, power limits were not critical,

and thus this limiting scheme was never tested.  In the final year of the research, power limitations will be considered for higher gross weight versions of the three helicopter models.

## 2.10  Task 10 Gust rejection control laws

Gust rejection properties of a helicopter flight control system can be framed as a design trade-off between high gain designs for disturbance rejection versus lower gain design for more robust stability of the closed loop system.   This tradeoff was clearly defined in work at the US Army AeroFlightDynamics Directorate [Mansur et al 2009], where helicopter disturbance rejection was defined by the Disturbance Rejection Bandwidth property, and stability robustness measured through classical broken loop stability margins (gain and phase margin) as well as the Disturbance Rejection Peak parameter.  These parameters are proposed as new handling qualities requirements for ADS-33 [Blanken et al 2014].

The concepts of stability margins are based on the Nyquist stability criterion, where stability of a closed loop system is based on analysis of the Nyquist plot: the trajectory of GH($j\omega$) in the complex plane for all frequencies $\omega$, where GH(s) is the open loop transfer function.   Stability is determined by encirclements of -1 + 0$j$, and gain and phase margin determine by the smallest phase or gain shift that will destabilize the closed loop system.  Technically, the Nyquist criterion applies to single-input / single-output feedback systems, but in practice the stability margin method is applied to MIMO aircraft flight controls systems by breaking the feedback of a single axis at a time, then observing the frequency response from broken loop input to broken loop output.   The loop break is normally applied right before the actuator.  This is illustrated for this application in Figure X.   Stability margin analysis was performed by extracting a high order linear model of the plant dynamics (46 state model) around the nominal operating point for shipboard operation (20 knots airspeed).  The linear model was linked with a flight control system model constructed in the MATLAB / SIMULINK environment, then the entire system linearized.  The linearized closed loop system can be used to verify closed loop stability and to check that the response bandwidths correlate with the model response used in design.  The model is then linearized with loop breaks to analyze stability margins, and this process is repeated for each of the four axes.
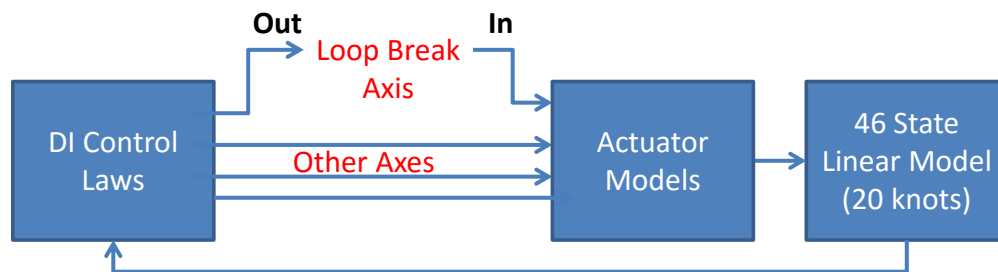


Figure 2.10.1 Schematic of Stability Margin Analysis

While stability margin analysis is more rigorously analyzed with Nyquist diagrams, it is more easily observed using Bode plots of the broken loop transfer function.  Phase Margin is seen as the difference between phase and -180° at the gain crossover frequency (where magnitude passes through 0 dB) and

gain margin as the difference between magnitude and 0 dB where phase passes through -180°. Actual interpretation can be difficult as there are sometimes multiple crossovers, however the MATLAB margin tools are able to handle this. The broken loop dynamics of the helicopter tend to be "conditionally stable systems" with at least two phase crossovers. This is logical, since the open-loop helicopter dynamics are normally unstable, so reducing gains to 0 will tend to destabilize the system. Thus there is typically both a positive gain margin indicating maximum allowable loop gain and a negative GM indicating minimum allowable loop gain. Figure 2.10.2 is a typical Bode plot for the medium class helicopter model. This diagram shows the longitudinal broken loop system. There are a few observations than can be taken from this diagram.

1. The gain crossover frequency is around 3 rad/sec, which is a frequency within the normal range of flight control compensation.
2. The magnitude dB curve is fairly linear around this frequency (form 1 to 10 rad/sec) with slope about -20 dB/decade, and the phase is hovering just below -90°. These are the properties of an integrator. This is a characteristic of the DI feedback linearization which converts the plant to integrators in each axis. This ensures desired dynamic properties when the axis loop is closed.
3. There are two phase crossings, one below and one above the gain crossover frequency, these define upper and lower bounds on loop gain. This indicates that the helicopter dynamics with the DI compensator represent a conditionally stable system.

The Disturbance Rejection Bandwidth (DRB) parameter was developed to provide a measurable metric for assessing the capability of a helicopter flight control system to hold trim in the presence of external disturbances. Like stability margins, the DRB metric is defined in the frequency domain, where one observes the closed loop frequency response from a disturbance applied to a sensor and the resulting sensor measurement. The analysis is performed on the outer most loop of the autopilot system (attitude on attitude hold systems, velocity on velocity hold systems, position on position hold systems). The resulting transfer function of sensor disturbance to sensor output is known as the Sensitivity transfer function. Since the sensor disturbance is direct feedthrough, the high frequency gain for the system is 1 (0 dB), while the low frequency gain is 0 (-∞ dB) as the "hold" function of the control system should reject the disturbance in steady-state. The frequency where the curve passes through -3 dB represents the Disturbance Rejection Bandwidth or the maximum frequency at which the controller effectively rejects disturbances. The curve will typically overshoot 0 dB, and the peak of the curve is known as Disturbance Rejection Peak (DRP). Excessive peak can indicate lack of damping in the closed loop system.
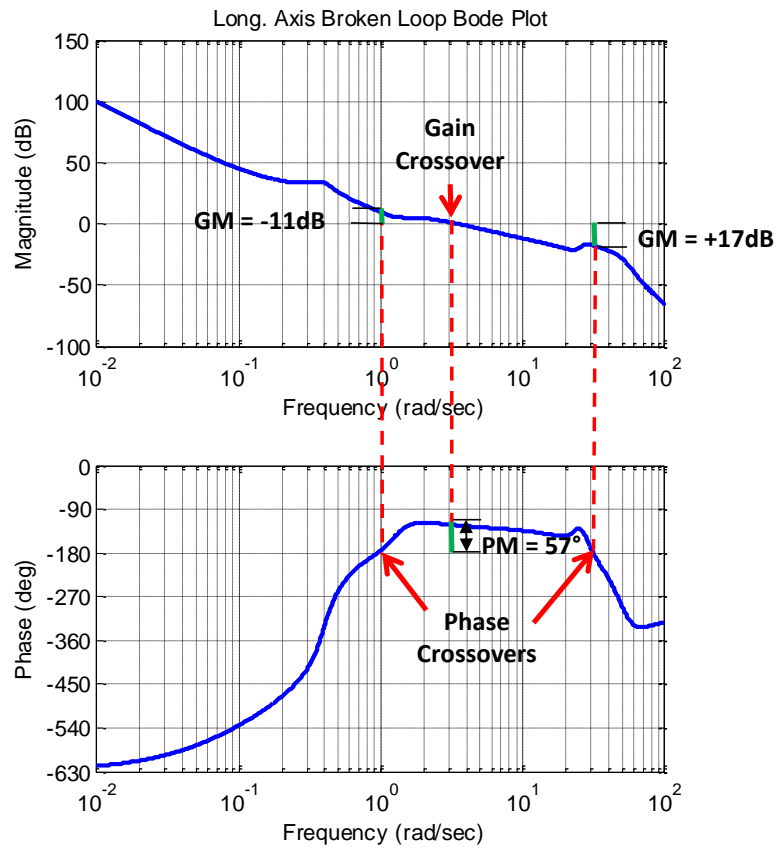
Figure 2.10.2 Stability Margin Analysis of Longitudinal Axis

A simple analysis can be used to demonstrate the effect of the DI control law gains on the DRB. Assuming a linear plant model and perfect inversion, we can analyze the output response due to a disturbance applied at the sensor as shown in the figure below. The DRB analysis considers the frequency response of $\frac{y}{y_d}(s)$.
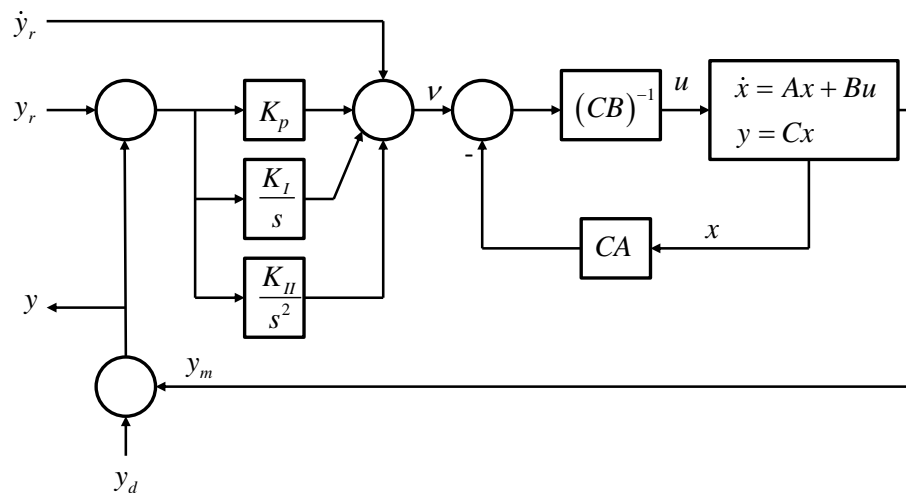


Figure 2.10.3 Basic Analysis of Dynamic Inversion Disturbance Rejection Properties

Following a similar derivation as shown in Eqs. 2.4.1 to 2.4.7., the disturbance dynamics can be derived as a 3$^{rd}$ order transfer function of sensor disturbance to sensor output:

$$\frac{y}{y_d}(s) = \frac{s^3}{s^3 + K_p s^2 + K_i s + K_{ii}} = \frac{s^3}{\left(s^2 + 2\zeta\omega_n s + \omega_n^2\right)(s+p)}$$

(2.4.6)

Thus the disturbance response follows the error dynamics specified by the gains or alternatively by the equivalent frequency, damping, and real pole parameters. In particular, the natural frequency parameter becomes a natural tuning parameter to adjust the disturbance rejection properties of the closed loop systems. Higher frequency yields higher values for all of the gains. Meanwhile, the damping ratio term can be kept constant to ensure well-damped error dynamics (typically $\zeta = 1$), and the pole, which sets the integrator action, is set to some fixed fraction of the natural frequency (typically $p = 0.2\omega_n$).

For the position hold system, the 3$^{rd}$ order error dynamics exist for both the inner loop (roll and pitch attitude) and the outer loop (lateral and longitudinal position). Thus the DRB will be affected by both sets of gains (or frequency parameters) and the inner loop command filter (since the outer loop command passes through it). Normally, it is desired that the inner loop be substantially faster (higher frequency) than the outer loop. A 1/5 frequency separation rule typically applies, i.e. the natural frequency parameter of the outer loop can be set to 1/5 of that of the inner loop.

Figure 2.10.4 shows a schematic of the analysis used for this research. A linearized SIMULINK model of the 46 state aircraft dynamics, the actuators, and the DI control laws was used to extract a model of sensor response to sensor disturbance, $\frac{y}{y_d}(s)$, with all feedback loops closed. Since the controller of interest is a fully autonomous controller design to follow a commanded trajectory, and position feedback is the outermost loop, the disturbance rejection properties of the position hold are analyzed.
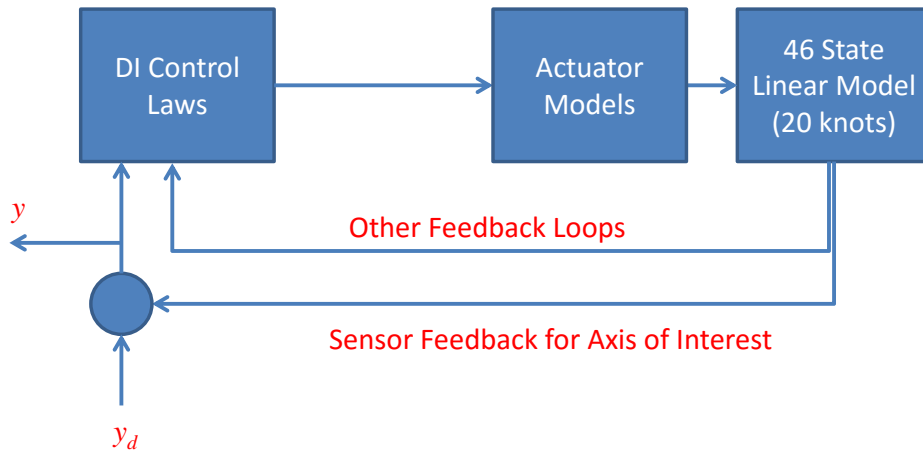


Figure 2.10.4 Schematic of Disturbance Rejection Analysis

Focusing on the longitudinal axis, details of the longitudinal position control are shown in Figure 2.10.5. For clarity the figure also includes the notional disturbance input used for longitudinal position is shown as the red dashed signal (this is notional as it is used in DRB analysis only and not part of the actual control law). Note that the trajectory commands and its first derivative are compared to position and velocity measurements. PI compensation is applied to position feedback and proportional compensation on velocity error provides derivative feedback. The 2$^{nd}$ derivative provides and acceleration command used for feedforward compensation and is summed with the compensators to yield the pseudo command. Outer loop inversion is very simple, pitch attitude commands is derived as the product of -1/g and the pseudo-command. The pitch attitude command passes through the command filter before passing on to the inner loop. Note that the lateral position control is very similar. The position hold disturbance rejection properties will be affected by numerous components of the control law: 1) The inversion, 2) The inner loop PID compensation, 3) The inner loop command filters, 4) The outer loop PID compensation. The disturbance rejection is *not* affected by the path generation elements of the control law.
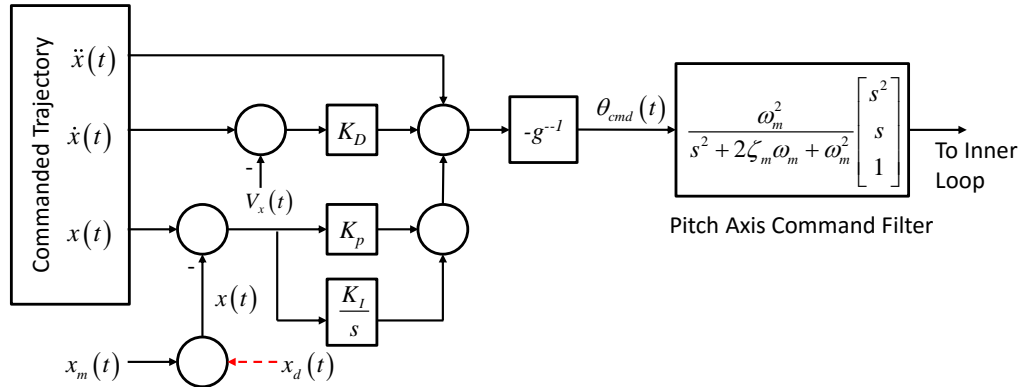


Figure 2.10.5 Details of Longitudinal Axis Position Control

Figure 2.10.6 shows a typical DRB plot for longitudinal position (X Position) hold. Note that the DRB is 0.17 rad/sec which is exactly the minimum recommended for ADS-33 design guidelines (no DRB requirements in ADS-33 have been officially defined). The peak is 3.3 dB is slightly higher than the maximum recommended peak of 3 dB. This is just for one notional set of gains and longitudinal axis command filter values.
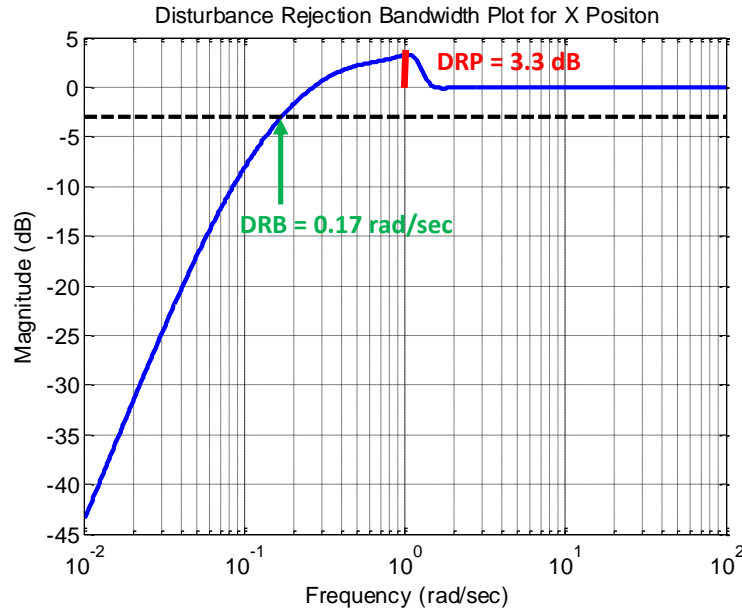
Figure 2.10.6 Typical DRB Plot for Longitudinal Position Hold

To better understand design tradeoffs and achievable performance, a more rigorous gain study was performed for the longitudinal and lateral position hold properties of the control law. The study focused on the medium class model. For both the lateral and longitudinal axes, the key frequency parameters were varied across a range while holding the parameters in other axes constant. The stability margins and DRB/DRP were then evaluated to understand the design tradeoff.

The method for varying the gains was as follows:

1. Select the inner loop natural frequency parameter for the attitude control (roll or pitch). Use this value for natural frequency of both the command filter and the error dynamics.
2. Set the damping ratio for the inner loop gain selection to $\zeta = 1.0$, and the pole to $p = 0.2\omega_n$. Then set inner loop gains based on formula in 2.4.7.
3. Set the outer loop natural frequency parameter for the position control (y or x) to be 1/5 that of the inner loop. Use this value for natural frequency of the error dynamics.
4. Set the damping ratio for the outer loop gain selection to $\zeta = 1.0$, and the pole to $p = 0.2\omega_n$. Then set inner loop gains based on formula in 2.4.7.
5. Implement in linearization diagram and extract stability margins and DRB/DRP.
6. Repeat for range of inner loop frequency from 1.5 to 4.0 rad/sec.

As the frequency parameter is increased the DRB goes up in the primary axis of interest. At the same time we find that the stability margins tend to go down and the DRP goes up, indicating less damping / stability of the closed loop system. Due to the de-coupling achieved by the DI control law, it can be observed that the stability and disturbance rejection of the other control axes are basically unaffected by the gain variations. This is one of the main advantages of the DI control architecture.

Table 2.10.1 shows the variations in the longitudinal axis, while Table 2.10.2 shows equivalent results for the lateral axis.   In [Blanken et al 2014] it is proposed that position hold achieve at least 0.17 rad/sec DRB in the X and Y position hold, while DRP ≤ 3 dB.  It can be seen that the DRB is achievable and can be exceeded.  However DRP slightly exceeds these guidelines.  It is possible that  the DRP requirement is not as significant for fully autonomous modes as long as the aircraft is stable.

The SAE guidelines recommend 45°/6 dB phase and gain margin.  The gain margin is easily achieved in all axes.  The phase margin is readily achieved in all axes except roll.  Some relaxation in the phase margin is generally accepted, especially with high levels of control augmentation.  In addition, the lateral axis is not as sensitive to increased gain as the longitudinal axes.

Figure 2.10.7 shows the stability margin Bode plot and the DRB curve for the longitudinal axis with variations in the longitudinal axis frequency parameter. We see the expected trends of increased DRB, increased DRP, and higher gain crossover (in the Bode plot) as the frequency parameter is increased. The higher gain crossover leads to lower phase margins.  Figure 2.10.8 shows the *lateral* axis Bode and DRB plots with variations in the *longitudinal axis* frequency parameter.  The point of this plot is to show that the performance and stability in the lateral axis is virtually unaffected by the longitudinal axis design parameter.  Figure 2.10.9 shows a design chart illustrating the tradeoff between SM and DRB for the longitudinal axis.  The 45° phase margin requirement and the 0.17 rad/sec DRB requirement are shown as red lines to indicate desired design constraints.

Table 2.10.1 Variations in Longitudinal Axis Gain

| Roll / Pitch Frequency Parameters | | Disturbance Rejection in Y Position | | Disturbance Rejection in X Position | | Lateral Axis Stability Margins | | Long. Axis Stability Margins | | Coll Axis Stability Margins | | Yaw Axis Stability Margins | |
|---|---|---|---|---|---|---|---|---|---|---|---|---|---|
| $\omega_{n_\phi}$ (rad/s) | $\omega_{n_\theta}$ (rad/s) | DRB (rad/s) | DRP (dB) | DRB (rad/s) | DRP (dB) | PM (deg) | GM (dB) | PM (deg) | GM (dB) | PM (deg) | GM (dB) | PM (deg) | GM (dB) |
| 2.0 | **1.5** | 0.14 | 3.5 | 0.13 | 2.9 | 38 | +26 -19 | 67 | +21 -12 | 52 | +28 -22 | 74 | +∞ -13 |
| 2.0 | **2.0** | 0.14 | 3.5 | 0.17 | 3.3 | 38 | +33 -19 | 57 | +17 -11 | 52 | +29 -22 | 74 | +∞ -14 |
| 2.0 | **2.5** | 0.14 | 3.5 | 0.21 | 3.9 | 38 | +32 -19 | 50 | +15 -9.4 | 51 | +29 -22 | 74 | +∞ -17 |
| 2.0 | **3.0** | 0.14 | 3.5 | 0.25 | 4.4 | 38 | +31 -19 | 45 | +13 -8.6 | 51 | +30 -22 | 74 | +∞ -18 |
| 2.0 | **3.5** | 0.14 | 3.4 | 0.29 | 4.7 | 36 | +29 -19 | 40 | +11 -8.6 | 51 | +30 -22 | 74 | +∞ -18 |
| 2.0 | **4.0** | 0.14 | 3.4 | 0.33 | 4.7 | 34 | +28 -18 | 37 | +9 -9 | 51 | +31 -22 | 74 | +∞ -18 |

Table 2.10.2 Variations in Lateral Axis Gain

| Roll / Pitch Frequency Parameters | | Disturbance Rejection in Y Position | | Disturbance Rejection in X Position | | Lateral Axis Stability Margins | | Long. Axis Stability Margins | | Coll Axis Stability Margins | | Yaw Axis Stability Margins | |
|---|---|---|---|---|---|---|---|---|---|---|---|---|---|
| $\omega_{n_\phi}$ (rad/s) | $\omega_{n_\theta}$ (rad/s) | DRB (rad/s) | DRP (dB) | DRB (rad/s) | DRP (dB) | PM (deg) | GM (dB) | PM (deg) | GM (dB) | PM (deg) | GM (dB) | PM (deg) | GM (dB) |
| 1.5 | 2.0 | 0.11 | 3.3 | 0.17 | 3.3 | 36 | +8.9 -31 | 57 | +18 -11 | 52 | +29 -22 | 74 | +∞ -13 |
| 2.0 | 2.0 | 0.14 | 3.5 | 0.17 | 3.3 | 38 | +33 -19 | 57 | +17 -11 | 52 | +29 -22 | 74 | +∞ -14 |
| 2.5 | 2.0 | 0.17 | 3.7 | 0.17 | 3.3 | 38 | +24 -20 | 57 | +17 -11 | 52 | +29 -22 | 74 | +∞ -14 |
| 3.0 | 2.0 | 0.20 | 4.0 | 0.17 | 3.3 | 36 | +20 -20 | 57 | +17 -11 | 52 | +29 -22 | 74 | +∞ -14 |
| 3.5 | 2.0 | 0.23 | 4.3 | 0.17 | 3.3 | 32 | +17 -19 | 57 | +17 -11 | 52 | +29 -22 | 76 | +∞ -13 |
| 4.0 | 2.0 | 0.26 | 4.6 | 0.17 | 3.3 | 27 | +14 -20 | 57 | +17 -11 | 52 | +29 -22 | 78 | +∞ -13 |
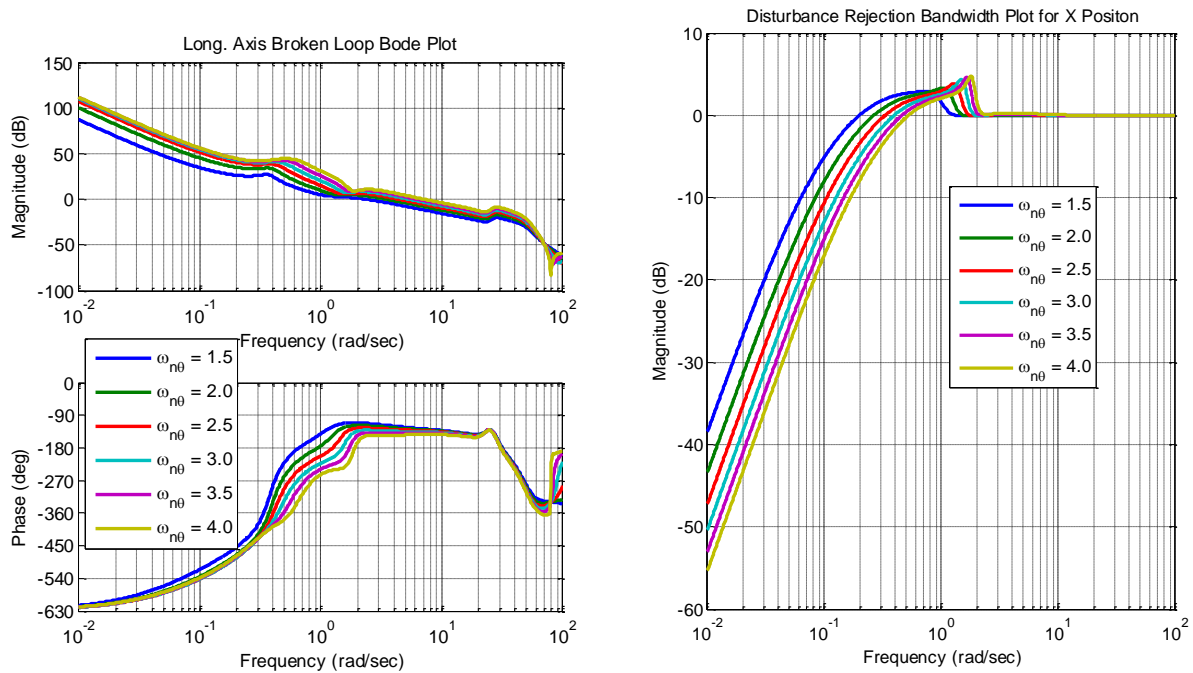


Figure 2.10.7 Longitudinal Axis Bode and DRB Plots with Variations in Longitudinal Axis Gain
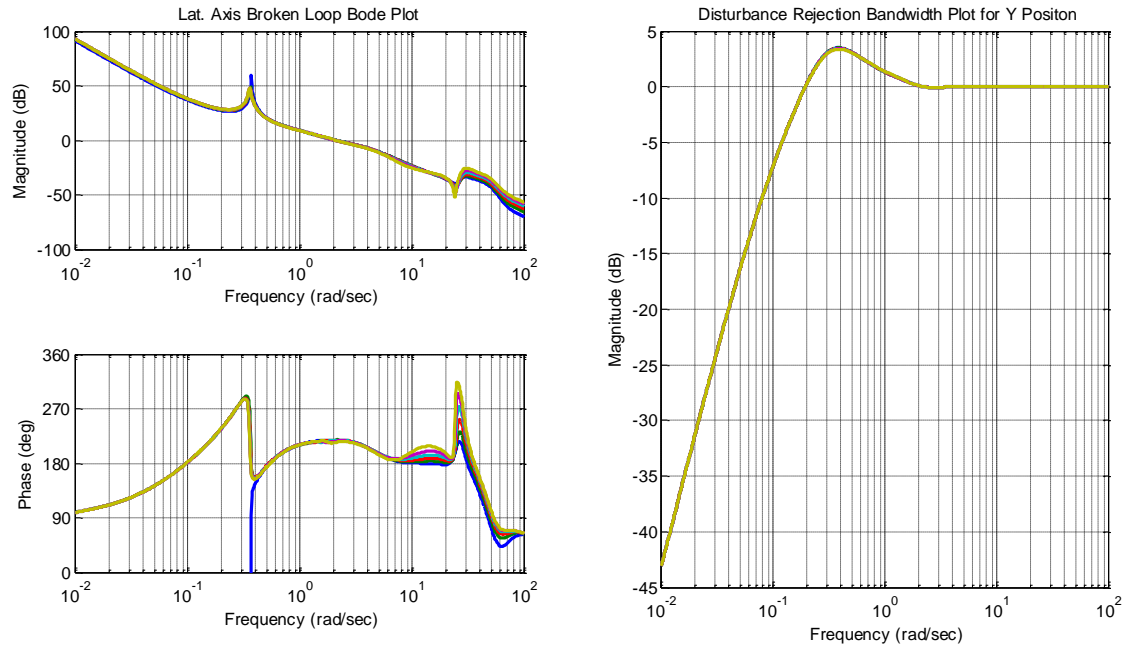(Margins and Disturbance Rejection are Driven by Longitudinal Gains)

Figure 2.10.8 Lateral Axis Bode and DRB Plots with Variations in Longitudinal Axis Gain
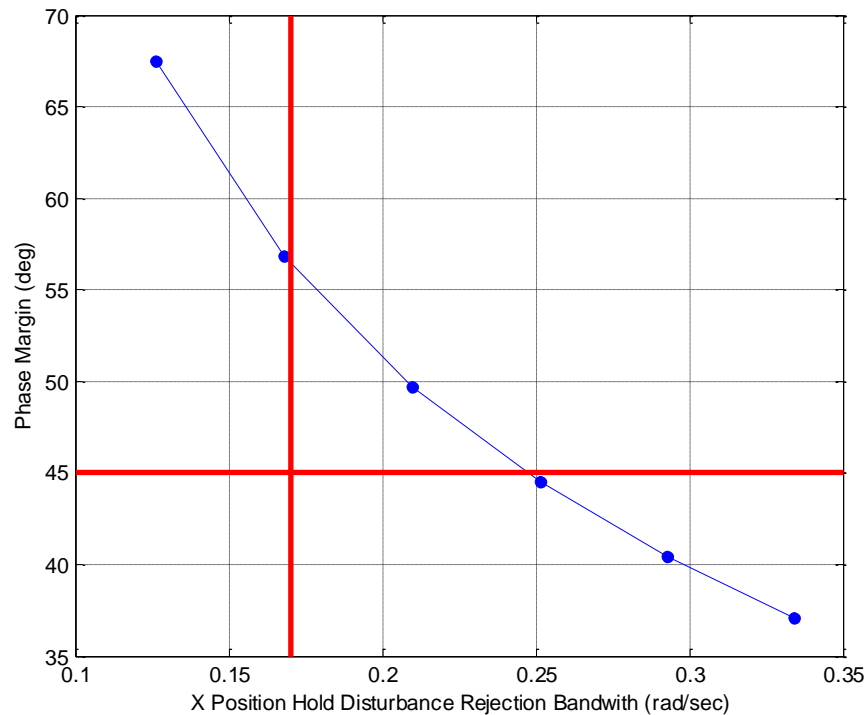(Margins and Disturbance Rejection are Unaffected by Longitudinal Gains)



Figure 2.10.9 Phase Margin versus Longitudinal DRB Design Chart

This chapter presented one method for gain optimization using the tradeoff of DRB and Stability Margins.   Another approach is to use direct optimization based on simulation time history results. This will be presented in the following chapter.

## 2.11  Task 11 Control parameter optimization

Efforts were made to develop a method to find optimized control parameters to enhance the path tracking performance. The inner-loop feedback control system (attitude control) was first considered (Figure 2.11.1). The optimization method used in this study was KSOPT (Kreisselmeier-Steinhauser OPTimizer). The KS function combines multiple objective functions with the constraints to form a single composite function (KS function), which can, in turn, be optimized by using the unconstrained optimization techniques. The KS function was first used by Kreisselmeier and Steinhauser and is defined as

$$K(\vec{x}) = \frac{1}{\rho}\ln\sum_{m=1}^{M}e^{\rho F_m(\vec{x})}$$

where $\rho$ is a scalar multiplying factor used in the KS function and $F_m(\vec{x})$ is a set of $M$ functions, which, in the current context, are the objective functions and the constraints. To convert the original constrained optimization problem to an unconstrained optimization problem, the KS function combines the objective functions with the constraint functions into a single composite function. This unconstrained KSOPT has been incorporated into FLIGHTLAB as a general purpose constrained minimization component.
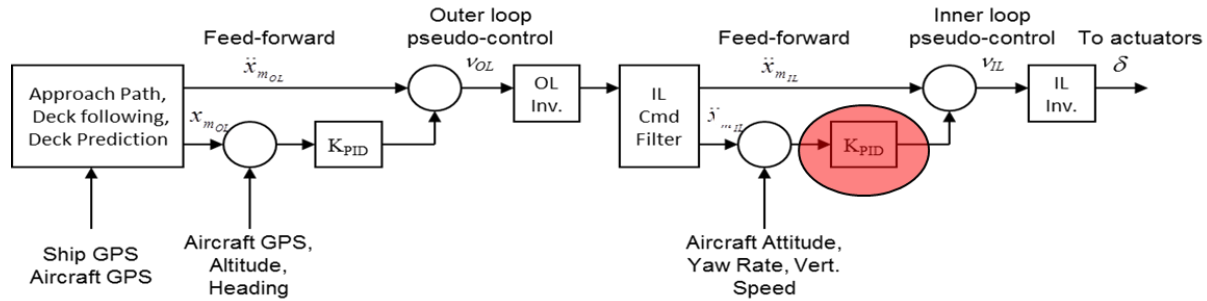


Figure 2.11.1 Dynamic inversion control system

The KSOPT component was written using a modular approach which allows portions of a component to be replaced easily as new and improved methods are developed. It should be noted that the user must provide the appropriate function to evaluate the desired costs and constraints for the optimizer. Once all the required information is determined, the optimization problem is then initialized to allocate space for internal arrays and to test the initial design variables. The KSOPT component is then called in a loop with the user supplied analysis procedures until the optimization problem is solved. At each iteration, the initial function value and the derivatives of the KS function are obtained from the function values/derivatives of the objective functions and constraint functions supplied by the user. After forming the composite KS function value and gradient with respect to the design variable, an unconstrained optimization problem related to the KS function is defined and can be solved iteratively. This unconstrained problem is solved by first finding a search direction vector, using the Davidon-Fletcher-Powell (DFP) algorithm. The above implementation of the unconstrained optimization procedure treats the side constraints on the design variables separately from the other general

constraints since it is sometimes desirable to approach the side constraints as closely as possible without violating them. Forming the side constraints on the design variables in the same way as the general constraints will not allow the optimization to approach the side constraint closely. Therefore, in the KSOPT method, the side constraints are inherently tackled inside the one dimensional line search procedure described above.

The proposed optimization process has been tested using a light weight class helicopter model with the SCONE2 ship motion. The inner loop feedback controller consists of 10 total gains (3 lateral gains, 3 longitudinal gains, 2 collective gains, and 2 pedal gains) to be tuned. Four tracking errors (roll, pitch, yaw, and vertical speed) were assigned as an objective function for each channel. It should be noted that each channel is assumed to be independent during the optimization process. Thus, the calculation of the objective's gradient is slightly modified to remove any cross-coupling effects among the control channels. The objective functions are formed as the sum of the squared tracking error for faster convergence. In addition, the KSOPT based optimization process has been applied to the outer-loop pseudo-control system. Similar to the inner-loop controller, a total of 10 gains (3 lateral gains, 3 longitudinal gains, 2 collective gains, and 2 pedal gains) were tuned and the outer-loop control system was applied for the optimization such that the tracking errors (aircraft position and heading angle) in the outer-loop were used to form a cost function of the optimization.

It was relatively straightforward to use the tracking errors to form the objective functions for the inner-loop control system. However, it is somewhat redundant to use the tracking error for the cost function for optimization of the outer-loop control system since a different form of tracking error was already used for optimization of the inner-loop control system. Further effort will be focused on the formulation of the cost function to enhance the overall optimization process.

Figures 2.11.2 through 2.11.5 show some representative simulation results with the optimized gains for an approach and station-keeping maneuver. The overall behavior and performance are similar to the simulation with the original gain set. However, one noticeable difference is the reduction of overshoot in the heave channel when the aircraft attempts to stop descending. It is hypothesized that the KS cost function for the inner loop feedback controller is dominated by the heave error because the attitude error is smaller than the position error.
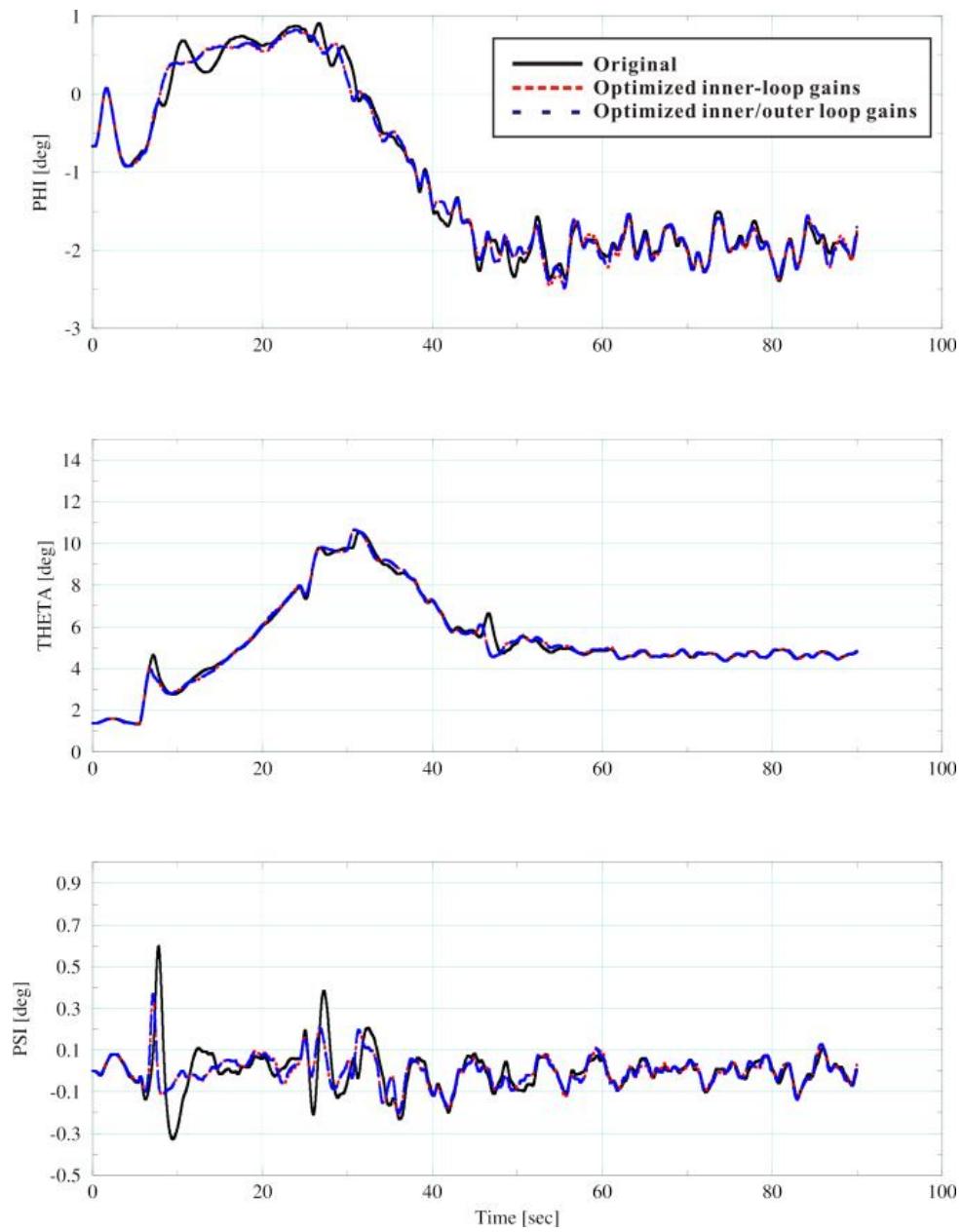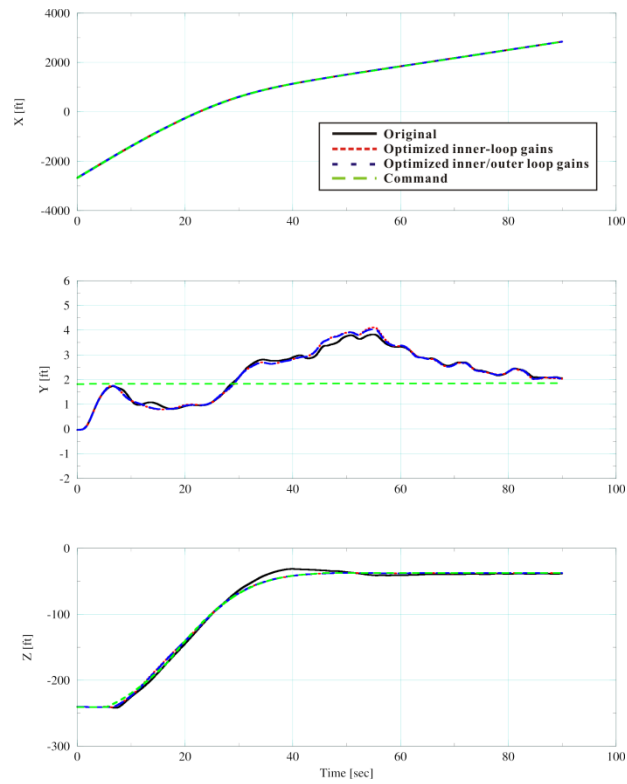
**Figure 2.11.2 Aircraft attitude**
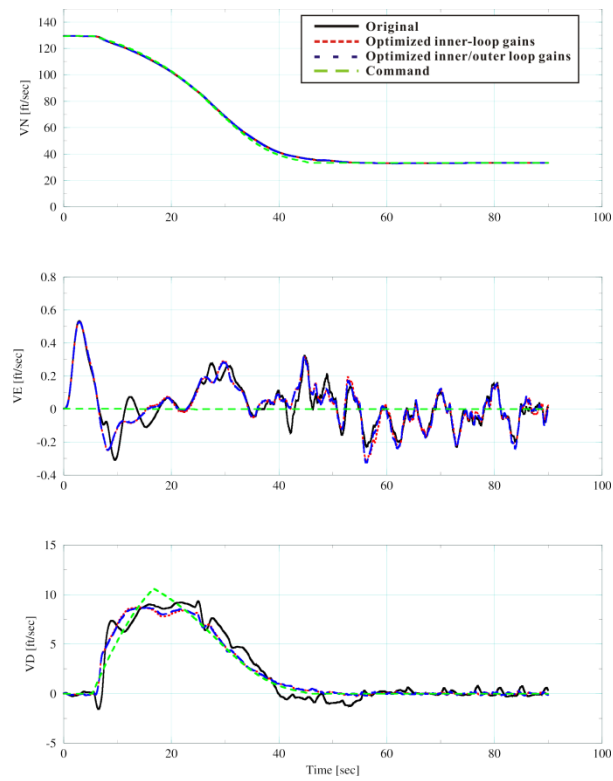
**Figure 2.11.2 Aircraft position**

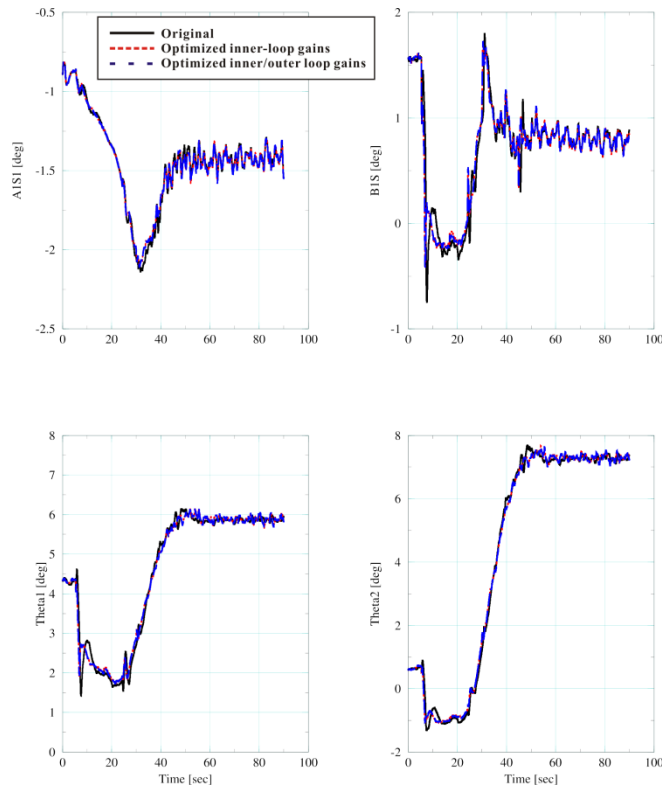

**Figure 2.11.4 Aircraft velocity**

**Figure 2.11.3 Swash plate control inputs**

## 2.12 Task 12 Path optimization of VTOL UAV

Task 12 is an extension of Task 6 (Path Optimization of Shipboard Helicopter) but applied to a smaller VTOL UAV.  In this section, results from two optimization studies are presented that illustrate 1) the application of the Task 6 methodology to a smaller VTOL UAV and 2) the effect of varied wind-over-deck (WOD) conditions on the path optimization results.

### 2.12.1 Simulation Overview
For this, the FLIGHTLAB simulation of the light-class VTOL UAV was used along with Dynamic Inversion control law as described in the previous sections. Once again the ship motion used a steady forward speed with no dynamic roll / pitch, and the ship airwake used nonuniform mean and turbulent variations derived from the SFS2 CFD solutions (as with the medium class).  However, in this study approaches to the ship were performed in 20 kts WOD with both 0° and 30° relative wind.  The 30° WOD case allows us to study the effect of asymmetric wind conditions on the path optimization.

### 2.12.2 Optimization Framework
As with the optimization studies in Task 6, the shipboard approach is formulated mathematically as a numerical optimization problem and cast into nonlinear mathematical programming form.  The general optimization procedure consists of finding the value of a vector of design variables $X$ such that a scalar objective function $F(X)$ is minimized. In practice, the optimization problem is converted into a sequence

of approximate optimization problems in which the objective function is replaced by function approximation $F_{app}(\boldsymbol{X})$.

### 2.12.2.1 Approach Profile Design Vector

As with Task 6, the approach profile utilized in the present study is the extended version of Heffley's mathematical formulation of longitudinal deceleration and velocity profiles for a visual helicopter approach, and the same four variables are used in the design vector, i.e., $\boldsymbol{X} = [v_0\ r_{pd}\ \gamma\ \psi]^T$. Each design variable is subjected to side constraints which, for the present study, were

$$100 \text{ ft/sec} \leq v_0 \leq 150 \text{ ft/sec} \tag{2.12.1}$$

$$100 \text{ ft} \leq r_{pd} \leq 500 \text{ ft} \tag{2.12.2}$$

$$1 \text{ deg} \leq \gamma \leq 15 \text{ deg} \tag{2.123}$$

$$-45 \text{ deg} \leq \psi \leq 45 \text{ deg} \tag{2.12.4}$$

The optimization procedure began with an initial inventory of approach profile designs. The baseline approach profile was $\boldsymbol{X}_1 = [v_0\ r_{pd}\ \gamma\ \psi]^T = [125 \text{ ft/sec}\quad 300 \text{ ft}\quad 8 \text{ deg}\quad 0 \text{ deg}]^T$, and the remainder of the initial inventory of designs was based on a sensitivity study, i.e., the baseline plus a positive and negative perturbation for each of the four variables in the design vector.

### 2.12.2.2 Objective Function

The objective functions $F(\boldsymbol{X})$ in the present study were similar to the objective functions used in Task 6 in order to account for multiple performance factors: 1) the maneuver duration, 2) the power requirements over the course of the maneuver, 3) path error along the maneuver, and 4) the effects of the turbulent ship airwake. To achieve the, the same $k_1$, $k_2$, $k_3$ terms were used for integrated power, tracking error, and thrust fluctuations. However, the normalization for the first performance factor, i.e. the work performed over the duration of the maneuver, was scaled by the induced power required in a hover (215 ESHP for the VTOL UAV versus 1221 ESHP for the helicopter in Task 6) such that the performance factor was:

$$k_1 = \frac{W}{350 \text{ hp-min}} \tag{2.12.5}$$

The second performance factor, i.e., the mean path error, was identical to that from Task 6:

$$k_2 = \frac{\bar{\varepsilon}}{25 \text{ ft}} \tag{2.12.6}$$

The normalization factor for the third performance factor, i.e., the peak thrust fluctuation, was scaled by the gross weight of the helicopter such that the performance factor was:

$$k_3 = \frac{\max(\Delta T(t))}{470 \text{ lbs}} \tag{2.12.7}$$

The objective functions included all three performance parameters, i.e.,

$$F^1(\boldsymbol{X}) = (k_1(\boldsymbol{X}) + k_2(\boldsymbol{X}) + k_3(\boldsymbol{X}))/3 \tag{2.12.8}$$

and

$$F^2(\boldsymbol{X}) = w_1 k_1(\boldsymbol{X}) + w_2 k_2(\boldsymbol{X}) + w_3 k_3(\boldsymbol{X}) \tag{2.12.9}$$

where $w_1 = w_2 = 0.1$, $w_3 = 0.8$.

### 2.12.2.3 Constraints

Behavior constraints were applied to the optimization procedure to ensure that the resulting approach profiles were both realistic and safe. The first behavior constraint was imposed to limit the maximum pitch attitude experienced by the aircraft over the duration of the maneuver to be no more than 15 deg; that is,

$$g_1(\boldsymbol{X}) = \vartheta_{\max}(\boldsymbol{X}) - 15 \text{ deg} \leq 0 \qquad (2.12.10)$$

A second behavior constraint was imposed to prevent approach profiles in which the aircraft would be likely to descend to within 10 feet of the ship deck (the approach maneuver terminated at a height of 20 feet above the ship deck); that is,

$$g_2(\boldsymbol{X}) = 10 \text{ ft} - [\min(h_{ac}(\boldsymbol{X})) - h_{deck}] \leq 0 \qquad (2.12.11)$$

### 2.12.2.4 Approximate Problem Formulation

The optimization problem was not solved by directly connecting the simulation and the optimizer; rather, the baseline optimization problem was converted into a sequence of computationally inexpensive approximate optimization problems in which the objective function and behavior constraints were replaced by approximations that were updated at each step of the sequence. The objective and constraint functions were replaced with approximations based on a Radial Basis Function (RBF) that were generated from the exact function evaluations. Additionally, move limits were imposed such that each design variable could not traverse more than 25% of the design space in a single optimization step; that is,

$$-0.25(\boldsymbol{X}_{\max} - \boldsymbol{X}_{\min}) \leq \boldsymbol{X}_k - \boldsymbol{X}_{k-1} \leq 0.25(\boldsymbol{X}_{\max} - \boldsymbol{X}_{\min}) \qquad (2.12.12)$$

where $\boldsymbol{X}_{k-1}$ is the best feasible design from the current inventory.
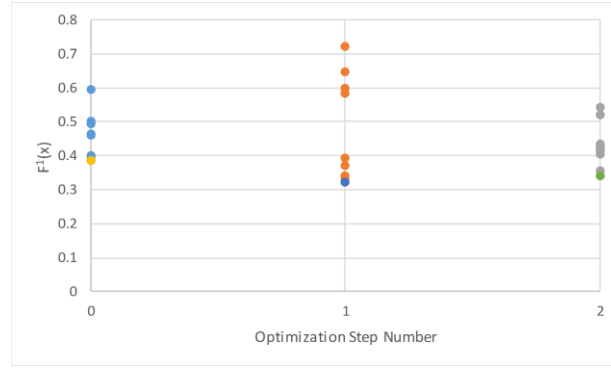
### 2.12.2.5 Additional Designs

To improve the global convergence characteristics of the methodology, additional designs were generated during the course of the optimization. The designs computed in this way were not necessarily better designs; however, they can improve the mathematical properties of the overall optimization by improving the accuracy of the approximate objective function and improving the global convergence characteristics.
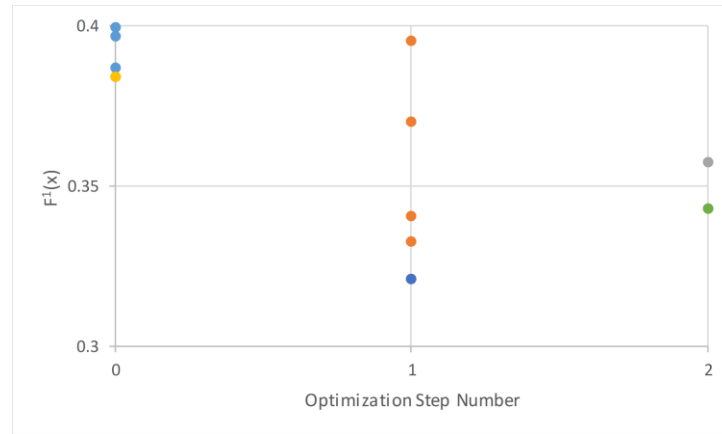
### 2.12.3 Results

### 2.12.3.1 Primary Objective Function for 0° WOD

A summary of the progression of the optimization procedure for the 0° WOD primary objective function, i.e., Eq. (2.12.8), is shown in Fig. 2.12.1. The best design at each step is shown by a different colored dot. The approach profiles described by $\boldsymbol{X}_1$–$\boldsymbol{X}_9$ comprise the initial sensitivity study that served to explore the design space before initiating any formal optimization steps (i.e., step zero). The objective function values for the initial sensitivity study ranged from 0.3842–0.5949. The best design from the initial inventory was:

$$\boldsymbol{X}_3 = [v_0 \ r_{pd} \ \gamma \ \psi]^T = [125 \text{ ft/sec} \quad 300 \text{ ft} \quad 15 \text{ deg} \quad 0 \text{ deg}]^T$$

a) All function evaluations



b) Best function evaluations

Figure 2.12.1.  Optimization history; that is, objective, function values vs. step number, for $F^1_{app}(X_{temp})$.

The first optimization step included runs $X_{10}$–$X_{21}$, where $X_{10}$ was the optimum of the approximation to the primary objective function, $F^1_{app}(X_1$–$X_9)$, $X_{11}$ was the optimum of the approximation to the secondary objective function, $F^2_{app}(X_1$–$X_9)$ (which may be treated as an additional design for the primary optimization), and $X_{12}$–$X_{21}$ were computed using the additional design objective function.  The best design evaluated at this step was an additional design; that is,

$$X_{16} = [v_0\ r_{pd}\ \gamma\ \psi]^T = [100\ ft/sec\quad 190.01\ ft\quad 15\ deg\quad 44.998\ deg]^T$$

The second optimization step included runs $X_{22}$–$X_{33}$, where $X_{22}$ was the optimum of the approximation to the primary objective function, $F^1_{app}(X_1$–$X_{21})$, $X_{23}$ was the optimum of the approximation to the secondary objective function, $F^2_{app}(X_1$–$X_{21})$, and $X_{24}$–$X_{33}$ were computed using the additional design objective function.  The best design evaluated at this step was also an additional design; that is,

$$X_{29} = [v_0\ r_{pd}\ \gamma\ \psi]^T = [100.01\ ft/sec\quad 190.1\ ft\quad 14.989\ deg\quad -36.91\ deg]^T$$

Notice in Fig. 2.12.1-b that the objective function values for the best design at each step are very close; therefore, the optimization was terminated.  In fact, the objective function values for the best designs from the first and second steps nearly equal, $F^1(\boldsymbol{X}_{16})$ - $F^1(\boldsymbol{X}_{24})\approx 0.217$.  The best designs for the first and second optimization step are very similar designs, mainly differing in $\psi$.  The approximation to the primary objective function that was constructed from all 33 approach profile designs is shown in Figure 2.12.2.   Notice that, although the objective function appears to be quite sensitive to $\boldsymbol{X}_{\text{temp}}$ (i.e., it exhibits drastic variations in a given subfigure), it is somewhat insensitive to $\boldsymbol{X}_{\text{spatial}}$ (i.e., it exhibits only subtle variations between subfigures). Although the primary objective function is fairly insensitive to $\boldsymbol{X}_{\text{spatial}}$, there is a clear trend that as $\gamma$ increases $F^1_{\text{app}}(X)$ decreases.



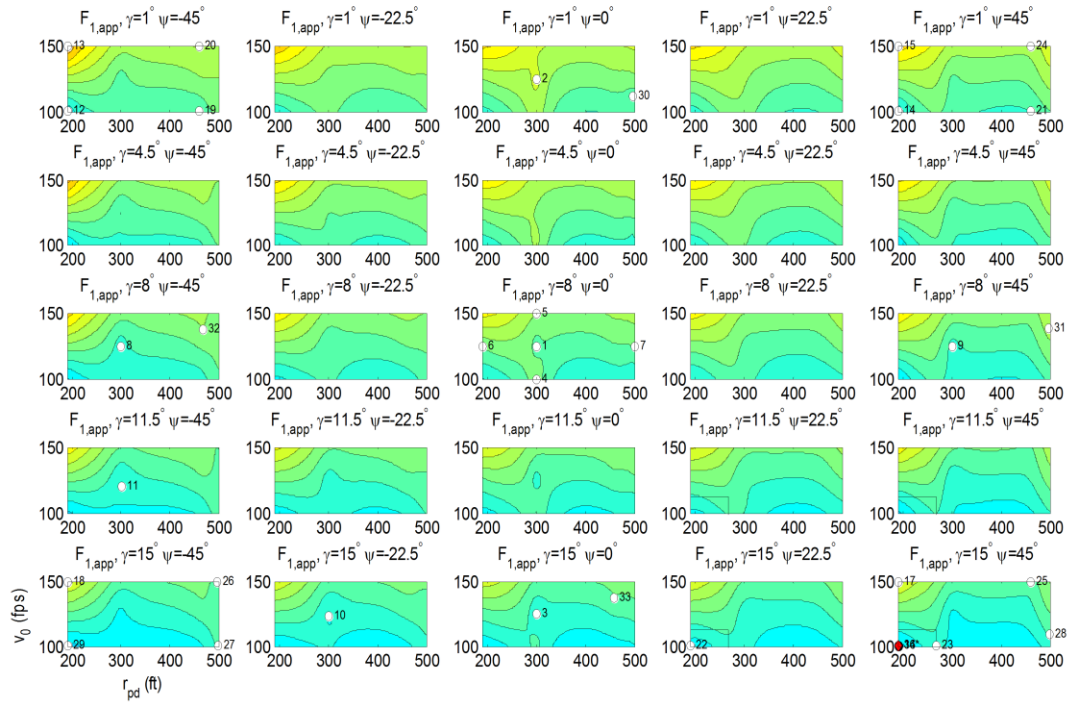**Figure 2.12.2.   Contour maps for $F^1_{\text{app}}(X_{\text{temp}})$ over a range of values for $X_{\text{spatial}}$.**

### 2.12.3.2  Secondary Objective Function for 0° WOD

A summary of the progression of the optimization procedure for the 0° WOD secondary objective function is shown in Figure 2.12.3.  Once again, the approach profiles described by $\boldsymbol{X}_1$–$\boldsymbol{X}_9$ comprise the initial sensitivity study that served to explore the design space before initiating any formal optimization steps.   As seen with the primary objective function, the objective function values for the initial sensitivity study ranged from 0.4051–0.8915.  There are two best designs from the initial inventor

$$\boldsymbol{X}_8 = [v_0\ r_{pd}\ \gamma\ \psi]^{\mathrm{T}} = [125\ \text{ft/sec}\quad 300\ \text{ft}\quad 8\ \text{deg}\quad -45\ \text{deg}]^{\mathrm{T}}$$

$$\boldsymbol{X}_9 = [v_0\ r_{pd}\ \gamma\ \psi]^{\mathrm{T}} = [125\ \text{ft/sec}\quad 300\ \text{ft}\quad 8\ \text{deg}\quad 45\ \text{deg}]^{\mathrm{T}}$$
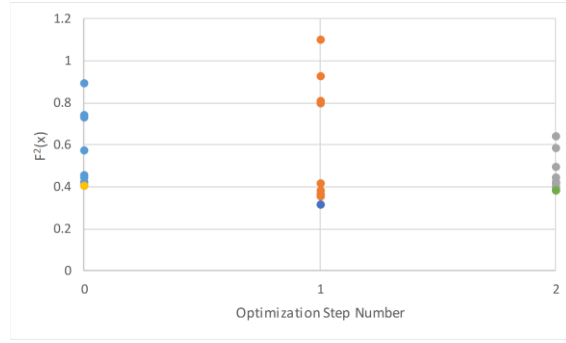
**a) All function evaluations**
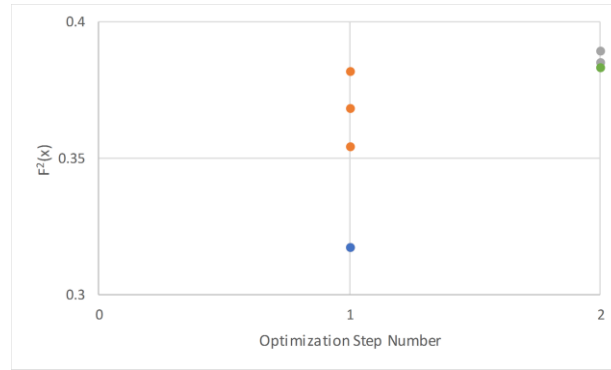


**b) Best function evaluations**

**Figure 2.12.3.   Optimization history; that is, objective, function values vs. step number, for $F_{\text{app}}^2(X_{\text{temp}})$.**

Each step of the optimization included the same runs described previously for the primary objective function, though, in this case, the optimal designs from the primary optimization were treated as additional designs for the secondary optimization.  The best design evaluated in the first step was an additional design; that is,

$$X_{16} = [v_0\ r_{pd}\ \gamma\ \psi]^{\mathsf{T}} = [100\ \text{ft/sec}\quad 190.01\ \text{ft}\quad 15\text{deg}\quad 44.998\ \text{deg}]^{\mathsf{T}}$$

The best design evaluated in the second step was also an additional design; that is,

$$X_{29} = [v_0\ r_{pd}\ \gamma\ \psi]^{\mathsf{T}} = [150\ \text{ft/sec}\quad 496.8\ \text{ft}\quad 15\ \text{deg}\quad -45\ \text{deg}]^{\mathsf{T}}$$

he approximation to the secondary objective function that was constructed from all 45 approach profile designs is shown in Figure 2.12.4.  As with the primary objective function, the secondary objective function appears to be quite sensitive to $X_{\text{temp}}$ (i.e., it exhibits drastic variations in a given subfigure in Figure 2.12.4) although it is somewhat insensitive to $X_{\text{spatial}}$ (i.e., it exhibits only subtle variations between subfigures in Figure 2.12.4). There is a clear trend in $F_{\text{app}}^2(X)$ with $X_{\text{spatial}}$, as both $\gamma$ and $\psi$ increase, $F_{\text{app}}^2(X)$ decreases.
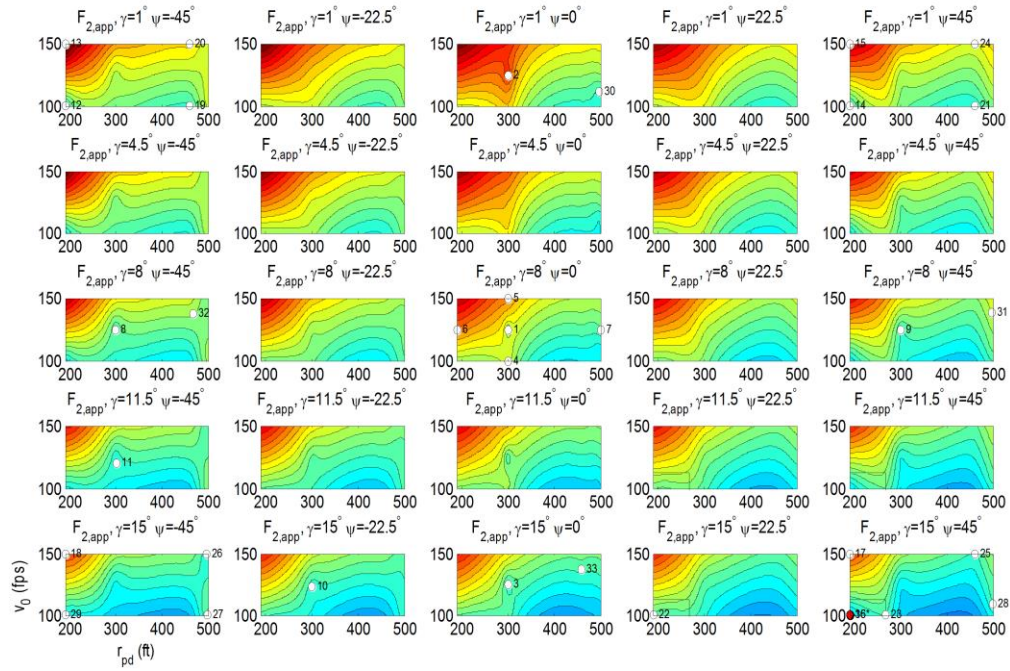
**Figure 2.12.4.** Contour maps for $F_{app}^2(X_{temp})$ over a range of values for $X_{spatial}$.

### 2.12.3.3 Primary Objective Function 30° WOD

A summary of the progression of the optimization procedure for the 30° WOD primary objective function is shown in Fig. 2.12.5. Once again, the approach profiles described by $X_1$–$X_9$ comprise the initial sensitivity study that served to explore the design space before initiating any formal optimization steps. As seen with the primary objective function, the objective function values for the initial sensitivity study were similar and ranged from 0.4205–0.5485 despite the fact that the approach profiles spanned the design space. The best designs from the initial inventory was:

$$X_8 = [v_0 \ r_{pd} \ \gamma \ \psi]^T = [125 \text{ ft/sec} \quad 300 \text{ ft} \quad 8 \text{ deg} \quad -45 \text{ deg}]^T$$
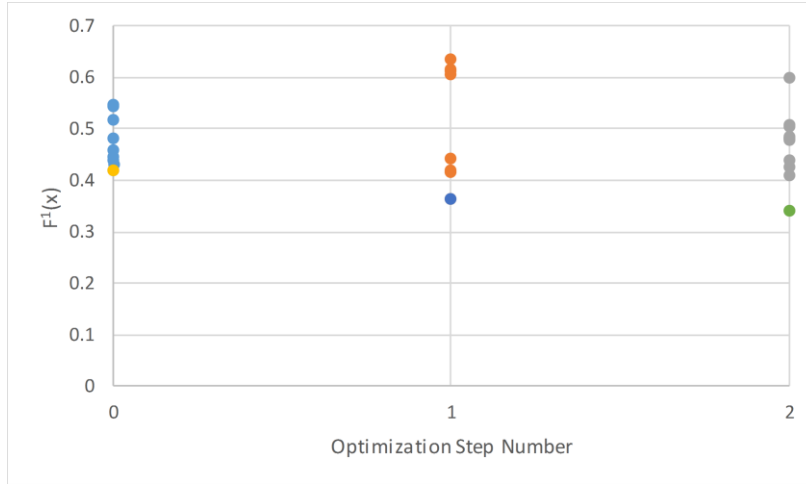
a) All function evaluations
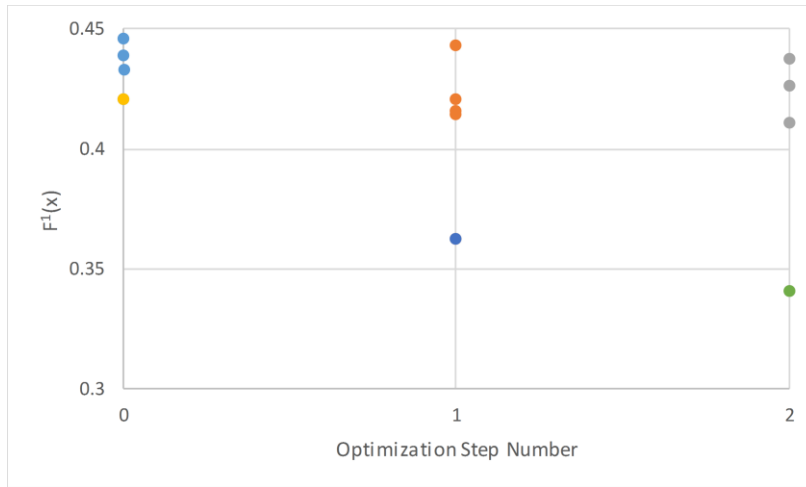


b) Best function evaluations

**Figure 2.12.5.   Optimization history; that is, objective, function values vs. step number, for $F_{app}^2(X_{temp})$.**

The best design evaluated in the first step was an additional design; that is,

$$\boldsymbol{X}_{16} = [v_0\; r_{pd}\; \gamma\; \psi]^T = [100.001\text{ ft/sec}\quad 190.0055\text{ ft}\quad 14.9997\text{deg}\quad 44.9982\text{ deg}]^T$$

The best design evaluated in the second step was also an additional design; that is,

$$\boldsymbol{X}_{29} = [v_0\; r_{pd}\; \gamma\; \psi]^T = [100.1775\text{ ft/sec}\quad 190.7393\text{ft}\quad 14.9517\text{ deg}\quad -18.285\text{ deg}]^T$$

The approximation to the secondary objective function that was constructed from all 33 approach profile designs is shown in Fig. 2.12.6.  As with the primary objective function, the secondary objective function appears to be quite sensitive to $\boldsymbol{X}_{temp}$ (i.e., it exhibits drastic variations in a given subfigure in

Fig. 2.12.6) although it is somewhat insensitive to $\boldsymbol{X}_{\text{spatial}}$ (i.e., it exhibits only subtle variations between subfigures in Fig. 2.12.6). There is a clear trend in $F^1_{\text{app}}(X)$ to $\boldsymbol{X}_{\text{spatial}}$, as both $\gamma$ *increases* $F^1_{\text{app}}(X)$ *decreases.*



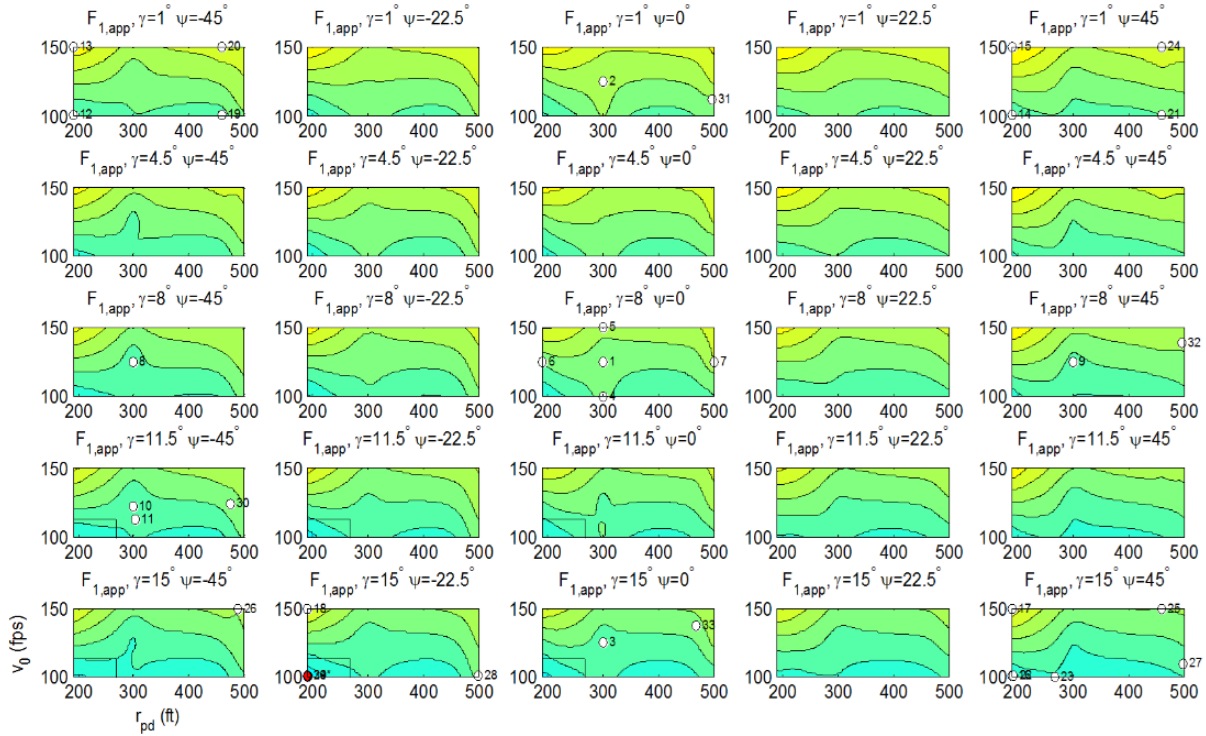**Figure 2.12.6. Contour maps for $F^1_{\text{app}}(X_{\text{temp}})$ over a range of values for $X_{\text{spatial}}.$**

### *2.12.3.4 Secondary Objective Function 30° WOD*

A summary of the progression of the optimization procedure for the 30° WOD primary objective function is shown in Fig. 2.12.7. Once again, the approach profiles described by $\boldsymbol{X}_1$–$\boldsymbol{X}_9$ comprise the initial sensitivity study that served to explore the design space before initiating any formal optimization steps. As seen with the primary objective function, the objective function values for the initial sensitivity study ranged from 0.4548–0.7388. The best designs from the initial inventory was:

$$\boldsymbol{X}_8 = [v_0 \; r_{pd} \; \gamma \; \psi]^T = [125 \text{ ft/sec} \quad 300 \text{ ft} \quad 8 \text{ deg} \quad \text{-45 deg}]^T$$
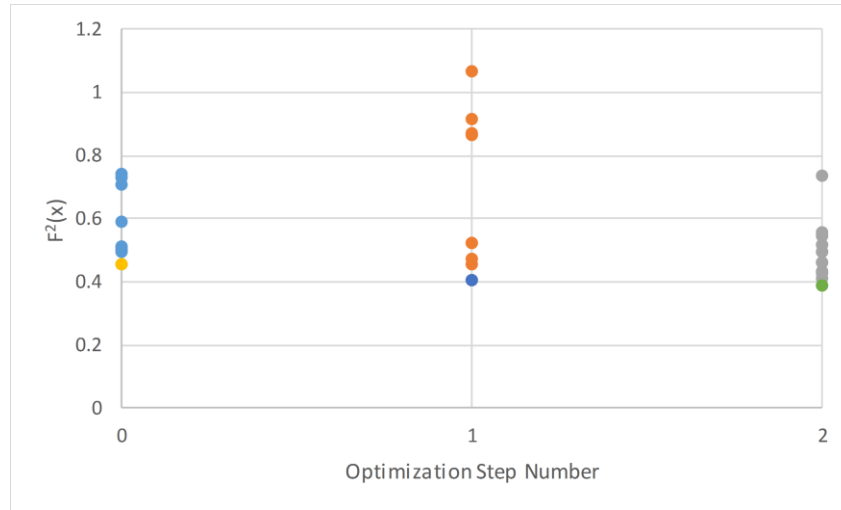
a) All function evaluations
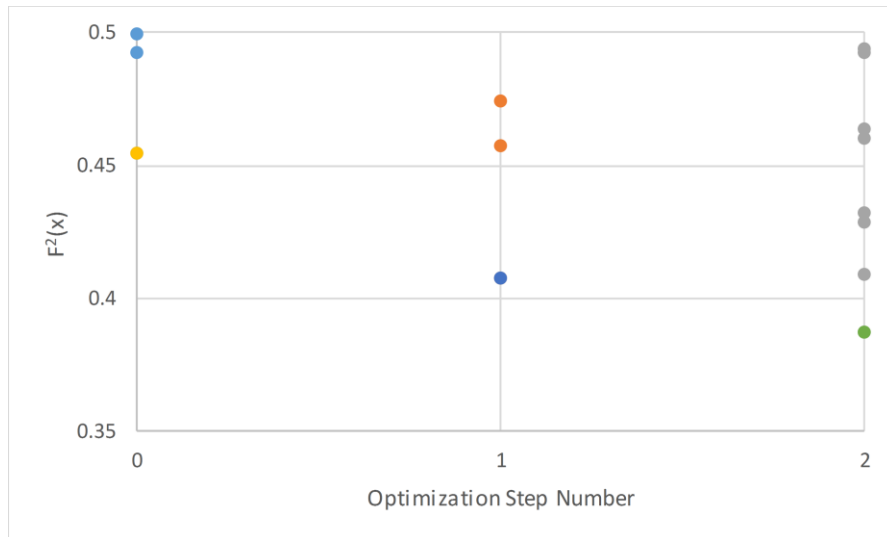


b) Best function evaluations

**Figure 2.12.7.  Optimization history; that is, objective, function values vs. step number, for $F_{\text{app}}^2(X_{\text{temp}})$.**

The best design evaluated in the first step was an additional design; that is,

$$X_{16} = [v_0 \; r_{pd} \; \gamma \; \psi]^T = [100.001 \text{ ft/sec} \quad 190.0055 \text{ ft} \quad 14.9997 \text{deg} \quad 44.9982 \text{ deg}]^T$$

The best design evaluated in the second step was also an additional design; that is,

$$X_{29} = [v_0 \; r_{pd} \; \gamma \; \psi]^T = [100.1775 \text{ ft/sec} \quad 190.7393 \text{ft} \quad 14.9517 \text{ deg} \quad -18.285 \text{ deg}]^T$$

The approximation to the secondary objective function that was constructed from all 33 approach profile designs is shown in Fig. 2.12.8. As with the primary objective function, the secondary objective function appears to be quite sensitive to $X_{temp}$ (i.e., it exhibits drastic variations in a given subfigure in Fig. 2.12.8) although it is somewhat insensitive to $X_{spatial}$ (i.e., it exhibits only subtle variations between subfigures in Fig. 2.12.8). There is a clear trend in $F_{app}^2(X)$ to $X_{spatial}$, as both $\gamma$ and $\psi$ increase $F_{app}^2(X)$ decreases.



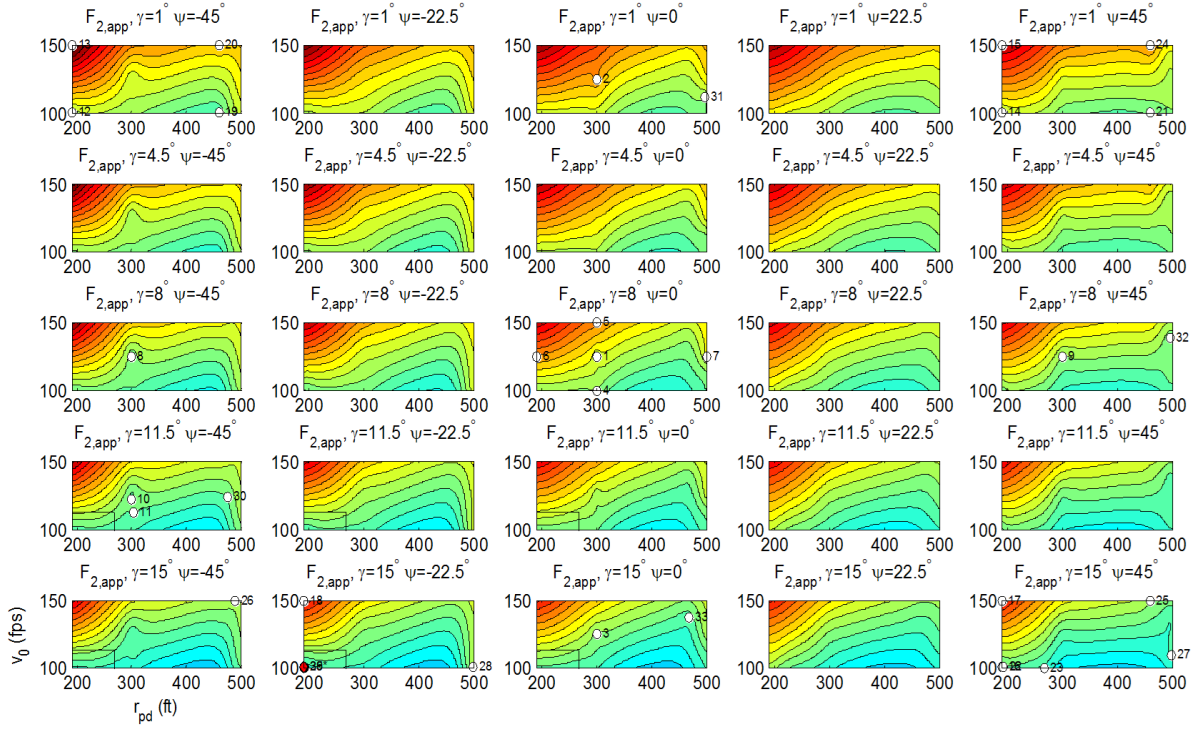**Figure 2.12.8.  Contour maps for $F_{app}^1(X_{temp})$ over a range of values for $X_{spatial}$.**

### 2.12.3.5 Discussion

To gain a better understanding of the optimization results, the individual performance metrics were also evaluated separately.  To make these assessments, RBF-based approximations for both 0° and 30° WOD cases to the various performance factors were computed.  Figure 2.12.9 shows RBF-based approximations for: 1) $k_1(X)$, i.e., normalized work, 2) $k_2(X)$, i.e., normalized mean path error, and 3) $k_3(X)$, i.e., the maximum thrust fluctuations caused by ship airwake for the baseline

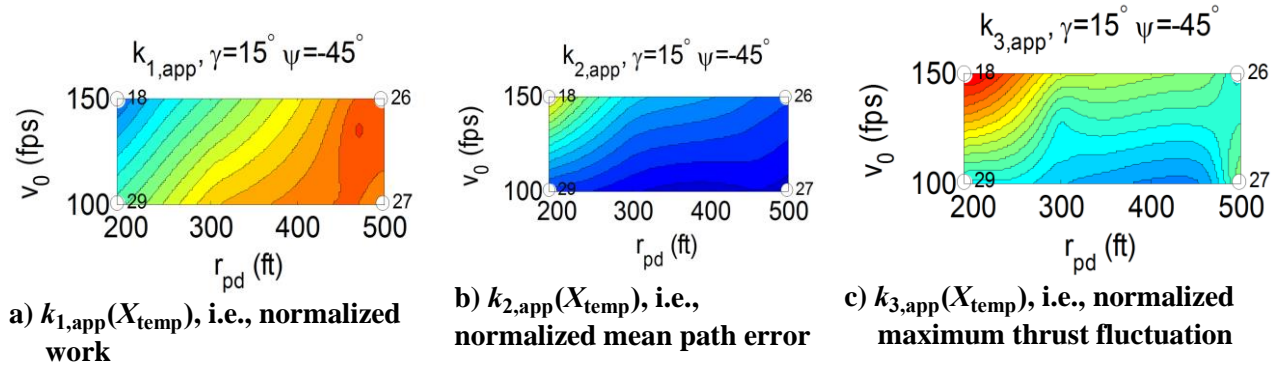$$X_{spatial} = [\gamma \ \psi]^T = [8 \text{ deg} \quad 0 \text{ deg}]^T.$$

a) $k_{1,app}(X_{temp})$, i.e., normalized work

b) $k_{2,app}(X_{temp})$, i.e., normalized mean path error

c) $k_{3,app}(X_{temp})$, i.e., normalized maximum thrust fluctuation

**Figure 2.12.9.** $0\,°$ **WOD Contour maps of the various performance factors over a range of values for** $X_{spatial} = [\gamma\;\psi]^{T} = [\textbf{15deg} \;\;\textbf{-45 deg}]^{T}.$

The results in Fig. 2.12.9-a clearly show that the work is minimized for more aggressive approach profiles, i.e., approach profiles with increased $v_0$ and reduced $r_{pd}$.  The results for mean path error (Fig. 2.12.9-b) show a similar sensitivity to the aggressiveness of the approach profile; however, performance is improved for less aggressive approach profiles for the case of mean path error.  Both the $k_1(X)$ and $k_2(X)$ performance factors were generally insensitive to $X_{spatial}$.  Notice that the maximum thrust fluctuation performance factor (Fig. 2.12.10) is highly nonlinear and nonconvex over $X_{temp}$.  While this performance factor exhibited some sensitivity to $X_{spatial}$, the results suggested that, for the present study, the airwake effects are similar for all oblique approaches (i.e., regardless of whether the approach profile is from the port or starboard side of the ship).  This result is likely attributable to the simplified SFS2 hull shape and 0° relative winds.
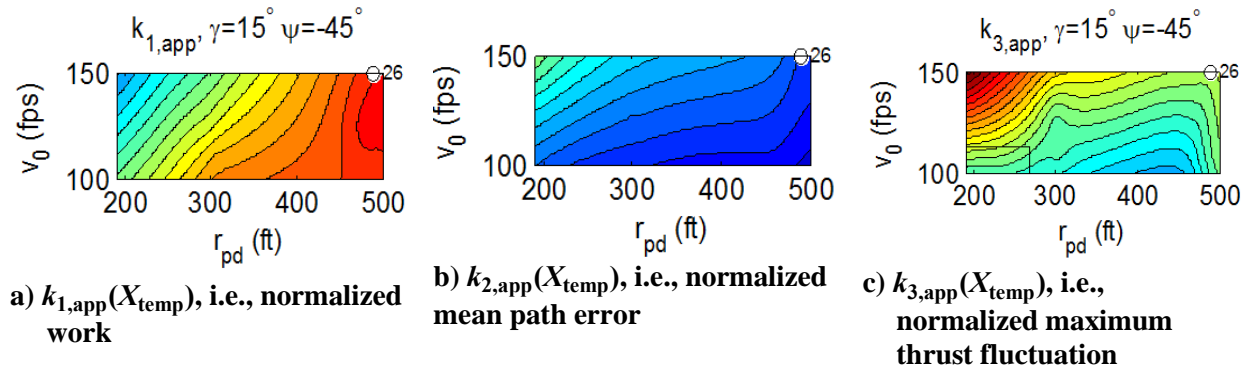


a) $k_{1,app}(X_{temp})$, i.e., normalized work

b) $k_{2,app}(X_{temp})$, i.e., normalized mean path error

c) $k_{3,app}(X_{temp})$, i.e., normalized maximum thrust fluctuation

**Figure 2.12.10.** $30\,°$ **WOD Contour maps of the various performance factors over a range of** $X_{spatial} = [\gamma\;\psi]^{T} = [\textbf{15deg} \;\;\textbf{-45 deg}].$

The results in Fig. 2.12.10-a clearly show that the work is minimized for more aggressive approach profiles, i.e., approach profiles with increased $v_0$ and reduced $r_{pd}$.  The results for mean path error (Fig. 2.12.10-b) show a similar sensitivity to the aggressiveness of the approach profile; however, performance is improved for less aggressive approach profiles for the case of mean path error.  Both the $k_1(X)$ and $k_2(X)$ performance factors were generally insensitive to $X_{spatial}$.  Notice that the maximum

thrust fluctuation performance factor (Fig. 2.12.10) is highly nonlinear and nonconvex over $X_{temp}$. Unlike the 0° WOD case, this performance factor, $k_3(X)$, exhibits significant sensitivity to $X_{spatial}$, as the results in Figure 2.12.11 demonstrate. The difference in results between the 0° and 30° WOD cases, suggest that WOD angle plays a significant role in maximum thrust fluctuation performance.
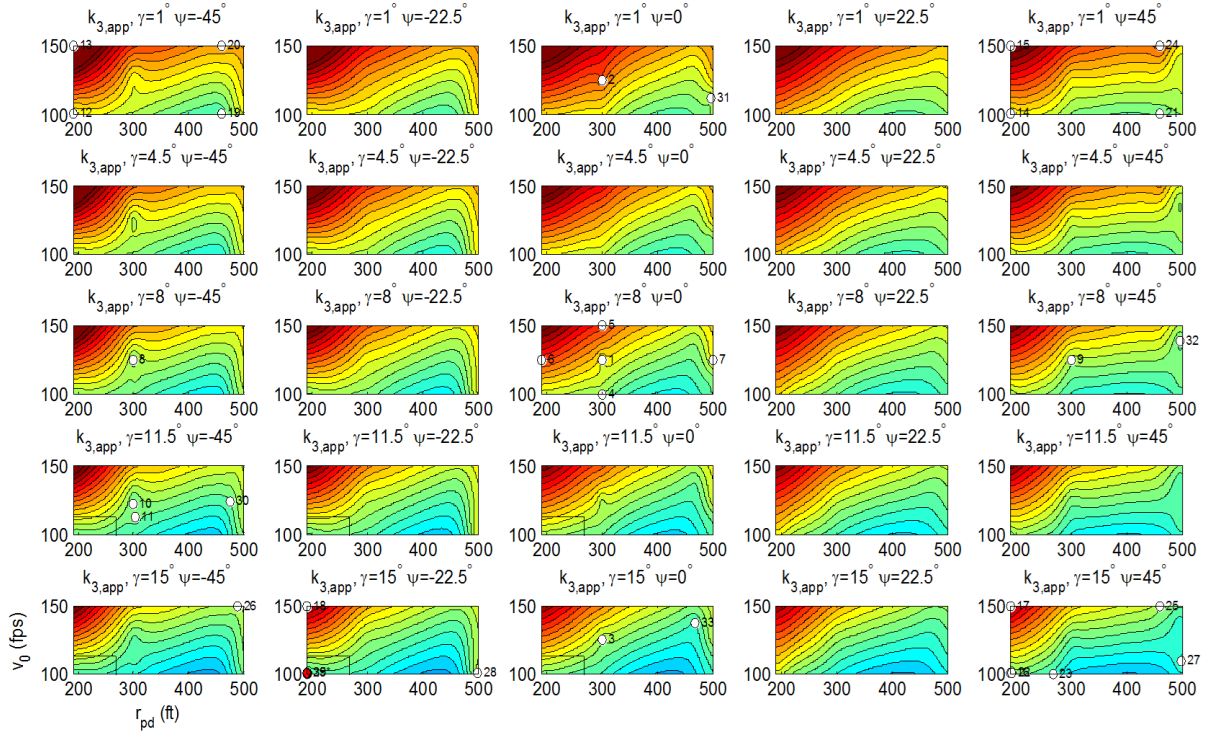


**Figure 2.12.11. 30 °WOD Contour maps of the $k_{3,app}(X_{temp})$ over a range of $X_{spatial}$.**

### 2.12.4 Conclusion

From this analysis, the following conclusions have been drawn:

As with the analysis in 2.6, the study indicates that it is possible to generate objective functions that include multiple performance factors, and that the relative weighting of performance factors may be tailored in accordance with operational considerations. The weighting factors and normalization factors must be carefully selected to maintain a suitable balance between multiple performance factors that may oppose each other. The thrust fluctuations caused by the turbulent ship airwake were the primary driver of the objective function characteristics. This observation was especially noted in the 30° WOD case, where the WOD angle caused significant sensitivity across the spatial design space. This relationship was a result of the relative weighting between performance factors and the normalization factors that were applied to each performance factor.

Second, results indicate that the mathematical properties of the resulting optimization problem are likely to be dependent on the specific performance factors included in the objective function as well as their relative weights. This dependency may have implications on the tractability of trajectory optimization studies with certain objective function formulations. In the present study, both objective

functions for both WOD angle cases were highly nonlinear and nonconvex. The optimization method produced some improvement in the objective functions, but for both WOD cases step 2 had a less optimal design than step 1. In future study, it would be prudent have more optimization steps in order to observe minimal difference in objective function value for the best designs.

Last, the segmentation between the temporal and spatial variables within the proposed approach profile design vector appears to be particularly effective for comparing sensitivities of performance parameters to $X_{spatial}$, the path through space that the helicopter will follow, and $X_{temp}$, the way in which the aircraft will traverse that path. In the present study, the objective functions were highly sensitive to $X_{temp}$ and less sensitive to $X_{spatial}$. In particular, the results generally showed little sensitivity to the ship-relative azimuth angle, $\psi$. This may be attributable to the use of a simplified ship structure (the SFS2) and 0° relative winds. While the previous three statements are true for the 0° WOD case, the 30° WOD case demonstrates significant sensitivity in $\psi$ as noted in figure 2.12.11. Future work could look at more optimization studies for additional WOD conditions to investigate the impact of WOD conditions on optimal helicopter approaches.

## 2.13  Task 13 Prototype testing and evaluation

Extensive tests and evaluations have been performed on helicopter models of the different classes. Focus was put on medium class, where the SCONE data and deck motion forecasting have been incorporated.

Statistical analysis was performed on the medium class to investigate the various landing approaches – including the deck tracking method and the methods using deck prediction. Thirty cases with randomized turbulence distribution and ship motion were tested for method, Figure 2.13.1 demonstrates the landing quality of Deck Tracking Method, Figure 2.13.2 demonstrates the performance for Deck Prediction Using Optimal Guidance Law, and Figure 2.13.3 shows performance for Deck Prediction Using Path Optimizations. Table 2.13.1 showed a comparative study of both methods in terms of statistical metrics of landing quality. The deck tracking method is found to perform more consistently than either of the predictive landing methods. The analysis suggests that the predictive methods are sensitive to inaccuracy in the forecasting algorithm. However, it should be noted that the deck tracking results here do not account for any time delay in the deck measurement. In addition deck tracking results in added maneuvering during the landing procedure.   In addition, these simulation results were run with a constant RPM model and therefore the vertical axis performance may be somewhat optimistic. An engine model with dynamic rotor RPM was added later on.
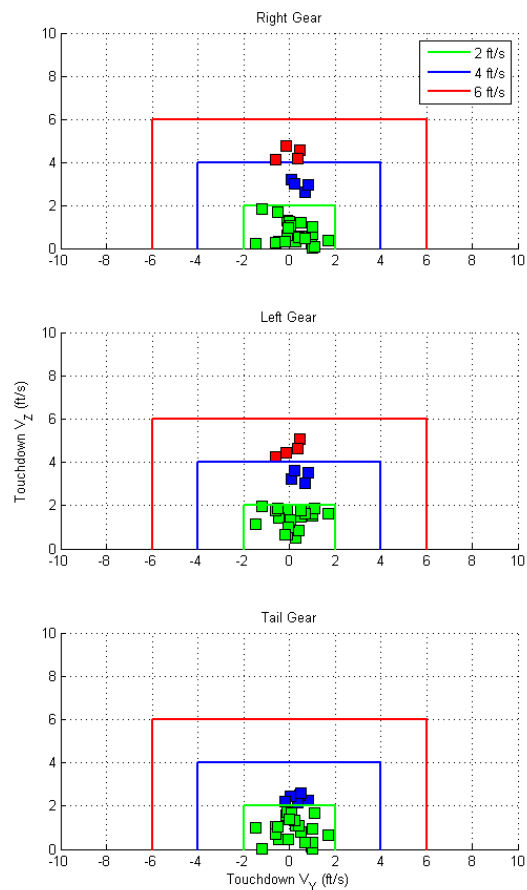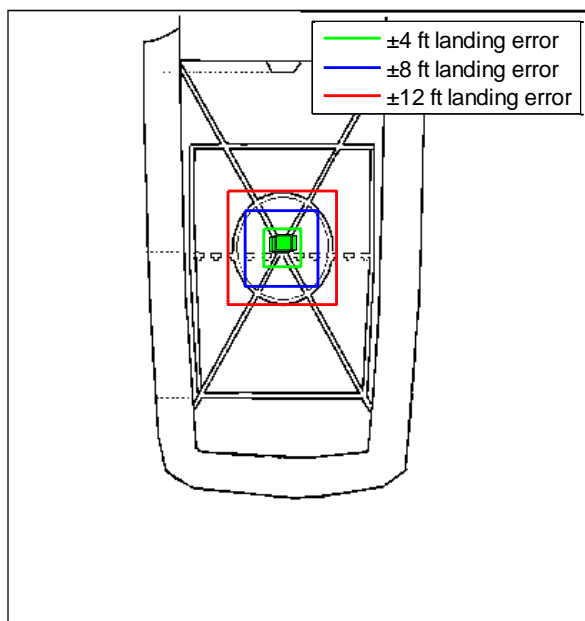
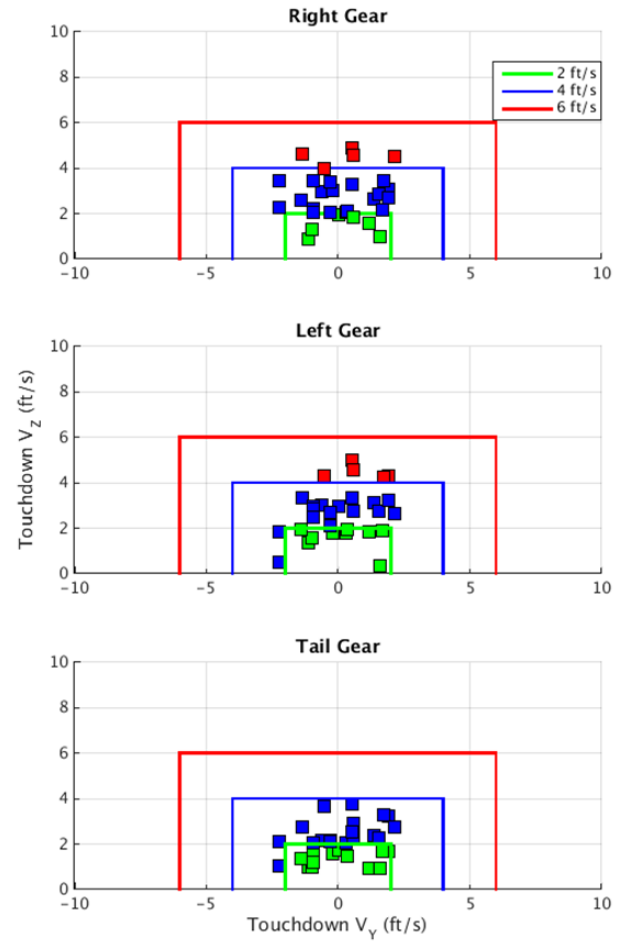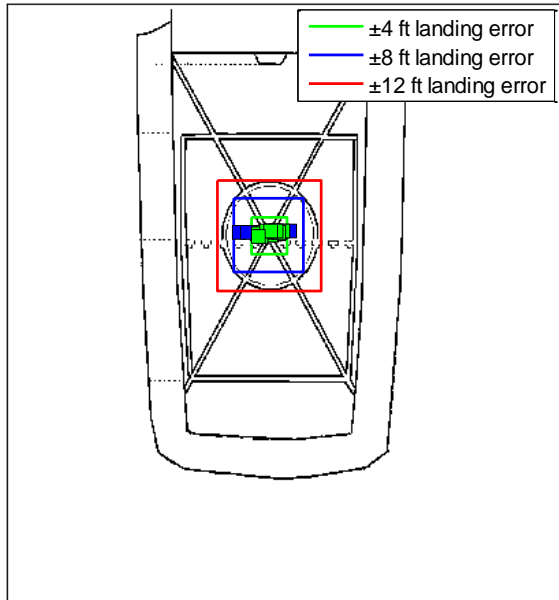Figure. 2.13.1 Landing Performance with Deck Tracking Method

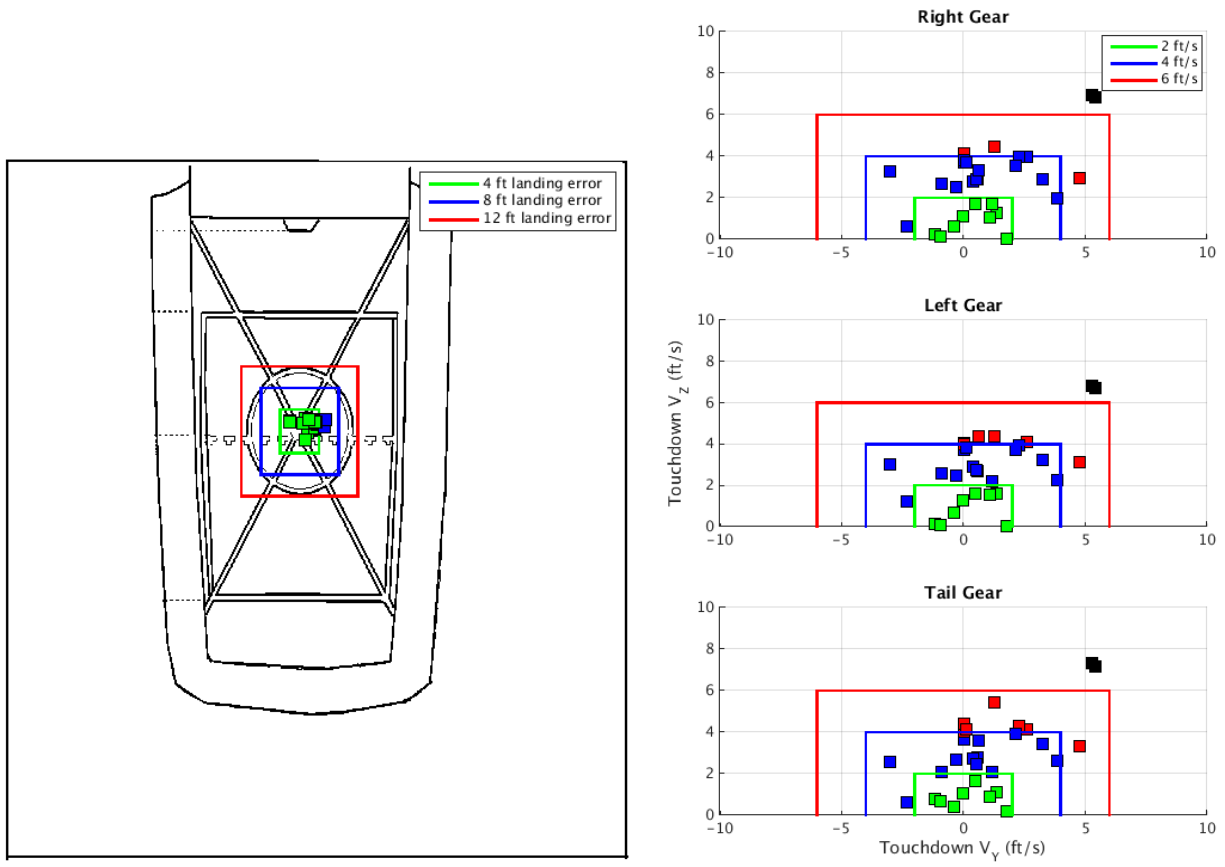Figure 2.13.2 Landing Performance with Deck Prediction Using Optimal Guidance Law

Figure 2.13.3 Landing Performance with Deck Prediction Using Path Optimization

| | Deck Tracking Method | Deck Prediction Method Using Optimal Guidance Law | Deck Prediction Method Using Path Optimization |
|---|---|---|---|
| Mean value of $e_{XPOS}$ (ft) | 0.5849 | 0.6742 | 1.403 |
| Standard deviation of $e_{XPOS}$ (ft) | 0.8217 | 0.1963 | 0.8096 |
| Mean value of $e_{YPOS}$ (ft) | 0.4359 | -0.3333 | 2.6343 |
| Standard deviation of $e_{YPOS}$ (ft) | 0.99 | 2.6168 | 1.6892 |
| Mean value of $e_{Vz}$ (ft/sec) | -1.5 | -2.6586 | -2.7 |
| Standard deviation of $e_{Vz}$ (ft/sec) | 1.2633 | 1.0569 | 1.8427 |
| Mean value of $e_{Vy}$ (ft/sec) | 0.216 | 1.2681 | 0.99 |
| Standard deviation of $e_{Vy}$ (ft/sec) | 0.7076 | 0.128 | 2.0385 |
| Present of cases with landing position error within ±4 ft | 100% | 73.33% | 86.67% |
| Present of cases with landing position error within ±8 ft | 100% | 100% | 100% |
| Present of cases with landing position error within ±12 ft | 100% | 100% | 100% |
| Present of cases with velocity at touchdown within in ±2 ft/sec | 63.33% | 30% | 26.67% |
| Present of cases with velocity at touchdown within in ±4 ft/sec | 86.67% | 83.33% | 63.33% |
| Present of cases with velocity at touchdown within in ±6 ft/sec | 100% | 100% | 93.33% |
| Present of cases with velocity at touchdown within in ±8 ft/sec | 100% | 100% | 100% |

Table 2.13.1 Statistic Metrics of Landing Quality

Additional cases have been analyzed for the medium class helicopter. The deck tracking landing control law was analyzed for a heavy version of the medium class, with gross weight 20,000 lbs and inertial properties scaled accordingly. In these results, the control law was not re-designed for the higher gross weight. Nonetheless, performance was still quite good and nearly the same as with the nominal gross weight. A case was also analyzed using a 0.2 sec time delay on the ship state feedback. The performance was degraded only slightly with the exception of a consistent aft bias on the landing location. Finally the light class was also tested using the deck tracking algorithm with successful results. Results are shown in Figure 2.13.4. Deck tracking was also tested on the light class model with good results as shown in Figure 2.13.5.
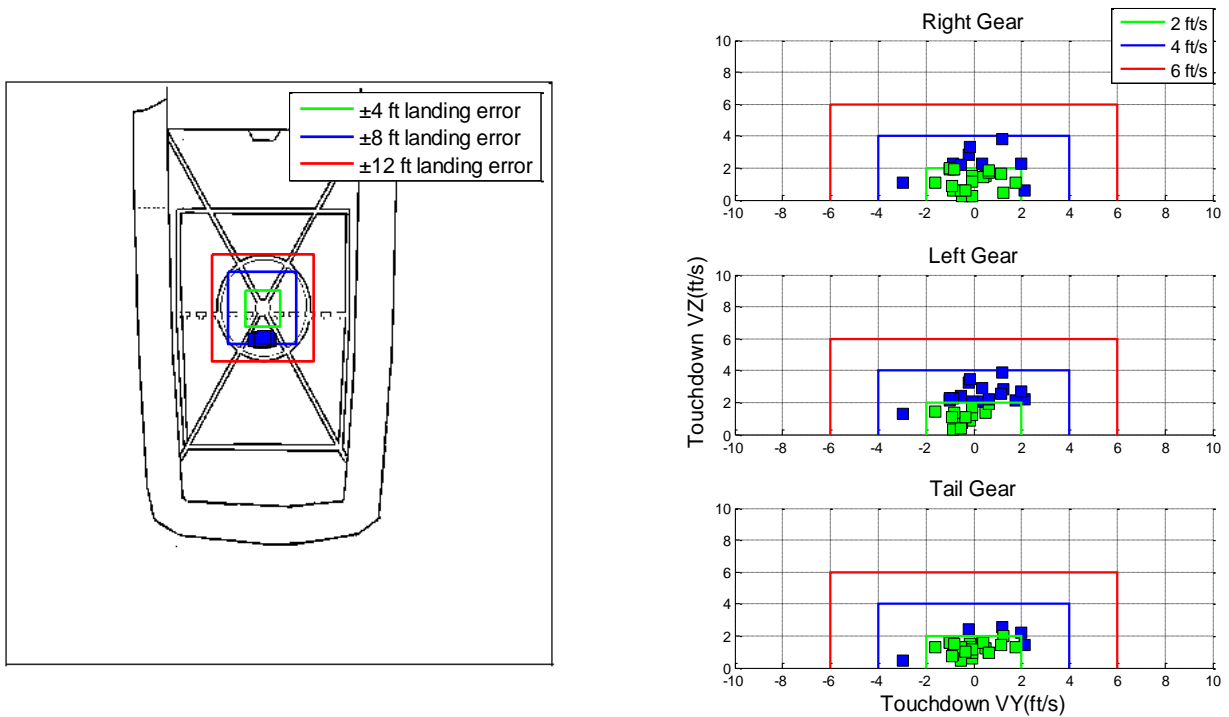


Figure 2.13.4 Landing Performance with Deck Tracking, 0.2 sec Time Delay
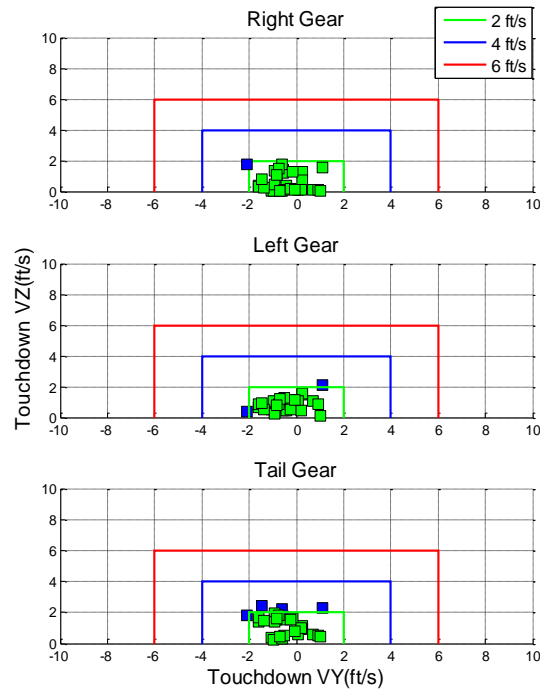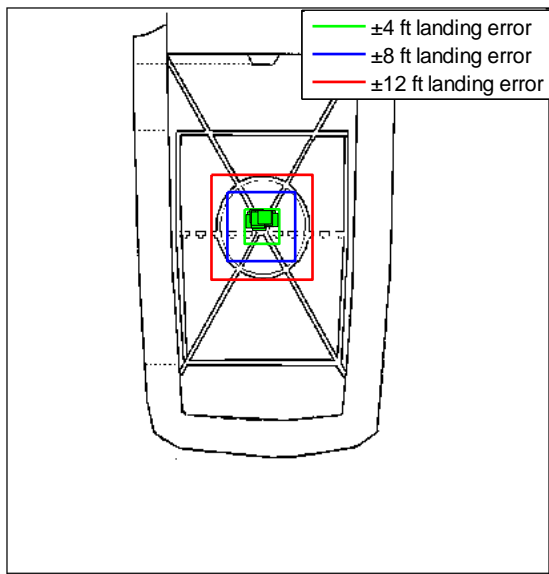
Figure 2.13.5 Landing Performance of the Light Class Model with Deck Tracking

## 2.14 Task 14 Documentation

During year 2, progress was reported in quarterly reports and at the annual review in November 2015. In addition, a conference paper was published:

"Autonomous Ship Approach and Landing using Dynamic Inversion Control with Deck Motion Prediction," Horn, J.F., Yang, J.F., He. C., and Lee D., 41st European Rotorcraft Forum, September 2015.

# 3    Summary and Conclusions

The base effort focused on development of advanced control laws, deck motion prediction algorithms, and path optimization techniques, and integration of these algorithms into the advanced simulation environment FLIGHTLAB.   A comprehensive tool set has been developed and can now be thoroughly evaluated in the year 3 option of the project.  It is notable that the design tools have proven to be highly modular and portable, with code be exchanged between multiple team members.  The tools have also been transition to outside Navy personnel; specifically Al Schwartz at the U.S. Naval Surface Warfare Center in Carderock has used the FLIGHTLAB software and Penn State control laws to perform sea-based aviation research.  A summary of work and conclusions drawn for each of the team members is summarized below:

## 3.1    Advanced Rotorcraft Technologies

The shipboard aircraft plant models for the rotorcraft configurations as proposed have been developed using the high fidelity FLIGHTLAB simulation program, including 1) a small UAV rotorcraft (FireScout class), 2) a utility helicopter (H-60 class), and 3) a large transport rotorcraft (H-53 class). Through this task, SCONE ship motion data were integrated with the FLIGHTLAB models, allowing the research to make use of standardized ship motion cases. In addition, the deck motion forecast method was established using the MCA algorithm and was tested for various conditions which were combinations of multiple sea states, ship speed, wave heading angle, significant wave height, and average wave modal period. The simulation results illustrated the capability of the MCA based ship motion forecasting algorithm by providing a forecast confidence measurement in terms of a statistical interpretation of the prediction error.

The KSOPT based optimization process was applied to find the optimal control parameters to improve overall approach and station-keeping maneuver for a light weight class helicopter model. Anticipated performance is obtained to enhance both the inner and outer loop control systems. The proposed optimization method has been packed with the light weight class helicopter model with SCONE2 data for utility testing. It was observed that the cost function should be carefully formulated for combined optimization of the inner-loop and outer-loop control systems.

## 3.2    Penn State

Penn State implemented the DI control laws with inner loop and outer loop path following control for all three classes of helicopters.  The design process is automated through a scripting process which has proven to be a reliable and fast method for porting control laws between different models.   Both straight-in and curved approach profiles were implemented and the control laws were able to successfully follow these paths.  Some of the key enablers for successful control included: use of feed-forward compensation with acceleration commands in the path following control, more rigorous vertical velocity modeling in the vertical axis component of the inner loop DI control law, and automated design scripts for generating airspeed scheduled linear models.

A study was performed to understand the trade off in feedback gains on stability margins and disturbance rejection. It was found that the DI control law produced the expected trend in the design

tradeoffs and a reasonable compromise in stability robustness and gust rejection can be defined. The main advantage of the DI approach is the de-coupling between axis such that gains can be tuned one axis at a time without significant changes in performance once all control loops are defined.

The landing control laws have proven to be the most challenging part of the automatic landing problem (more challenging than the approach), especially with larger ship motions.   Three different approaches were investigated: 1) Simple deck tracking; 2) Deck prediction with an optimal guidance law; 3) Deck prediction with path optimization.  Presently, the simple deck tracking method is the most reliable, with the following two deck prediction methods degrading in reliability (in the order listed). This is because of their sensitivity to the deck prediction accuracy.    However, the predictive algorithms provide the potential for additional flexibility in dealing with constraints, and the potential to reduce the maneuvering required for the landing task.

## 3.3   NAVAIR

The path optimization study showed that it is feasible to define and optimize a multi-parameter objective function for ship approaches in turbulent airwake, and that these objective functions can readily be tuned by careful selection of weights.  The path properties are naturally partitioned into temporal parameters (defining approach velocity and deceleration) and spatial parameters (defining orientation of the approach path).  For symmetric wind conditions (0° WOD), the performance was primarily sensitive to the temporal parameters, which govern the aggressiveness of the approach, while performance was largely insensitive to spatial parameters.  It was found that constraints needed to be considered to maintain stay within safe pitch attitude limits for very aggressive approach.  For the 30° WOD case, the turbulence effects became more important and were more sensitive to spatial parameters, including the azimuth of the approach, which is logical as the strength of airwake turbulence is likely to have more lateral spatial variation across the landing deck.  In all cases the objective functions tend to be very non-convex.

# 4   Accomplishments

1. Developed dynamic inversion control law for full trajectory control of ship approach and landing.  Automated design scripts to generate controllers for both medium and light class helicopters. Transitioned tools to NAVAIR and NSWC-Carderock.
2. Developed and demonstrated Minor Components Analysis (MCA) deck motion prediction algorithm.
3. Demonstrated successful autonomous landing using high fidelity simulations using deck tracking and deck motion prediction.  Used SCONE moderate deck motion case for small deck ship (representative of sea state 5).
4. Developed objective functions and optimized approach profiles for medium and light class approach to frigate.
5. Conference Publication: "Objective Function Development for Optimized Path Guidance for Rotorcraft Shipboard Recovery," Tritschler J.K., Horn, J.F., and He, C., AIAA Atmospheric Flight Mechanics Conference, June 2015.
6. Conference Publication: "Autonomous Ship Approach and Landing using Dynamic Inversion Control with Deck Motion Prediction," Horn, J.F., Yang, J.F., He. C., and Lee D., 41st European Rotorcraft Forum, September 2015.

# 5   Plans for Future Work

The final option year of the project will produce full integration of all of the control algorithms with each of the simulation models.  Then more comprehensive testing and evaluation of the final control laws will be performed.  This includes off-line simulations, and piloted simulation to test interface of the autonomous control modes with a human pilot (engage / dis-engage techniques).

Penn State will refine the landing control laws for the final testing and evaluation, and implement the medium and large class simulations in the Penn State Rotorcraft Flight Simulator.  Final versions of the control laws will be provided to ART for distribution of unified software to the team and interested U.S. Navy contacts.

The next focus of ART will be on the further integration of control laws as developed and case-tested with full flight simulation models in FLIGHTLAB. The integration will be made with the light, medium, and heavy class helicopter models that coupled with the effects of corresponding ship motion and ship airwake disturbance. ART, along with the team members, will also perform the integrated model simulation tests to evaluate the shipboard control effectiveness and aircraft performance. Any deficiency as revealed from the test and evaluation will be addressed to enhance the simulation.

NAVAIR will assist in final integration of optimal flight paths into the guidance law for each class of helicopter.  In addition, curved flight paths will be considered in the path optimization studies.

## 6  Financial Summary

Total funding Penn State University and their sub-contractor Advanced Rotorcraft Technologies were expended by the end date of the base effort: July 8, 2016.  Funding for NAVAIR is separate and therefore not reported here.

| Year | PSU Funds | ART Funds |
|------|-----------|-----------|
| 2014-2015 | $99K | $140K |
| 2015-2016 | $86K | $140K |

## 7  References

Stevens, B. L., Lewis, F. L., Aircraft Control and Simulation, John Wiley & Sons Inc., Hoboken, NJ, 2003, pp. 494-496.

Aeronautical Design Standard, Performance Specification, Handling Qualities Requirements for Military Rotorcraft, US Army Aviation and Missile Command, Redstone Arsenal, AL, ADS-33E-PRF, 2000. [4].

Anon., "Flight Control Systems - Design, Installation, and Test of Piloted Military Aircraft, General Specification for," SAE International, SAE-AS94900, 2007.

Oruc, I. B., Horn, J. F., "Coupled Flight Dynamics and CFD Simulations of the Helicopter / Ship Dynamic Interface," American Helicopter Society 71st Annual Forum Proceedings, Virginia Beach, VA, May 2015.

Sezer-Uzol, N., Sharma, A., and Long. L.N., "Computational Fluid Dynamics Simulations of Ship Airwake," Vol. 219, *Institute of Mechanical Engineering Part G Journal of Aerospace Engineering,* 2005.

Williams, S.L., Long, K.R., "ADS-33 and Shipboard Rotorcraft Operations: A USN Flight Test and Simulation Perspective," Proceedings of the American Helicopter Society 53rd Annual Forum, Virginia Beach, VA, April, 1997.

Horn, J. F., Bridges D. O., "A Model Following Controller Optimized for Gust Rejection during Shipboard Operations," American Helicopter Society 63rd Annual Forum Proceedings, Virginia Beach, VA, May 2007.

Cooper, J., Horn, J. F., Yomchinda, T., O'Neill E. P., "Handling Qualities Evaluation of an Adaptive Disturbance Compensation System for Ship-Based Rotorcraft," Journal of the American Helicopter Society, Volume 59, Number 2, April 2014, pp. 1-12.

Soneson, G. L., Horn, J. F., "Simulation Testing of Advanced Response Types for Ship-Based Rotorcraft," American Helicopter Society 70th Annual Forum Proceedings, Montreal, Quebec, Canada May 2014.

Horn, J. F., Guo, W., Ozdemir, G. T., "Use of Rotor State Feedback to Improved Closed Loop Stability and Handling Qualities," Journal of the American Helicopter Society, Volume 57, Number 2, April 2012, pp. 1-10.

Zheng, A., Horn, J.F.," Investigation of Bandwidth and Disturbance Rejection Properties of a Dynamic Inversion Control Law for Ship-based Rotorcraft", American Helicopter Society 71$^{st}$ Annual Forum, Virginia Beach, VA, May 5-7, 2015.

Heffley, R. K, "A model for Manual Decelerating Approaches to Hover", 15$^{th}$ Annual Conference on Manual Control Proceeding, Air Force Flight Dynamics Laboratory, Dayton, OH, November 1979.

Farin, G.," Curves and Surfaces for Computer Aided Geometric Design – a Practical Guide", Academic Press, 1988.

Bryson, E.E., Ho, Y.C.," Applied Optimal Control. Optimization, Estimation and Control", Hemisphere Publishing Corporation, New York, 1975.

Mansur, M. H., Lusardi, J. A., Tischler, M. B., and Berger, T., "Achieving the Best Compromise between Stability Margins and Disturbance Rejection Performance," American Helicopter Society 65th Annual Forum Proceedings, Grapevine, TX, May, 2009.

Blanken C. L., Tischler, M. B., Lusardi J. A., and Ivler, C. M., "Aeronautical Design Standard - 33 (ADS-33) ...Past, Present and Future," American Helicopter Society Rotorcraft Handling Qualities Specialists' Meeting, Huntsville, AL, Feb 2014.